



8-2009

Search for Electron Antineutrinos From The Sun With KamLAND Detector

Oleg Victorovic Perevozchikov
University of Tennessee - Knoxville

Recommended Citation

Perevozchikov, Oleg Victorovic, "Search for Electron Antineutrinos From The Sun With KamLAND Detector." PhD diss., University of Tennessee, 2009.
http://trace.tennessee.edu/utk_graddiss/106

This Dissertation is brought to you for free and open access by the Graduate School at Trace: Tennessee Research and Creative Exchange. It has been accepted for inclusion in Doctoral Dissertations by an authorized administrator of Trace: Tennessee Research and Creative Exchange. For more information, please contact trace@utk.edu.

To the Graduate Council:

I am submitting herewith a dissertation written by Oleg Victorovic Perevozchikov entitled "Search for Electron Antineutrinos From The Sun With KamLAND Detector." I have examined the final electronic copy of this dissertation for form and content and recommend that it be accepted in partial fulfillment of the requirements for the degree of Doctor of Philosophy, with a major in Physics.

Yuri Efremenko, Major Professor

We have read this dissertation and recommend its acceptance:

Robert N. Compton, Robert Grzywacz, Yuri Kamyshev

Accepted for the Council:

Carolyn R. Hodges

Vice Provost and Dean of the Graduate School

(Original signatures are on file with official student records.)

To the Graduate Council:

I am submitting herewith a dissertation written by Oleg Victorovic Perevozchikov entitled "Search for Electron Antineutrinos from the Sun with KamLAND detector". I have examined the final electronic copy of this dissertation for form and content and recommend that it be accepted in partial fulfillment of the requirements for the degree of Doctor of Philosophy, with a major in Physics.

We have read this dissertation
and recommend its acceptance:

Yuri Efremenko, Major Professor

Robert N. Compton

Robert Grzywacz

Yuri Kamyshkov

Accepted for the Council:

Carolyn R. Hodges
Vice Provost and Dean of the Graduate School

Search for electron anti-neutrinos
from the Sun with KamLAND
detector

A Dissertation

Presented for the

Doctor of Philosophy

Degree

The University of Tennessee, Knoxville

Oleg Perevozchikov

August 2009

Abstract

In this dissertation I present the results of the search for the electron antineutrinos from the Sun with Kamioka Liquid scintillator Anti-Neutrino Detector (KamLAND). There is no known direct production of the electron antineutrinos in the Sun. However, in the some theoretical models with the large neutrino magnetic moment antineutrinos from the Sun can be produced e.g. via Spin Flavor Precession mechanism (SFP). Search for solar antineutrinos potentially can provide new information about fundamental properties of neutrinos. The most sensitive one-kiloton antineutrino detector KamLAND gives the possibility to search for such antineutrinos.

The analysis described in this dissertation is based on 1425.9 days of data collection in KamLAND. The search for the electron antineutrinos have been made within 8.8-16.3MeV antineutrino energy range, that is above energies of reactor antineutrinos and where properties of the solar B^8 neutrinos are well studied. Based on the number of observed candidates and estimated background rates the upper limit on the electron antineutrino flux is set to be less than $1.2 \times 10^2 \text{ cm}^{-2}\text{s}^{-1}$ at 95% confidence level. The upper limit on the probability of conversion electron neutrinos produced in the Sun to electron antineutrinos is found to be less than 9.8×10^{-5} at 95% confidence level. Using the conversion probability the upper limit on the product of the neutrino magnetic moment and the transverse component of the magnetic field in the core of the Sun is set to be 7.7×10^{-2} . The same limit can be used on the diffuse Supernovae neutrino flux. The estimated background rates can make significant impact on the design of the future neutrino scintillator detectors.

Contents

1	Introduction	1
1.1	History of neutrinos and their properties	2
1.1.1	The neutrino	2
1.1.2	Neutrino oscillations	3
1.1.3	Neutrino magnetic moment	5
1.1.4	Neutrino mass	7
1.2	Neutrino sources	8
1.2.1	Solar neutrinos	8
1.2.2	Atmospheric neutrinos	11
1.2.3	Reactor neutrinos	13
2	KamLAND Detector	16
2.1	Inner detector	16
2.2	Outer detector	20
2.3	Front-end electronics and trigger system	20
2.4	Antineutrino detection	21
3	Scintillator response and energy scale in KamLAND	24
3.1	Non-linearity of liquid scintillator	24
3.1.1	The Birks' law	25
3.1.2	Cherenkov light absorption and reemission	26
3.2	LS response to low energy electrons measured with Compton spectrometer	29
3.2.1	Spectrometer design	30
3.2.2	Light yield with and without Tyvek	33
3.2.3	Spectrometer alignment	35
3.2.4	Monte-Carlo simulation of the real energy	36
3.2.5	Events selection in measurements of non-linearity	37

3.2.6 LS response to low-energy electrons (final result)	40
3.3 Monte-Carlo study of non-linearity	40
3.3.1 Cherenkov photons detection	41
3.3.2 Calculation of deposited energy with different Birks' coefficients	44
3.3.3 Monte-Carlo study results	45
4 Data Analysis	51
4.1 Verification of the energy scale	51
4.2 Candidates selection	55
5 Background Calculations	62
5.1 Accidental background	62
5.2 ^9Li background	64
5.3 Reactor neutrinos background	68
5.4 Atmospheric neutrinos background	69
5.4.1 Atmospheric charged current background	72
5.4.2 Atmospheric neutral current background	75
5.5 Background summary	79
6 Interpretation of results	82
6.1 Total number of candidates and background rate	82
6.2 Electron antineutrino flux limit	82
6.3 Limits on the neutrino conversion probability and product of the neutrino magnetic moment and magnetic field	83
6.4 Diffuse Supernovae neutrino flux	84
6.5 Future large scintillator neutrino detectors	85
7 Conclusions	87
Bibliography	89
Vita	92

List of Tables

Table 1: Nuclear fusion reactions producing solar neutrinos	9
Table 2: Expected and reconstructed (visible) energy for gamma calibration sources. ...	24
Table 3: Summary of the measurements with and without Tyvek	33
Table 4: Accidental background summary (scaled to neutrino detection time interval). .	64
Table 5: Background summary for the 5.5 meters fiducial volume	80
Table 6: Background summary for 6.0 meters fiducial volume	80
Table 7: Triple coincidence events in KamLAND data and Monte-Carlo study of the background.....	81

List of Figures

Figure 1: Energy spectrum of neutrinos produced in the Sun. Solid line is PP-chain neutrinos and dashed line corresponds to CNO-cycle neutrinos [9]......	9
Figure 2: Solar neutrino flux from different sources as a function of solar radius [9].	10
Figure 3: ^8B solar neutrino fluxes from different modes of neutrino detection [11].	11
Figure 4: Zenith angle distributions of e-like, μ -like and UP μ are shown for data (filled circles with statistical error bars), Monte-Carlo distributions without oscillations (boxes) and best fit with oscillations distributions (red dashed). These distributions show the azimuth angle anomaly observed by SuperKamikande.	12
Figure 5: SuperKamiokande neutrino oscillation parameters $\sin^2 2\theta_{23}$ and Δm_{23}^2	13
Figure 6: Anti-neutrino energy spectrums from the following isotopes: U235:[16], Pu239,241:[17], U238:[18].	14
Figure 7: The ratio of the background subtracted electron antineutrino candidates including the subtraction of geo-neutrinos to no-oscillation expectations as a function of L_0/E , where $L_0=180$ km is effective baseline taken as a flux-weighted average [8]. Blue line shows the expectation based on KamLAND oscillation parameters and experimental points are black.	15
Figure 8: Allowed region for neutrino oscillation parameters from KamLAND and solar neutrino experiments.....	15
Figure 9: Scheme of the KamLAND experimental site.....	17
Figure 10: Nuclear power plants and KamLAND location	18
Figure 11: KamLAND detector design.....	19
Figure 12: Energy dependence of cross section of electron antineutrinos interactions on free proton.	22

Figure 13: Antineutrinos interaction in KamLAND. Positron energy loss along with its annihilation gives prompt signal and neutron capture on proton gives delayed signal. ...	23
Figure 14: Observed non-linearity of energy scale, measured with calibration γ -sources represented by energy dependence of ratio between expected and real energy. The red line shows what is expected in case of the 100% linear response of the detector.	25
Figure 15: Wavelength dependence of KamLAND liquid scintillator refractive index...	27
Figure 16: PMT photocathode quantum efficiency.	28
Figure 17: Probability of reemission of light dependence on absorbed light wavelength.	29
Figure 18: Scheme of the Compton Spectrometer.....	31
Figure 19: Compton Spectrometer Design	31
Figure 20: Quartz vessel for KamLAND liquid scintillator.	32
Figure 21: Amplitude of Compton peak from 0.511 MeV gamma line at scattering angle 30° versus volume of exchanged nitrogen.....	32
Figure 22: Amplitude of signal in the LS with and without Tyvek for 0.511MeV and 1.275MeV gamma lines at 60 degrees NaI position.	34
Figure 23: Deposited energy in the LS as a function of angular deviation from real angular position of the NaI detector. Blue line is deposited energy by recoil electron for 30 degrees NaI position and incident 1.275MeV gamma. Red line is deposited energy of the recoil electron for 120 degree NaI position and incident 0.511 MeV gamma.....	35
Figure 24: Collimator alignment procedure with respect of 0 degrees position of NaI detector and measurements of the event rate in NaI for different displacement of the NaI. Red line – before alignment and blue line – after alignment procedure.....	36
Figure 25: Real energy deposited in LS by recoil electron for the different angular position of the NaI detector. Right plot is for the 0.511MeV incident gamma and left plot is for 1.275MeV gamma.	37
Figure 26: Correlation between energy deposition in the NaI detector and LS at the 20 degrees angular position of the NaI. The left plot corresponds to the real measurements and the right one to the Monte Carlo simulation.	38

Figure 27: Distribution of the recoil electron energy in the LS for both incident gammas at 70 degrees angular position of the NaI detector. The blue histogram shows the MC result and the white shows real data.	38
Figure 28: Selection of the energy deposited in the LS by recoil electrons coming from incident gammas with the different initial energy. White histogram – before energy cut in the NaI and red – after energy cut in the NaI.....	39
Figure 29: Liquid scintillator non-linear response to low-energy electrons measured as a ratio between visible and real energy of the recoil electron as a function of real energy.	40
Figure 30: Initial spectrums of the Cherenkov light produced by electrons with different initial kinetic energies. Spectrums are normalized to one initial electron.	43
Figure 31: Cherenkov light collection with and without reemission as a function of kinetic energy of electron. Red line represents the light collection without reemission mechanism and the blue line light collection taking into account reemission process.....	44
Figure 32: Possible parameter region of the Birks coefficients and scintillation light output for the C.L. 99%, 95% and 90%. Black point corresponds to the minimum χ^2 ...	46
Figure 33: Scintillation light output calibration setup	46
Figure 34: Distribution of the signals from PMT at 1600V (left) and 1250V (right).....	48
Figure 35: PMT signal distribution from the single photoelectron as a function of ADC channels.....	48
Figure 36: Cherenkov light contribution as a function or recoil electron energy	49
Figure 37: Non-linearity of the LS response to electrons measured by Compton Spectrometer (red) and from Monte-Carlo study (blue) as a function of real electron energy.....	49
Figure 38: The LS response to electrons (Blue – Compton Spectrometer measurements, Red – Monte-Carlo study) same as Figure 37. The LS response to gammas (Green – KamLAND measurements with gamma calibration sources, Purple – Monte-Carlo study)	50

Figure 39: Proton quenching parameterization based on measurements made by OKTAVIAN Facility (blue line) and Monte-Carlo calculations (red line)	50
Figure 40: Energy distribution of the final event candidates from the first solar antineutrino KamLAND paper [28]. No candidates were found in the region of interest. The tail from reactor electron antineutrinos is visible below 8 MeV.	52
Figure 41: R^3 distribution of the ^{12}B events with different energy cuts inside the KamLAND detector as a function of radius of the balloon with scintillator. X-axis is a cubed ratio between actual radius of the event and radius of the balloon.	54
Figure 42: Reconstruction inefficiency of the ^{12}B events. Ratio between the events reconstructed inside the buffer oil to the total number of reconstructed events as a function of energy.	55
Figure 43: Energy spectrum of ^{12}B decay. Blue points are KamLAND data, red line is theoretical spectrum of ^{12}B decay and green points obtained from Monte-Carlo.	56
Figure 44: Spatial (left) and timing (right) correlation between events high statistics (reactor antineutrino analysis).....	57
Figure 45: 5.5 meters volume. Prompt (left) and delayed (right) events energy spectra. Green candidates – one prompt and one delayed events, blue candidates – multiple neutron captures, red candidates – muon decay.....	60
Figure 46: 6.0 meters volume. Prompt (left) and delayed (right) events energy spectra. Green candidates – one prompt and one delayed events, blue candidates – multiple neutron captures, red candidates – muon decay.....	60
Figure 47: 5.5 meters volume. Space (left) and time (right) correlation between prompt and delayed events. Green candidates – one prompt and one delayed events, blue candidates – multiple neutron captures, red candidates – muon decay.	61
Figure 48: 6.0 meters volume. Space (left) and time (right) correlation between prompt and delayed events. Green candidates – one prompt and one delayed events, blue candidates – multiple neutron captures, red candidates – muon decay.	61
Figure 49: Accidental time intervals distribution between prompt and delayed events. ...	63

Figure 50: Energy distribution of the accidental events for the 5.5 m volume on the left and 6.0 m volume on the right. Number of events on both histograms has to be scaled by factor of 10^{-4} in order to obtain real number of accidentals.....	63
Figure 51: Energy distribution of the ${}^9\text{Li}$ events selected from the data (blue). Theoretical spectrum of the ${}^9\text{Li}$ β -decay events (red).	65
Figure 52: Visible energy spectrum of neutron capture events. First peak around 2.2MeV corresponds to neutron capture on proton and second peak around 5MeV corresponds to capture on ${}^{12}\text{C}$	67
Figure 53: Distance between spallation neutron capture and muon track. 94.1% of events are within 3 meters cylindrical volume around muon track.	67
Figure 54: Expected prompt energy spectrum from reactor antineutrinos with oscillations.	69
Figure 55: Source of the background from atmospheric neutrinos.....	70
Figure 56: Atmospheric neutrino fluxes at KamLAND site: electron (anti)neutrinos fluxes on the left and muon (anti)neutrinos on the right. Solid color lines correspond to neutrinos and dashed lines correspond to antineutrinos.	71
Figure 57: Cross-section per nucleon of muon antineutrino interactions on ${}^{12}\text{C}$ (left). Cross-section of muon antineutrino interactions on free proton (right).	73
Figure 58: R^3 distributions for 6m volume of the muon-prompt event (left) and positron-prompt event (right).	74
Figure 59: Distance between prompt and delayed events for muon-prompt event (left) and positron-prompt event (right).....	74
Figure 60: Prompt energy spectra of the background events coming from interactions of atmospheric muon antineutrinos on proton.....	75
Figure 61: Cross-section of neutral current interaction of 1.25 GeV neutrinos on free proton and neutron as a function of squared transferred momentum.	76
Figure 62: R^3 distribution of the neutral current (outer shell) background events in 6m. fiducial volume.	77

Figure 63: Distance between prompt and delayed events for neutral current interaction (outer shell) in 6m fiducial volume.....	78
Figure 64: Prompt energy spectra of background from neutral current interactions (outer shell) in 6m fiducial volume.	78
Figure 65: Atmospheric neutrino background spectra. The red line shows the background from charged current interactions. Green and blue lines correspond to background from neutral current interactions with neutron emission from inner and outer shells of carbon atom, respectively. Black line corresponds to the total background induced by atmospheric neutrino interactions.	79
Figure 66: Diffuse Supernovae neutrino flux and current limits obtained by SuperK, SNO and KamLAND. The blue solid lines and the red dash lines correspond to electron antineutrinos and electron neutrinos respectively. The black line represents the theoretically predicted diffuse supernovae flux. The green solid line represent limit obtained during this study. The plot had been taken from [38] and current study limit had been added.	85
Figure 67: Event rates expected by LENA experiment from reactor, atmospheric and diffuse supernovae electron antineutrinos. DSNF is based on various models (LL, KRJ and TBP). Plot is taken from [40]. Red dashed line added to this plot shows neutral current background calculated during this study and scaled corresponding time exposure and target volume of proposed LENA experiment.	86

Chapter 1

Introduction

The neutrino magnetic moment has never been measured before. According to the Standard Model of Electro-Weak Interactions (SM) the neutrino has a non-zero magnetic moment with an unreachable magnitude with present experimental technique $\mu_\nu = 3.2 \times 10^{-19} (m_\nu/\text{eV}) \mu_B$. However, there are SUSY models [1] setting the upper limit up to $10^{-15} \mu_B$ on the neutrino magnetic moment that is larger than in SM. Models mostly based on stellar evolution [2], [3], set the model dependent upper limit on the neutrino magnetic moment μ_ν up to $10^{-12} \mu_B$. The most stringent direct experimental limit on the neutrino magnetic moment is about nine orders of magnitude higher than those predicted by the Standard Model of Electro Weak interactions [4]. Observation of such large value of the neutrino magnetic moment will be a clear indication of the physics outside the Standard Model of Electro-Weak Interactions.

Neutrinos with non-negligible magnetic moment can interact with strong magnetic fields within Solar interior and resulting in Spin Flavor Precession (SFP) process. Such a process with following neutrino oscillations could be an effective mechanism of conversion of neutrinos generated in the solar core into antineutrinos. Probability of SFP is proportional to the product of the neutrino magnetic moment and solar magnetic field.

One-kiloton KamLAND detector specially optimized for antineutrino detection has the best sensitivity for solar antineutrino detection in the world. Due to the large fiducial volume and long time of operation it gives the possibility to detect solar antineutrinos or to set a new limit on the product of the neutrino magnetic moment and the solar magnetic field.

1.1 History of Neutrinos and Their Properties

1.1.1 The Neutrino

The first indication on the existence of a new electrically neutral particle was found in the beginning of the twentieth century. Studying β -decay reaction the observed spectrum of an emitted electron appeared to be continuous while the discrete spectrum had been expected. This observation was an obvious contradiction of the energy conservation law. The existence of an extra particle emitted along with the electron during the β -decay reaction could be the possible solution to this problem. Later in 1930 W. Pauli proposed the existence of electrically neutral particle that can be one of the products of the β -decay reactions responsible for carrying away extra energy. In 1933 E. Fermi called this particle a “neutrino” which in Italian means “little neutral one”. According to the Standard Model of Electro Weak interactions there are three charged leptons: electron, muon, tau (e, μ, τ). Each lepton has a corresponding neutrino (ν_e, ν_μ, ν_τ), that calls neutrino flavor. Neutrinos have zero charge and spin $1/2$. During the last couple of decades there were many experiments trying to study neutrino properties. Neutrinos are very different from other particles. They have very small, but non-zero mass. The most unusual property is that neutrinos can experience the transformation of one type of neutrino into another. That process is called “neutrino oscillations”. The fact that neutrinos could change their flavor, did confirm that neutrinos have non-zero mass. Recent results from SuperKamiokande, SNO and KamLAND collaborations show the existence of neutrino oscillations.

Due to the zero electric charge the neutrino cannot participate in electromagnetic interactions. Neutrinos can be only involved in weak interactions mediated by massive Z^0 or W^\pm . The range of the weak interactions is about 10^{-18} meters. Due to this fact, it is very hard to detect neutrinos since the cross-section of neutrino interactions with matter is $\sim 10^{-48} \text{ m}^2$.

1.1.2 Neutrino Oscillations

In 1955 it was observed that neutral kaons oscillate to its antiparticles. Two years later Bruno Pontecorvo proposed a similar idea for neutrino oscillations. Lets consider the most general case of the three-flavor model of neutrino oscillations in vacuum. The flavor eigenstates ν_e, ν_μ, ν_τ can be expressed in terms of mass eigenstates ν_1, ν_2 and ν_3 :

$$|\nu_\alpha\rangle = \sum_{i=1}^3 U_{\alpha i} |\nu_i\rangle, \quad (\alpha = e, \mu, \tau) \quad (1)$$

The unitary 3×3 matrix U is the Maki-Nakagawa-Sakata matrix constructed using three mixing angles $\theta_{12}, \theta_{23}, \theta_{13}$ and CP phase δ .

$$U = \begin{bmatrix} U_{e1} & U_{e2} & U_{e3} \\ U_{\mu1} & U_{\mu2} & U_{\mu3} \\ U_{\tau1} & U_{\tau2} & U_{\tau3} \end{bmatrix} = \begin{bmatrix} 1 & 0 & 0 \\ 0 & c_{23} & s_{23} \\ 0 & -s_{23} & c_{23} \end{bmatrix} \begin{bmatrix} c_{13} & 0 & s_{13}e^{-i\delta} \\ 0 & 1 & 0 \\ -s_{13}e^{i\delta} & 0 & c_{13} \end{bmatrix} \begin{bmatrix} c_{12} & s_{12} & 0 \\ -s_{12} & c_{12} & 0 \\ 0 & 0 & 1 \end{bmatrix} = \quad (2)$$

$$= \begin{bmatrix} c_{12}c_{13} & s_{12}c_{13} & s_{13}e^{-i\delta} \\ -s_{12}c_{23} - c_{12}s_{23}s_{13} & c_{12}c_{23} - s_{12}s_{23}s_{13}e^{i\delta} & s_{23}c_{13} \\ s_{12}s_{23} - c_{12}c_{23}s_{13} & -c_{12}s_{23} - s_{12}c_{23}s_{13}e^{i\delta} & c_{23}c_{13} \end{bmatrix}$$

where, $s_{ij} = \sin\theta_{ij}$ and $c_{ij} = \cos\theta_{ij}$ and $(i,j=1, 2, 3)$.

The time dependant Shrödinger equation expresses the time evolution of mass eigenstates (3).

$$i \frac{d}{dt} |\nu_j\rangle = E_j |\nu_j\rangle \quad (3)$$

where E_j is the energy of ν_j and the wave function is expressed by (4),

$$|\nu_j(t)\rangle = e^{-iE_j t} |\nu_j(0)\rangle \quad (4)$$

From (1), (3) and (4) one can obtain the relationship for the flavor eigenstates,

$$i \frac{d}{dt} |\nu_\alpha\rangle = \sum_{j=1}^3 U_{\alpha j} E_j U_{j\alpha}^\dagger |\nu_\alpha\rangle \quad (5)$$

$$|\nu_\alpha(t)\rangle = \sum_{j=1}^3 U_{\alpha j} e^{-iE_j t} U_{j\alpha}^\dagger |\nu_\alpha(0)\rangle \quad (6)$$

If at $t=0$ ν_α have been born then the probability to detect ν_β at time t is represented by (7)

$$\begin{aligned} P(\nu_\alpha \rightarrow \nu_\beta) &= \left| \langle \nu_\beta(t) | \nu_\alpha(0) \rangle \right|^2 = \sum_{j=1}^3 \left| \langle \nu_\beta(t) | U_{\alpha j} e^{-iE_j t} U_{j\alpha}^\dagger | \nu_\alpha(0) \rangle \right|^2 = \\ &= \delta_{\alpha\beta} - 4 \sum_{i>j} \text{Re}(U_{\alpha i}^* U_{\beta i} U_{\alpha j} U_{\beta j}^*) \cdot \sin^2 \Psi_{ij} \pm 2 \sum_{i>j} \text{Im}(U_{\alpha i}^* U_{\beta i} U_{\alpha j} U_{\beta j}^*) \cdot \sin^2 \Psi_{ij} \end{aligned} \quad (7)$$

where

$$\Psi_{ij} \equiv \frac{\Delta m_{ij}^2 L}{4E_\nu} = \frac{1.27 \Delta m_{ij}^2 [eV^2] L[m]}{E_\nu [MeV]} \quad (8)$$

$\Delta m_{ij}^2 = m_i^2 - m_j^2$, L is the distance from the neutrino production point and E_ν is the neutrino energy.

Now let us consider a simplified case of two-flavor neutrino oscillations in vacuum. Similar to the general case of three flavor oscillations, the flavor eigenstates ν_μ and ν_e can be expressed in terms of mass eigenstates ν_1 and ν_2 :

$$\begin{pmatrix} \nu_e \\ \nu_\mu \end{pmatrix} = \begin{pmatrix} \cos \theta & \sin \theta \\ -\sin \theta & \cos \theta \end{pmatrix} \begin{pmatrix} \nu_1 \\ \nu_2 \end{pmatrix} \quad (9)$$

where θ is mixing angle. Mass eigenstates can, in turn, be expressed in terms of flavor eigenstates:

$$\begin{pmatrix} \nu_1 \\ \nu_2 \end{pmatrix} = \begin{pmatrix} \cos \theta & -\sin \theta \\ \sin \theta & \cos \theta \end{pmatrix} \begin{pmatrix} \nu_e \\ \nu_\mu \end{pmatrix} \quad (10)$$

Using time dependent Shrödinger equation the mass eigenstate can be written as,

$$|\nu_i(t)\rangle = e^{-iE_i t} |\nu_i(0)\rangle \quad (11)$$

Then using (9) the time evolution of ν_e can be expressed as a combination of mass eigenstates and after that using (10) it can be written in the form of a combination of neutrino flavors,

$$\begin{aligned} |\nu_e(t)\rangle &= (\cos^2 \theta e^{-iE_1 t} + \sin^2 \theta e^{-iE_2 t}) |\nu_e\rangle \\ &+ \sin \theta \cos \theta (-e^{-iE_1 t} + e^{-iE_2 t}) |\nu_\mu\rangle \end{aligned} \quad (12)$$

Therefore the oscillation probability is

$$P(\nu_e \rightarrow \nu_\mu, t) = \frac{1}{2} \sin^2(2\theta) [1 - \cos(E_1 - E_2)t] \quad (13)$$

Using the fact that $E_i \approx p + m^2/2p$ and $L = ct$ the oscillation probability can be written in a different form

$$P(\nu_e \rightarrow \nu_\mu) = \sin^2(2\theta) \sin^2 \left[\frac{1.27 \Delta m^2 [eV^2] L [m]}{E [MeV]} \right] \quad (14)$$

1.1.3 Neutrino magnetic moment

Under the Standard Model of Electro-Weak Interactions the neutrino magnetic moment is predicted to be unobservably small: $\mu_\nu = 3.2 \times 10^{-19} (m_\nu/eV) \mu_B$ and it is proportional to the, as yet, unknown neutrino mass - m_ν . Recently the MUNU Collaboration along with TEXONO Collaboration set the new direct limits on the neutrino magnetic moment: $\mu_\nu < 9 \times 10^{-11} \mu_B$ [5]. Large time projection chamber located near the nuclear power plant was used for this experiment. The cosmological limit on the neutrino magnetic moment is $\mu_\nu < 10^{-12} \mu_B$ [2], [3]. This indirect limit is based on estimations of stellar evolution and red giants cooling time and might be not as reliable as direct measurements. Taking into consideration that the neutrino can have a magnetic moment up to $9 \times 10^{-11} \mu_B$ there is a possibility of detecting electron antineutrinos from the Sun.

There is no direct production of electron anti-neutrinos in the Sun within energy range up to 18 MeV. During the CNO- cycle and pp-chain reactions only electron neutrinos can be produced. If the neutrinos have a magnetic moment significantly larger than that predicted by the Standard Model there is a possibility of observation of the neutrino conversion mechanism. Assuming neutrinos to be Majorana particles the following process of neutrino conversion can be shown as:

$$\nu_{eL} \xrightarrow{SFP} \nu_{\mu R} \xrightarrow{osc.} \nu_{eR} \quad (15)$$

If the neutrino magnetic moment is several orders of magnitude larger than it is predicted by the Standard Model the neutrino's spin will precess under strong transverse magnetic field [6]. Spin flavor precession (SFP) converts a solar electron neutrino into a muon anti-neutrino since the neutrino spin has been changed from -1/2 to 1/2 due to the interaction with the strong magnetic field ($B_T \sim 10^7 G$). This process could occur at the central region of the Sun's core $R \sim 0.05 R_{\text{Sun}}$. Then muon anti-neutrinos oscillate into electron anti-neutrinos in vacuum on their way to the Earth.

Since the conversion of electron neutrinos to electron antineutrinos occurs in two consequent steps the probability of such a process consist of two independent parts. First, is the probability of conversion of an electron neutrino to a muon antineutrino which depends on the magnetic field and electron neutrino production region and second is the probability of a muon antineutrino oscillation into an electron antineutrino in vacuum on its way from the Sun to the Earth. The SFP conversion probability is represented by (16) [7],

$$P(\nu_{eL} \rightarrow \bar{\nu}_{\mu R}) = 3.6 \times 10^{-10} \left[\frac{\mu}{10^{-12} \mu_B} \frac{B_T(0.05 R_{\text{sun}})}{10 kG} \right]^2 \quad (16)$$

where μ is the neutrino magnetic moment and B_T is the transverse magnetic field in the region of neutrino production. Now we can combine the probability of oscillation of muon antineutrino to electron antineutrino on its way from the Sun to the Earth using (14) with SFP conversion probability (16). Taking into account multiple oscillations of neutrinos on the way from the Sun to the Earth and using the latest value of θ_{12} obtained by KamLAND [8], SNO and solar neutrino experiments we replace the oscillation equation (14) with the average value of the probability. Finally, the probability of electron neutrino conversion to electron antineutrino becomes:

$$P(\nu_{eL} \rightarrow \bar{\nu}_{eR}) = 1.657 \times 10^{-10} \left[\frac{\mu}{10^{-12} \mu_B} \frac{B_T(0.05 R_{sun})}{10 kG} \right]^2 \quad (17)$$

1.1.4 Neutrino mass

It is assumed in The Standard Model of Electroweak Interactions that neutrinos have zero mass. Observation of neutrino oscillations governed by Δm^2 established that neutrinos are massive particles, although determination of absolute value of neutrino mass was not possible in oscillation experiments. Until recently the results of direct laboratory experiments have not given any indications that neutrinos have non-zero mass although upper limits on neutrino mass had been established a relatively long time ago. However, there is a cosmological limit on the sum of the mass of three neutrino flavors. This limit comes from cosmic microwave background radiation (CMBR) explained by the Big Bang Theory. CMBR was discovered in 1964 by Arno Penzias and Robert Wilson. The latest study of CMBR based on results obtained by the Wilkinson Microwave Anisotropy Probe (WMAP) significantly improved the cosmological limit on neutrino mass. According to it the upper limit on sum of all three neutrino flavors is $\Sigma m_\nu < 0.63 \text{ eV}$ with the 95% C.L. [21]. Recently the existence of neutrino oscillations had been confirmed. This fact proves that neutrino mass cannot be zero. Neutrino oscillation experiments are sensitive only for mixing angle and the difference of squared mass of two neutrinos flavor, but not for the neutrino mass itself. Using the Δm^2 the lower limit on the neutrino mass can be set. From the latest KamLAND publication [8] $\Delta m_{21}^2 = 7.59 \times 10^{-5} \text{ eV}^2$ which gives the lower limit on mass of at least one neutrino flavor $m_\nu \geq 0.0087 \text{ eV}$.

In 90's the Mainz neutrino mass experiment was trying to improve the neutrino mass limits by studying electron spectra endpoint in tritium β -decay (18). Using data collected in 1997 through 1999 the new limit had been set $m_\nu < 2.8 \text{ eV}$ [25]. At present time KATRIN neutrino mass experiment located in Karlsruhe, Germany is trying to

improve the current limit on neutrino mass. The experiment is based on the study of electron spectra tritium β -decay (18) as well. Its planned sensitivity is up to 0.2eV neutrino mass. The data is coming soon.

1.2 Neutrino Sources

1.2.1 Solar Neutrinos

Production of energy on the Sun is the result of thermo-nuclear fusion chain reactions. In 1939 G. Bethe considered the carbon-nitrogen-oxygen cycle, known as the CNO cycle, as one of the sources of helium production from hydrogen in stars. The interaction of ^{12}C with a proton gives the consequent chain of the reactions with helium as the product of this chain. The CNO chain is one of the solar neutrino sources. The other, and most significant, source is the proton-proton chain of reactions occurring on the Sun, which gives about 98% of solar energy. The nuclear fusion reactions producing solar neutrinos are summarized in Table 1. According to the energy coming out from the proton-proton chain of reactions it is possible to calculate the spectra of neutrinos produced on the Sun. The solar neutrino spectrums from the CNO-cycle and PP-chain are shown in Figure 1 [9]. The region of neutrino production in the Sun for each reaction is shown in Figure 2 [9]. The first experiment dedicated to solar neutrino observation started in the South Dakota mine in 1967 by R. Davis. The detector was filled with C_2Cl_4 and the detection of neutrinos occurred through the neutrino capture on ^{37}Cl (19).



The results were published in 1968 [10]. Although there was an evidence of neutrino signal, the deficit of neutrinos has been observed.

Table 1: Nuclear fusion reactions producing solar neutrinos

Reaction	Name	Flux, $\text{cm}^{-2}\text{sec}^{-1}$
PP-chain		
$\text{pp} \rightarrow \text{de}^+ \nu_e$	pp	5.94×10^{10}
$\text{pep} \rightarrow \text{d} \nu_e$	pep	1.40×10^8
${}^3\text{He p} \rightarrow \text{e}^+ \nu_e$	hep	7.88×10^3
${}^7\text{Be e}^- \rightarrow \text{e}^+ \nu_e$	${}^7\text{Be}$	4.86×10^9
${}^8\text{B} \rightarrow {}^8\text{Be e}^+ \nu_e$	${}^8\text{B}$	5.82×10^6
CNO-cycle		
${}^{13}\text{N} \rightarrow {}^{13}\text{C e}^+ \nu_e$	${}^{13}\text{N}$	5.71×10^8
${}^{15}\text{O} \rightarrow {}^{15}\text{N e}^+ \nu_e$	${}^{15}\text{O}$	5.03×10^8
${}^{17}\text{F} \rightarrow {}^{17}\text{O e}^+ \nu_e$	${}^{17}\text{F}$	5.91×10^6

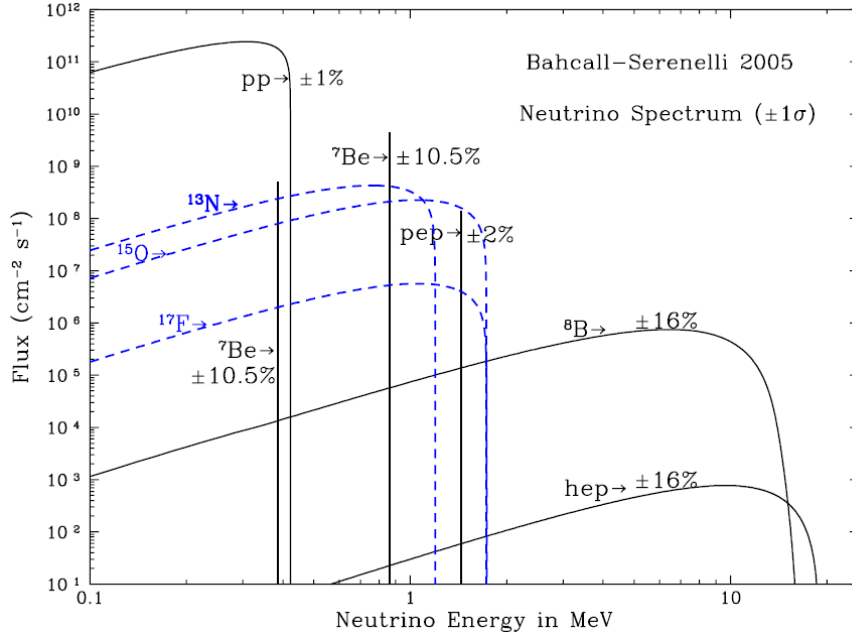


Figure 1: Energy spectrum of neutrinos produced in the Sun. Solid line is PP-chain neutrinos and dashed line corresponds to CNO-cycle neutrinos [9].

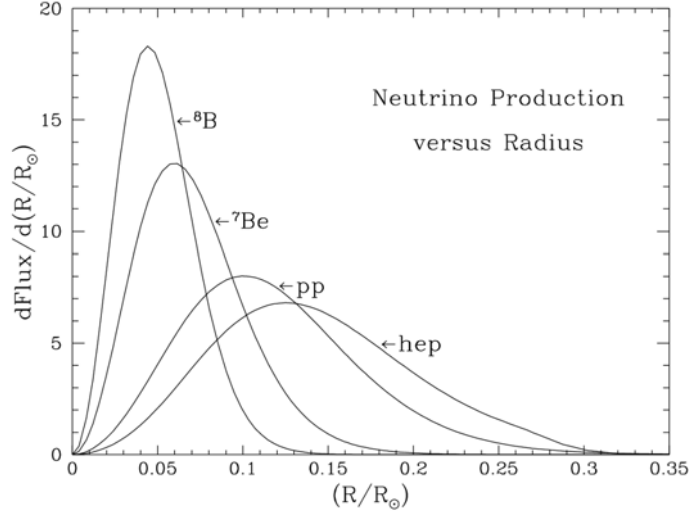


Figure 2: Solar neutrino flux from different sources as a function of solar radius [9].

The ratio of the observed neutrino flux to the flux predicted by the Standard Solar Model was 0.3. The found neutrino deficit has been named “The Solar Neutrino Problem” which was resolved at Sudbury Neutrino Observatory (SNO) in 2002 [11]. SNO is a ring imaging Cherenkov detector located in the mine in Ontario, Canada. It is filled by heavy water D_2O . The detection of 8B solar neutrinos occurs through charge current (CC) and neutral current (NC) neutrino interactions with deuterium (20).



Electron neutrinos can be detected in a CC reaction, but the NC reaction gives the opportunity to detect all three neutrino flavors. The ability of the SNO experiment to detect all neutrino flavors along with the ability to distinguish both types of reactions solved the “Solar Neutrino Problem”. Results of SNO collaborations that are expressed in Figure 3 showed that summarized flux of all three neutrino flavors has not changed.

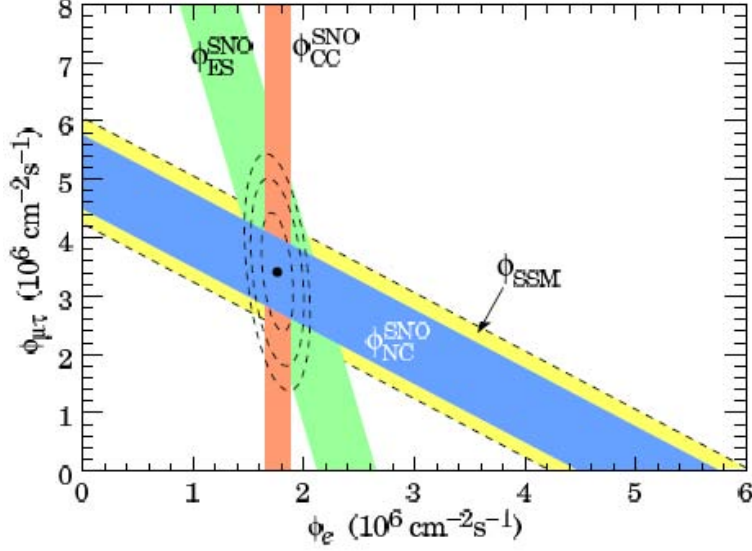


Figure 3: ^8B solar neutrino fluxes from different modes of neutrino detection [11].

The SNO collaboration also set the allowed region for the neutrino oscillation parameters [12]. These results are consistent with the recent results published by KamLAND collaboration [8] that will be discussed below.

1.2.2 Atmospheric neutrinos

Atmospheric neutrinos are produced by interaction of the cosmic rays with the nuclei in the atmosphere of the Earth. Primarily cosmic rays consist of about 90% of protons, 9% of helium and 1% of electrons. Interactions of cosmic rays with the nitrogen and oxygen nuclei in the atmosphere produce mesons, primarily pions and kaons. Decay of the charged pions $\pi^\pm \rightarrow \mu^\pm \nu_\mu (\bar{\nu}_\mu)$ is followed by the decay of the muons $\mu^\pm \rightarrow e^\pm \nu_e \bar{\nu}_\mu (\bar{\nu}_e \nu_\mu)$, coming from pion decay produce atmospheric neutrinos.

From the decay reactions it can be clearly seen that the expected ratio between muon neutrinos and electron neutrinos is 2 to 1. Recent results from the Super-Kamiokande (SuperK) collaboration show that the expected ratio $(\nu_\mu + \bar{\nu}_\mu)/(\nu_e + \bar{\nu}_e)$ is larger than that is observed. For the (sub-GeV) events it is equal to $1.32 \pm 0.03 \pm 0.07$ and for the (multi-GeV) events the ratio is equal to $1.4 \pm 0.06 \pm 0.2$ [13]. Super-Kamiokande has also observed the anomaly in zenith angle dependence. Figure 4 shows the zenith angle distributions of Super-Kamiokande events [14]. The results of the experiment were the first indication of the existence of neutrino oscillations. The SuperK atmospheric neutrino study gave the possibility to obtain the possible regions for the neutrino oscillation parameters $\sin^2\theta_{23}$ and Δm_{23}^2 (see Figure 5) [15].

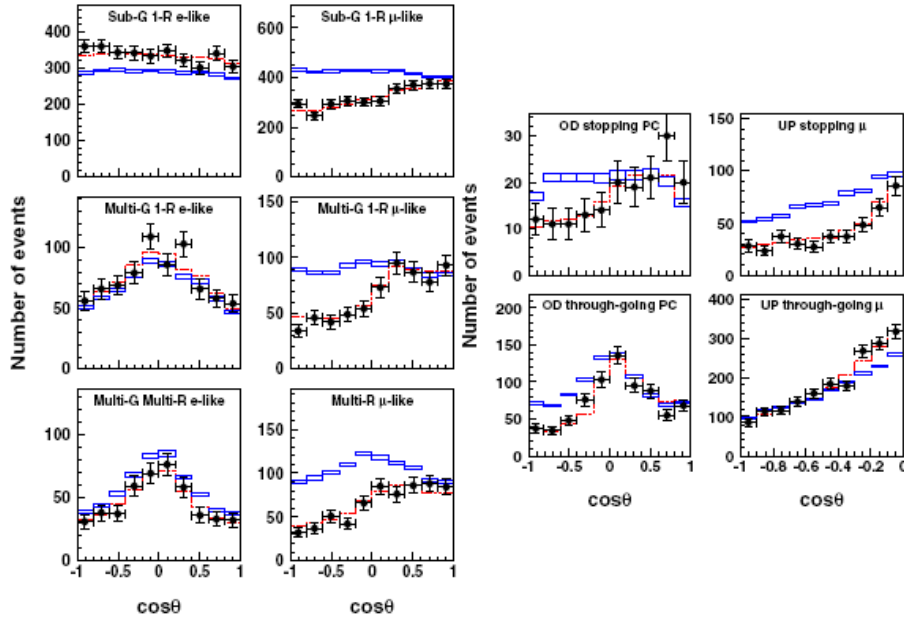


Figure 4: Zenith angle distributions of e-like, μ -like and UP μ are shown for data (filled circles with statistical error bars), Monte-Carlo distributions without oscillations (boxes) and best fit with oscillations distributions (red dashed). These distributions show the azimuth angle anomaly observed by SuperKamikande.

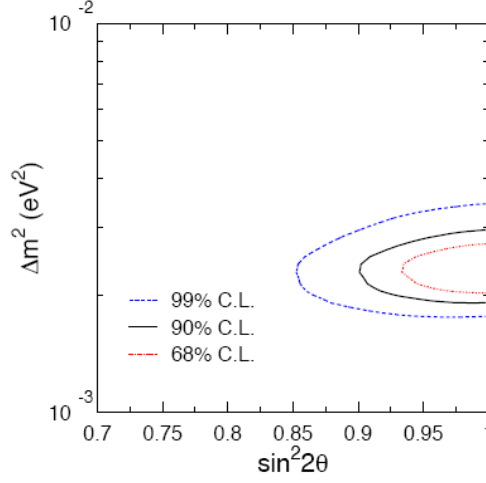


Figure 5: SuperKamiokande neutrino oscillation parameters $\sin^2 2\theta_{23}$ and Δm_{23}^2

1.2.3 Reactor neutrinos

Nuclear power plants are abundant source of neutrinos. Electron antineutrinos are emitted by the products of the fission of isotopes of uranium and plutonium (^{235}U , ^{238}U , ^{239}Pu , ^{241}Pu). Antineutrinos are produced through the β -decay chains. The spectrums of the antineutrinos coming from reactors from different fuel elements are shown in Figure 6. Although the energy spectra of the reactor neutrinos extend up to 10MeV the flux of the neutrinos with energy above 8MeV is very small compared to the neutrinos coming from the Sun within this energy window. It gives us the opportunity to search for the ^8B neutrinos with the energies $E_\nu < 15\text{MeV}$. One of the most successful reactor neutrino detectors KamLAND was designed to verify the disappearance on electron antineutrinos produced by nuclear reactors. In 2002 KamLAND has reported the first evidence of reactor neutrino disappearance [19]. Latest KamLAND results are represented in Figure 7, which shows the reactor neutrinos' survival probability dependence on L/E ratio, where L is the distance between neutrino source and detector and E is the neutrino

energy. Based on the reactor antineutrino disappearance study the KamLAND collaboration set the values for oscillation parameters $\tan^2\theta_{12}=0.56$ and $\Delta m_{21}^2=7.59\times 10^{-5}$ eV² [8]. The allowed region for these parameters is shown in Figure 8 [8].

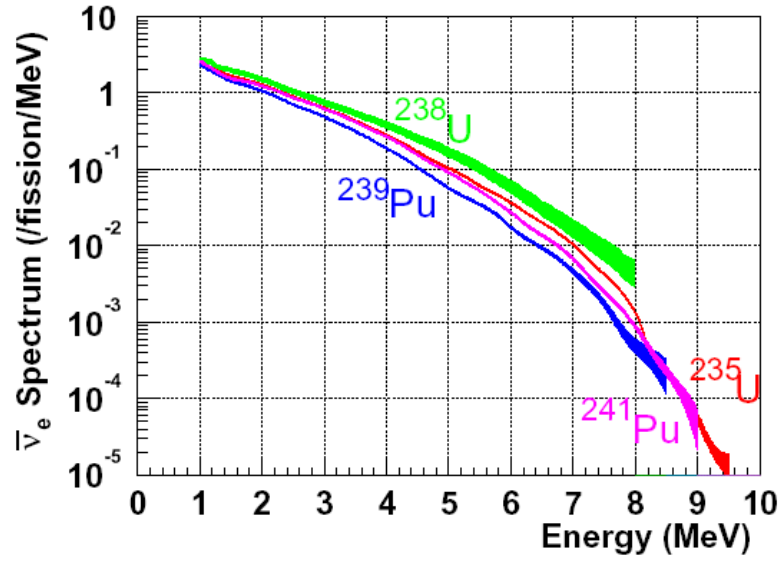


Figure 6: Anti-neutrino energy spectrums from the following isotopes: U235:[16], Pu239,241:[17], U238:[18].

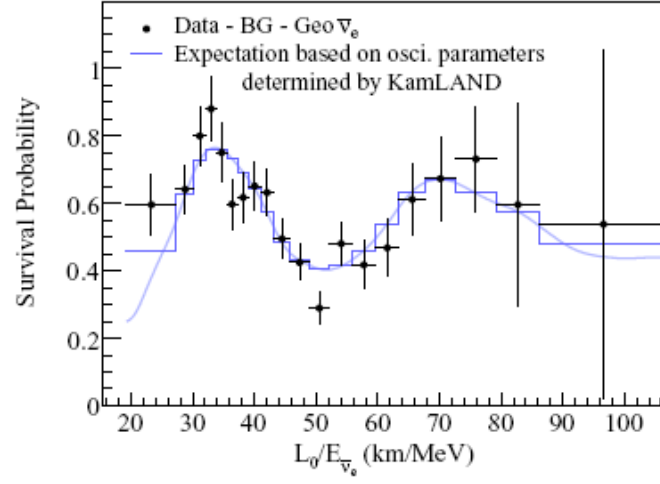


Figure 7: The ratio of the background subtracted electron antineutrino candidates including the subtraction of geo-neutrinos to no-oscillation expectations as a function of L_0/E , where $L_0=180$ km is effective baseline taken as a flux-weighted average [8]. Blue line shows the expectation based on KamLAND oscillation parameters and experimental points are black.

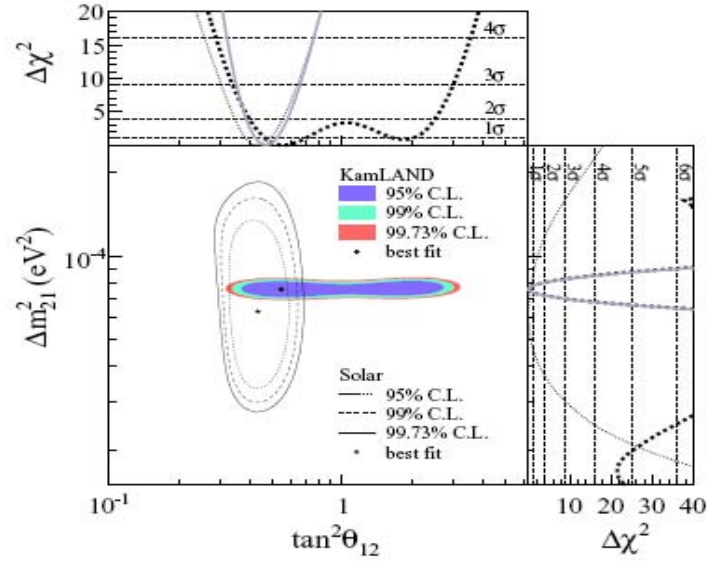


Figure 8: Allowed region for neutrino oscillation parameters from KamLAND and solar neutrino experiments

Chapter 2

KamLAND Detector

KamLAND is a Kamioka Liquid Scintillator Anti-neutrino Detector built in Japan in the Kamioka mine 1000 meters beneath Mt. Ikenoyama by KamLAND Collaboration. The layout of the KamLAND experimental site is represented in Figure 9. Primarily it was designed to detect electron antineutrinos from the Japanese commercial nuclear power plants. KamLAND detector and nuclear plants locations are shown in Figure 10.

2.1 Inner detector

The main volume of the inner detector is a nylon balloon with 6.5 meters radius that is filled with 1 kiloton of organic liquid scintillator (LS). This volume is used for the electron antineutrino detection. A balloon with LS is supported by Kevlar ropes and it is submerged into the buffer oil (BO) filled inside the stainless steel sphere with a radius of 9 meters. The scintillator composition is 80.2% of normal paraffin (Dodecane: $C_{12}H_{26}$), 19.8% of pseudocumene (C_9H_{12}) and 1.52 g/liter of PPO ($C_{15}H_{11}NO$). The PPO was used as a fluorescent material. The H/C ratio is 1.969 and the density is 0.778 g/cm^3 . The buffer oil is a mixture of dodecan and isoparaffin with a density which is 0.04% less than the liquid scintillator to maintain the balloon shape. BO is used as a support for the main volume filled with LS and to protect it from external radiation mainly coming from the wall and photo multiplier tubes (PMT). Since BO has no fluorescent material in its structure only Cherenkov light can be produced in this region of the detector. The KamLAND detector is subdivided into two independent sensitive volumes: inner detector (ID) and outer detector (OD). Figure 11 shows the KamLAND detector components. The liquid scintillator can produce light due to both scintillation and Cherenkov radiation.

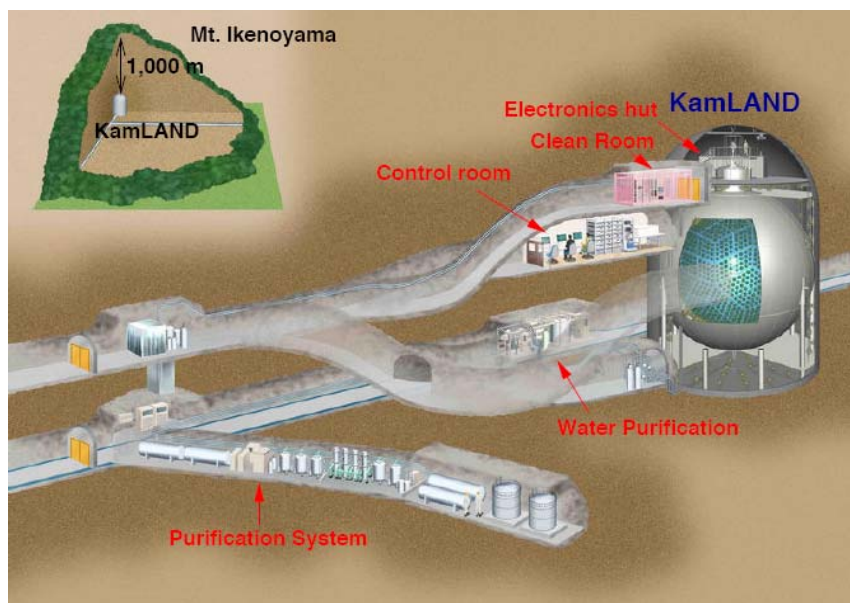
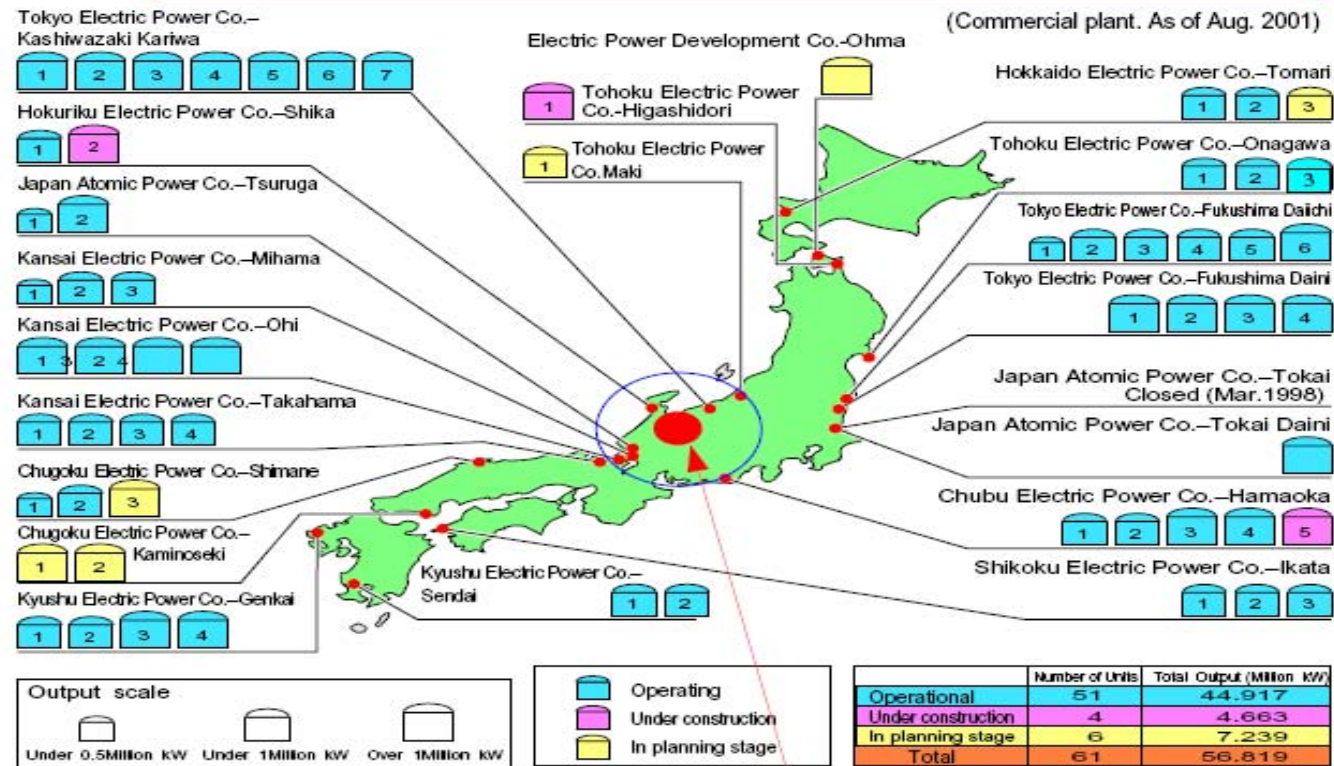


Figure 9: Scheme of the KamLAND experimental site

Nuclear Power Stations in Japan



KamLAND

Figure 10: Nuclear power plants and KamLAND location

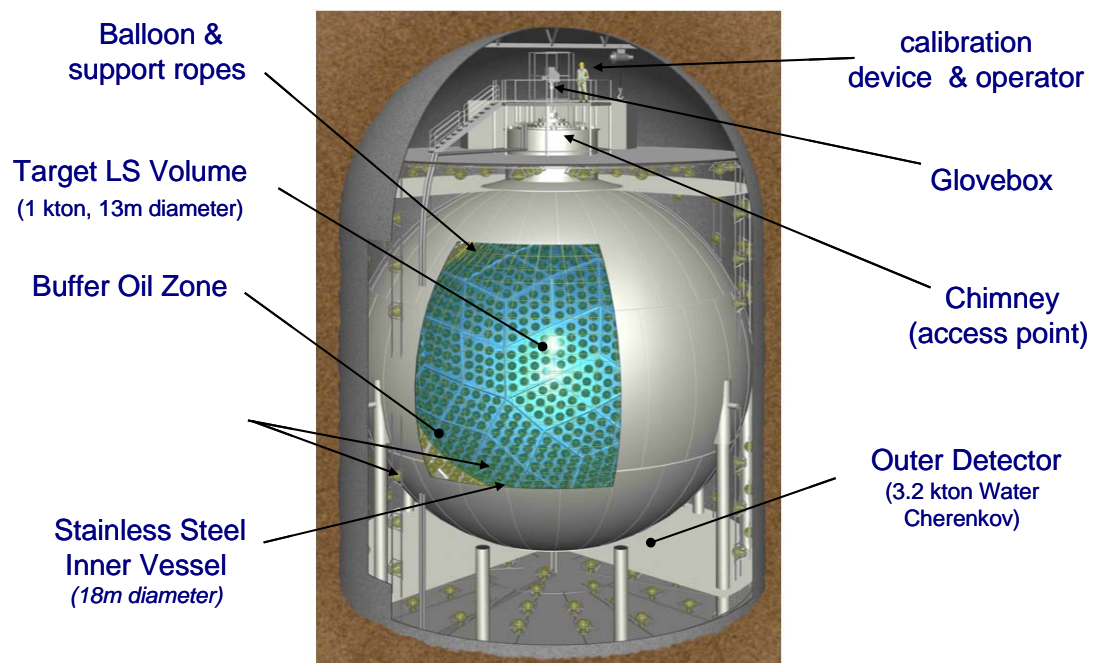


Figure 11: KamLAND detector design

During the filling process liquid scintillator (LS) and buffer oil (BO) had passed the water extraction process along with nitrogen purging to reduce the radioactive impurities that could cause the background. Detection of light produced in ID occurred by means of 1325 17" new Hamamatsu custom-designed PMTs and 554 20" PMTs that have been previously used by the Kamiokande experiment. PMTs are mounted on the inner wall of the stainless steel sphere. Summarized photo-cathode coverage of both PMT's types is 34%. The quantum efficiency of the PMTs is about 22% for the light of wavelength span of 300-500nm.

2.2 Outer Detector

The outer detector (OD) is separated from the ID by the stainless steel sphere. It has a cylindrical shape. OD is filled with 3.2 kilotons of water and used as a Cherenkov veto detector. Ultra-purified water refills the outer detector constantly maintaining the temperature of the liquid scintillator. Although the cosmic rays flux is significantly suppressed by the 1km layer of rock that surrounded the detector the remaining flux along with radioactivity from the rock can contribute to the background in the inner detector. Cosmic muon flux in the KamLAND detector is about 0.3 Hz. All events detected in ID accompanied by signal in the veto detector are considered as background events. OD light is detected by 225 20-inch Hamamatsu photomultiplier tubes (PMT).

2.3 Front-End Electronics and Trigger System

The main components of the KamLAND Front-End Electronic (FEE) are the Analog Transient Waveform Digitizers (ATWD). ATWD chips were custom-designed at Lawrence Berkeley National Laboratory. Each ATWD chip is connected to a PMT to convert the output voltage to the digital waveforms. Each waveform is 200 ns long and is triggered by the discriminator with a threshold about 1/3 of a photoelectron. It takes 25 microseconds for the ATWD to digitize the analog signal. To reduce the dead-time two

ATWD chips are connected to each phototube. Obtained waveforms are digitized by the ATWD and used for future analysis of events. In order to reduce the amount of data to be stored the special selection procedure is required. The aforementioned selection procedure is mediated by a trigger system. The trigger system sends an acquisition signal to the FEE modules to start conversion of analog waveforms using ATWDs. Every 25nsec the trigger system sends a clock signal to each FEE module to synchronize them. Every clock-tick trigger system summarizes the number of PMTs produced signal in the different regions of detector. For the outer detector different thresholds are set for the top, upper, lower and bottom regions. The corresponding thresholds are 6, 5, 6 and 7 PMT hits. For the inner detector two different thresholds are set during the regular “physics” runs. 200 PMT hits threshold is set for the prompt event. During 1msec after the prompt event 120 PMT hits threshold is set for the delayed events. These types of events will be discussed in paragraph 2.4. If the obtained sums exceed set threshold the trigger system issues the data acquisition signal.

2.4 Antineutrino detection

Detection of antineutrinos in KamLAND is based on the interaction of neutrinos with a liquid scintillator. To be more specific, antineutrinos interact with the hydrogen by means of an inverse β -decay reaction. This process gives two correlated events, a so-called “prompt event” and “delayed event”. The prompt event is the result of an inversed β -decay reaction (21). The threshold for this reaction is 1.8MeV (22). Prompt events are characterized by energy deposition of emitted positron and two gammas with energy of 0.511MeV coming from electron-positron annihilation.

$$\bar{\nu}_e + p \rightarrow e^+ + n \quad (21)$$

$$E_{threshold} = \frac{(M_n + m_e)^2 - M_p^2}{2M_p} = 1.806MeV \quad (22)$$

Thus, energy of incoming antineutrinos can be calculated from detected energy of positrons. Energy of recoil neutrons is negligible. The cross section of the electron antineutrino interaction on free proton is shown in Figure 12 and it is represented by (23).

$$\sigma_{\bar{\nu}_e + p \rightarrow e^+ + n} = 9.3 \times 10^{-44} \left(\frac{E_{\bar{\nu}}}{1 \text{ MeV}} \right)^2 \text{ cm}^2 \quad (23)$$

The delayed event is a result of neutron capture on proton. Emitted thermal neutron from inverse beta decay reaction is captured on hydrogen after $\sim 210 \text{ } \mu\text{sec}$ and it is accompanied by emission of 2.22 MeV gammas (24):



The observation of both prompt and delayed events gives a clear signature of the antineutrino detection. Spatial and timing coincidence of both events significantly reduces the accidental background. Schematically antineutrino interactions in KamLAND are shown in Figure 13.

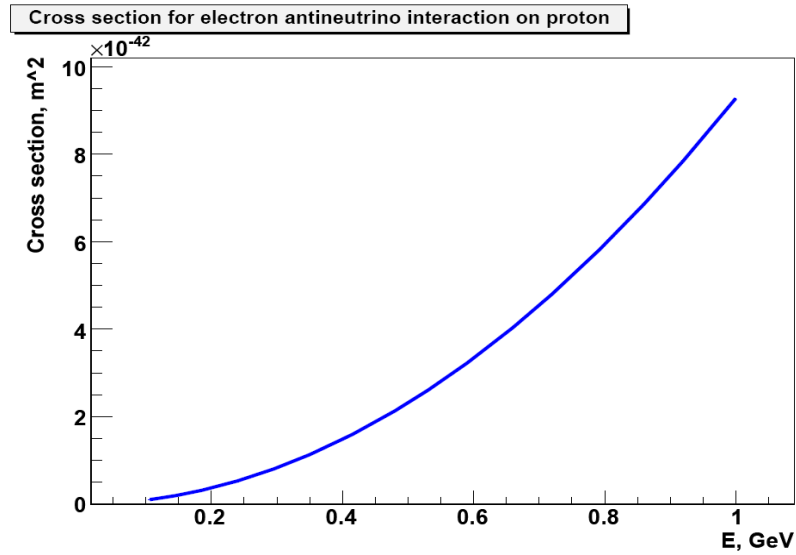


Figure 12: Energy dependence of cross section of electron antineutrinos interactions on free proton.

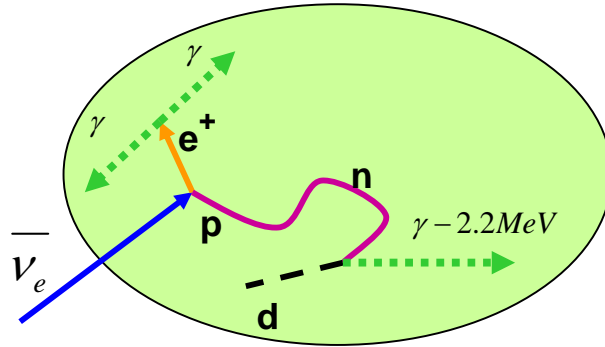


Figure 13: Antineutrinos interaction in KamLAND. Positron energy loss along with its annihilation gives prompt signal and neutron capture on proton gives delayed signal.

Chapter 3

Scintillator response and Energy Scale in KamLAND

The energy reconstruction procedure in KamLAND is based on the conversion of light detected by PMTs to the units of energy. Proper calibration of the detector is necessary to perform the correct energy reconstruction of observable events. Since the oscillation probability depends on L/E_ν it was of primary importance to calculate neutrino energy correctly.

3.1 Non-linearity of liquid scintillator

A non-linear response of the scintillator to calibration sources is a long standing problem in KamLAND. Calibration of the detector with the various γ -sources shows the strong non-linearity of the liquid scintillator response. Results of calibration with γ -sources are summarized in table 2 and a plot of non-linearity is shown in Figure 14.

Table 2: Expected and reconstructed (visible) energy for gamma calibration sources.

Calibration sources	Expected energy, MeV	Reconstructed energy, MeV
^{68}Ge	0.511×2	0.846
^{65}Zn	1.11552	1.021
^{60}Co	$1.173 + 1.333$	2.346
$n + p \rightarrow d + \gamma$	2.22457	2.211
$n + {}^{12}\text{C} \rightarrow {}^{13}\text{C} + \gamma$	4.9468	5.061
Am-Be	7.652	8.032

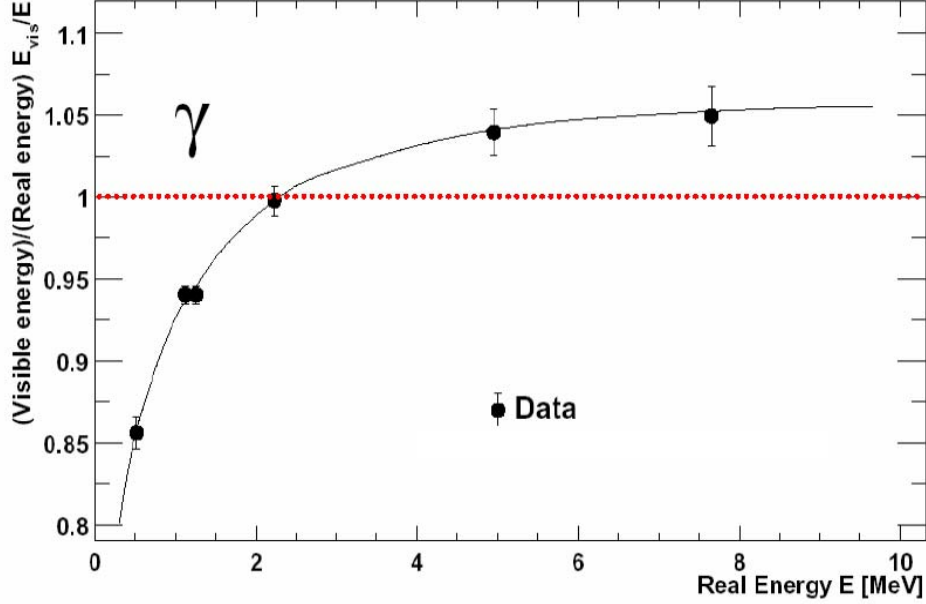


Figure 14: Observed non-linearity of energy scale, measured with calibration γ -sources represented by energy dependence of ratio between expected and real energy. The red line shows what is expected in case of the 100% linear response of the detector.

An understanding of the scintillator non-linearity plays an extremely important role for the energy reconstruction procedure of the observed events. This non-linearity can be explained with the contribution of two non-linear mechanisms: Birks' quenching and Cherenkov light absorption and reemission with detectable wavelength. Detailed studies in KamLAND have shown that both contributions are important to measure and account for correct energy reconstruction.

3.1.1 The Birks Law

In the 1950's J. B. Birks measured the scintillator response corresponding to different particles passing through a sensitive volume. During his measurements Birks noticed that energy deposited by particles in the scintillator volume is less than the initial energy of the incident particle and this effect is energy dependent on the particle energy

[22]. Based on the results of his measurements Birks introduced the empirical relationship between the expected energy deposition and that observed. Birks law is represented by (25).

$$\Delta E_{visible} = \frac{\Delta E_{expected}}{1 + k_B (dE / dx)} \quad (25)$$

3.1.2 Cherenkov light absorption and reemission

Cherenkov radiation is produced by a charged particle passing through the media with a velocity higher than the velocity of light in the same media. The direction of the Cherenkov radiation depends on the refractive index of the media and velocity of the particle. Created photons are contained in the cone around the trajectory of the particle. The acceptance angle of this cone can be obtained from (26).

$$\cos \theta_{max} = \frac{1}{n(p_{\gamma}^{max})\beta} \quad (26)$$

where β is the particle velocity in units of the speed of light and n is the refractive index that depends on the momentum of the Cherenkov photon. The number of photons produced by the particle is calculated from (27).

$$\frac{dN}{dx} \approx 370z^2 \int_{p_{\gamma}^{min}}^{p_{\gamma}^{max}} \left(1 - \frac{1}{\beta^2 n^2(p_{\gamma})} \right) dp_{\gamma} \quad (27)$$

where z is the charge of the particle in units of electron charge and p_{γ} is the momentum of the photons. The refractive index dependence on wavelength for the KamLAND liquid scintillator had been estimated by Prof. Yu. Kamyshkov. However Cherenkov light production occurs mainly in the 100-300nm wavelength range. These calculations were based on characterization of refractive indexes of each component of KamLAND scintillator mixture.

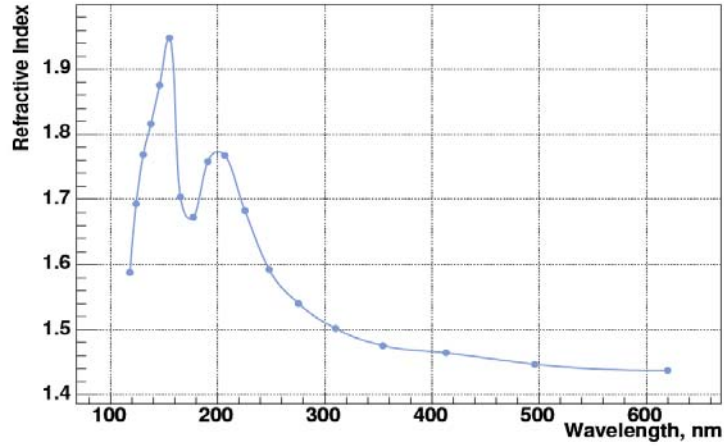


Figure 15: Wavelength dependence of KamLAND liquid scintillator refractive index.

KamLAND LS refractive index had been calculated mixing the indexes of each component of the scintillator [26], [27]. The obtained result is shown in Figure 15. PMTs in KamLAND are sensitive to the light with the wavelength higher than about 300nm. Figure 16 shows the typical quantum efficiency dependence on the wavelength. The main part of the Cherenkov light spectra belongs to the UV region. KamLAND LS is not transparent to the UV light and the produced photons are almost immediately absorbed by the scintillator. This absorption results in the redistribution of the excitation in the chain of molecular structure of the LS and it is followed by reemission of the photons with the wavelength transparent to the scintillator. The process of Cherenkov light absorption followed by reemission of light with the visible wavelength for the PMTs significantly increases the number of Cherenkov photons detected by phototubes. The study of Cherenkov light absorption and reemission had been performed by prof. Yury Kamyshev using a UV monochromator that allows focusing the specific UV wavelengths through MgF_2 window into the vessel with LS and measure the probability of the conversion UV to visible light. Figure 17 shows the reemission probability dependent on the wavelength of the absorbed Cherenkov light. The red and purple lines

represent the reemission probability for the scintillator and dark blue and blue for the dodecane. The probability is in arbitrary units. Reemission efficiency (quantum efficiency of PPO) around 300-350nm was quoted in Borexino experiment as 80%. This allows us properly normalize measured reemission efficiency.

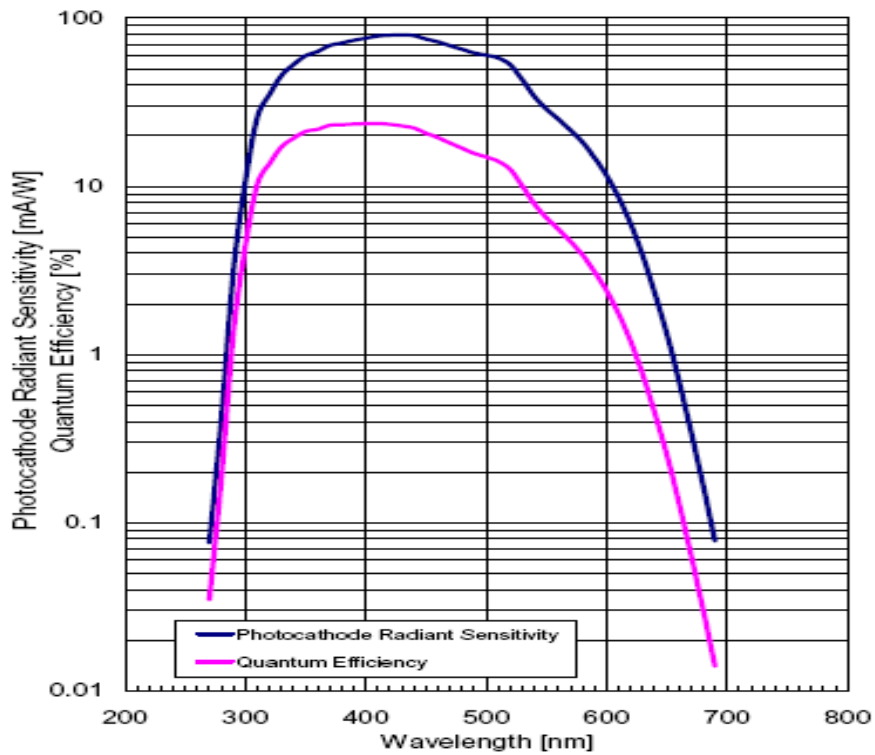


Figure 16: PMT photocathode quantum efficiency.

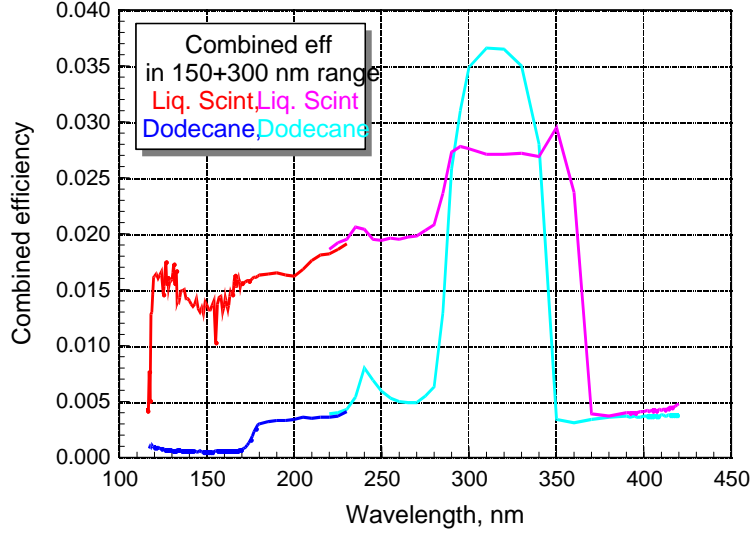


Figure 17: Probability of reemission of light dependence on absorbed light wavelength.

3.2 LS response to low energy electrons measured with a Compton Spectrometer

Calibration of the detector in KamLAND can be practically made only with gamma sources. However such a procedure does not calibrate the entire energy range of neutrino interactions and does not provide calibration for scintillator response to other particles that is different from response to gammas. To calculate the background caused by atmospheric neutrino interactions in KamLAND it is necessary to understand the scintillator response to other particles. In order to measure the LS response within 1MeV energy window to electrons a Compton Spectrometer has been built by our UT group. The idea of this study was to measure the LS response to low energy electrons and then based on obtained results of the measurements along with a Monte Carlo study including Cherenkov radiation simulation we would like to extract the Birks coefficient for the KamLAND scintillator and LS light yield. Both of these parameters together with

Cherenkov light reemission will allow us to calculate the LS response to the various particles.

3.2.1 Spectrometer Design

The Compton Spectrometer consists of a γ -source (1mCi ^{22}Na source with two 0.511MeV and 1.275MeV monochromatic γ -lines), target (liquid scintillator) and detector of scattered γ (NaI detector). A schematic of the Compton spectrometer and design are shown in Figure 18 and 19 respectively. The angular position of the NaI γ -detector determines the energy of the recoil Compton electron in the scintillator sample (28).

$$E_{e^- \text{ recoil}}^{\text{kin}} = \frac{E_{\gamma \text{ incident}}^2 (1 - \cos \theta)}{m_e + E_{\gamma \text{ incident}} (1 - \cos \theta)} \quad (28)$$

The ^{22}Na source allows measurements of the electron recoil energy in a wide range from 29 to 1000keV. In order to keep the angular dispersion small the NaI is positioned 1.6-m away from the target. The liquid scintillator had been sent directly from the KamLAND site in Japan and it was placed inside a quartz vessel shown in Figure 20. The vessel was placed upon the Hamamatsu PMT H1161. To provide better optical contact between the vessel and PMT glass Bicron optical grease was used. Contamination of oxygen in the liquid scintillator results in reduced light output. In order to minimize the amount of oxygen the scintillator was thoroughly purged with clean nitrogen before the measurements were started and then the target container was sealed using Teflon valves. The required volume of purged nitrogen was determined experimentally. Figure 21 shows the amplitude of the signal in the LS during the process of purification from oxygen. It is seen that the amplitude of the signal achieved a maximum when the volume of purged nitrogen was about 30 volumes of the scintillator. The result of our measurement is a ratio of measured visible energy to real energy determined from the angular position of the NaI and GEANT simulations.

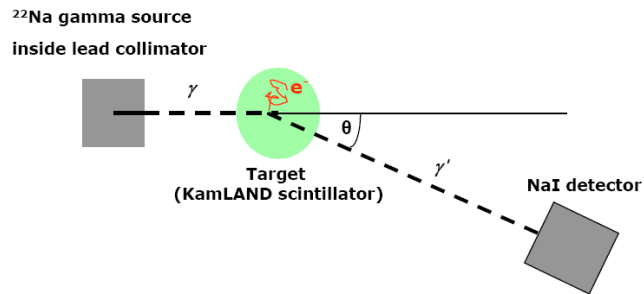


Figure 18: Scheme of the Compton Spectrometer

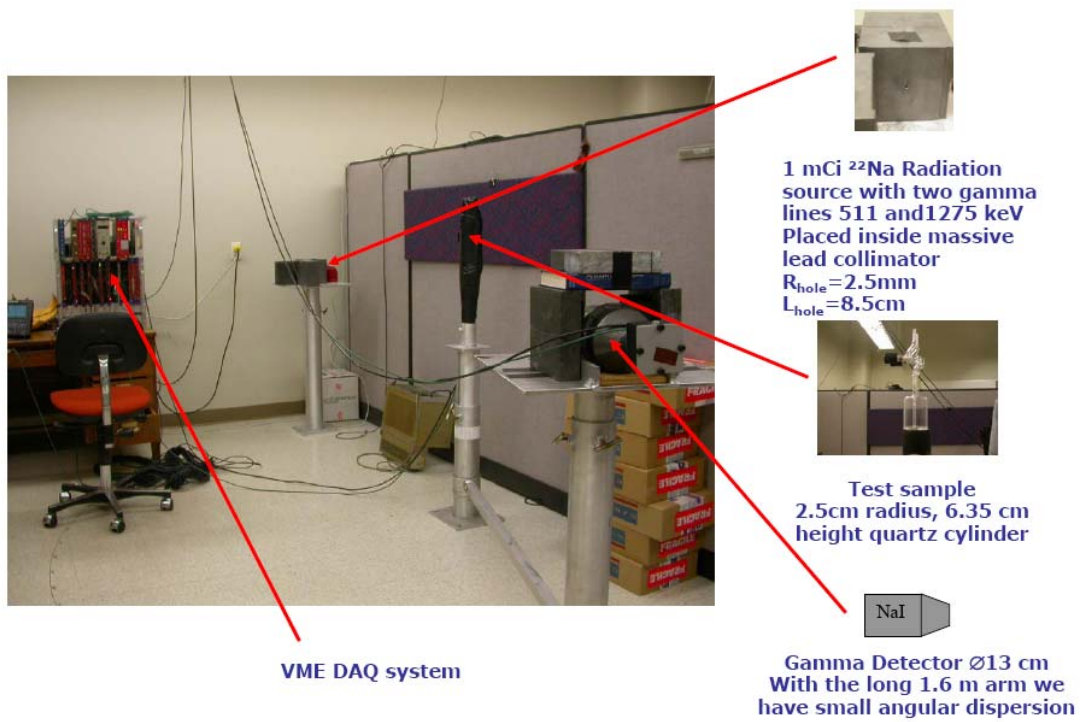


Figure 19: Compton Spectrometer Design

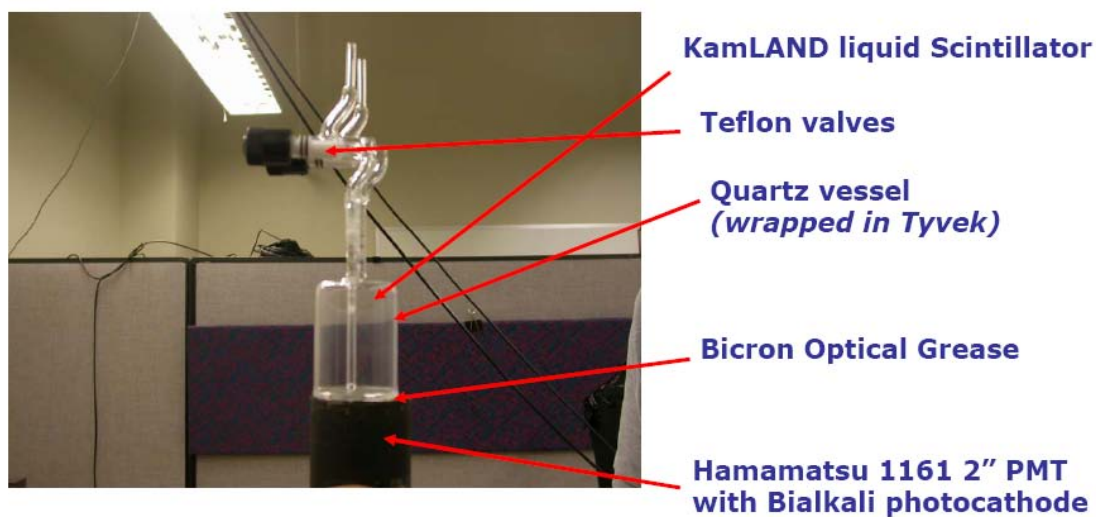


Figure 20: Quartz vessel for KamLAND liquid scintillator.

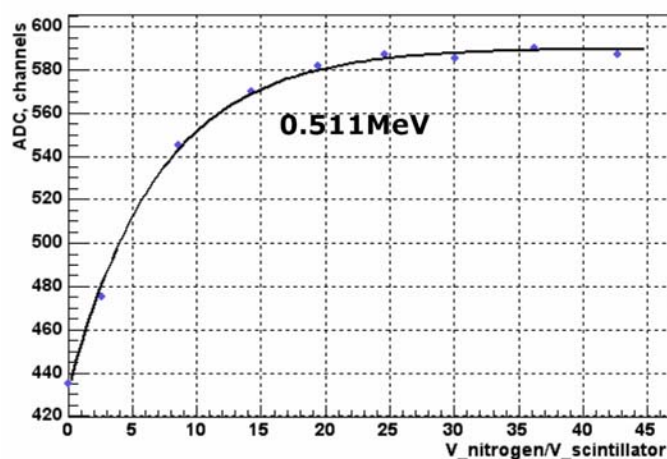


Figure 21: Amplitude of Compton peak from 0.511 MeV gamma line at scattering angle 30° versus volume of exchanged nitrogen

3.2.2 Light yield with and without Tyvek

In order to obtain maximum light collection the container with the liquid scintillator was wrapped in Tyvek - diffuse reflecting paper. Instead of leaving the target volume photons reflected from Tyvek eventually reach the PMT photocathode. The measurements of the amplitude of the signal from the liquid scintillator with and without Tyvek were performed for the 60 degrees NaI position. Figure 22 shows the amplitude of the signals from the LS for both gamma lines with and without Tyvek. The results are summarized in Table 3. As shown in Table 3 the light collection gain with Tyvek is 4.02. The ratio between deposited energies in the LS from different incident gammas with and without Tyvek remained the same 4.35. This result shows the linearity of the PMT and electronics.

Table 3: Summary of the measurements with and without Tyvek

	No Tyvek		Tyvek	
Incident gamma E, MeV	0.511	1.275	0.511	1.275
Mean, ch.	119.8	522	482	2096
Sigma, ch.	34.01	118.1	59.82	151.8

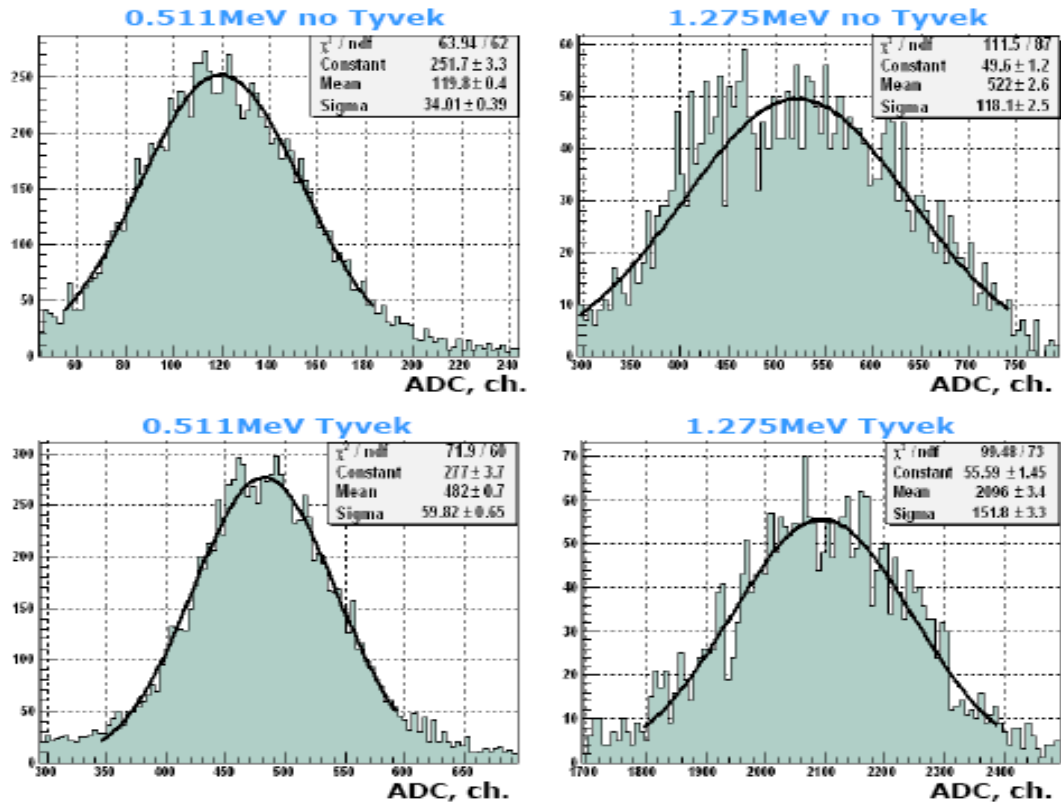


Figure 22: Amplitude of signal in the LS with and without Tyvek for 0.511MeV and 1.275MeV gamma lines at 60 degrees NaI position.

3.2.3 Spectrometer Alignment

Alignment of the Compton Spectrometer is a very important part of the experiment. Misalignment can cause a false non-linearity of the scintillator response. It is clearly seen in Figure 23 how even a small misalignment of the NaI detector can affect a difference in energy deposition. For example at 30 degrees position of the NaI detector one degree difference in angular position results in about 4% variation in deposited energy by electron recoil coming from the incident 1.275MeV gamma. Angular position of the NaI detector was accomplished using theodolite to an accuracy of better than 0.1 degrees. Alignment of the direction of the collimator with respect the 0 degree position of the NaI detector was performed manually by rotation of the lead container with the radiation source. The alignment procedure for the collimator and results of the alignment are shown in Figure 24. Measurements of the event rate in the NaI detector with different displacement around the 0 degree point were made for the different directions of the collimator. After alignment the accuracy of the collimator directionality became 0.04 degrees

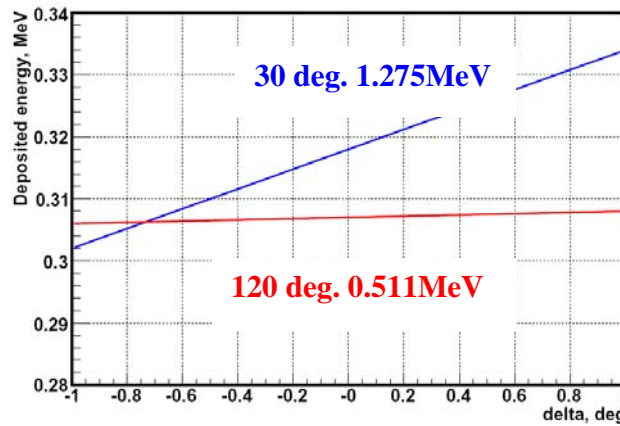


Figure 23: Deposited energy in the LS as a function of angular deviation from real angular position of the NaI detector. Blue line is deposited energy by recoil electron for 30 degrees NaI position and incident 1.275MeV gamma. Red line is deposited energy of the recoil electron for 120 degree NaI position and incident 0.511 MeV gamma.

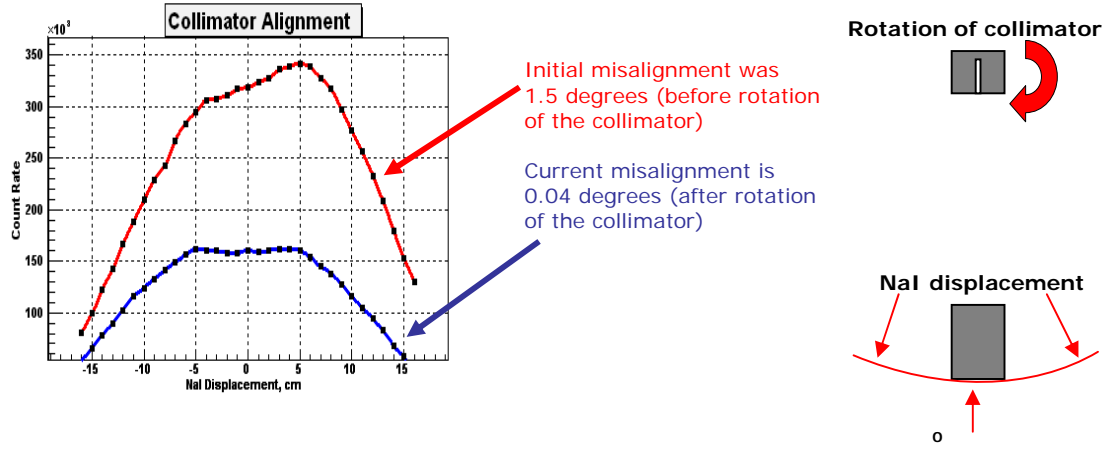


Figure 24: Collimator alignment procedure with respect of 0 degrees position of NaI detector and measurements of the event rate in NaI for different displacement of the NaI. Red line – before alignment and blue line – after alignment procedure

3.2.4 Monte Carlo Simulation of the Real Energy

Real energy of the recoil electron calculations was performed using the Detector Description and Simulation Tool (GEANT). The simulation was performed disregarding the energy quenching in the liquid scintillator and Cherenkov light detection. This energy can not be calculated by simple usage of the Compton formula since the Compton Spectrometer has its own non zero resolution. The resolution of the spectrometer consists of two components: geometrical resolution due to angular dispersion and resolution due to the light collection statistics.

During the Monte Carlo simulation the exact physical and geometrical properties of the Compton Spectrometer was described in order to define the energy deposition in the liquid scintillator. Errors in the energy deposition were about 0.2%. The difference in energy deposition in LS between MC and Compton formula is up to 0.9%. The calculated real energy for both gamma lines is dependent on angular position of the NaI detector as shown in Figure 25.

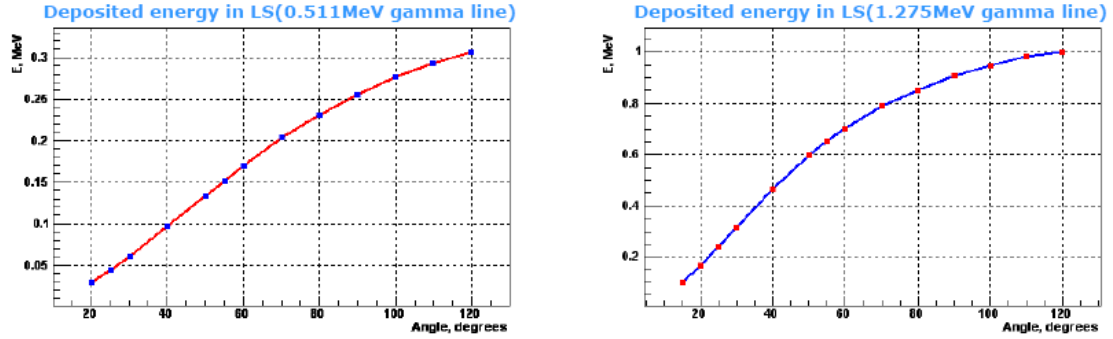


Figure 25: Real energy deposited in LS by recoil electron for the different angular position of the NaI detector. Right plot is for the 0.511MeV incident gamma and left plot is for 1.275MeV gamma.

3.2.5 Events selection in measurements of non-linearity

Figure 26 shows the typical correlation between energy deposited in the NaI detector and in the liquid scintillator for the determined position of the NaI detector. These plots were made using data sets obtained from the real measurements and from the Monte Carlo simulation. Figure 26 clearly shows peaks corresponding to electron recoil for both gamma lines, backscattering in the NaI detector and double Compton scattering region. The distribution of the recoil electron energy deposited in the LS for both gamma lines is shown on Figure 27 for the real data and MC simulation at 70 degrees angular position of the NaI detector. It can be found that the ratio between peaks corresponded to the different incident gammas in MC and in real data is not the same as that explained by the energy quenching in the liquid scintillator. Energy cut of the events in the NaI detector let us clearly select the energy deposited by the recoil electron in the test sample. The distribution of the energy deposited in the scintillator before and after energy cut of the events in the NaI detector at 30 degrees angular position is shown in Figure 28.

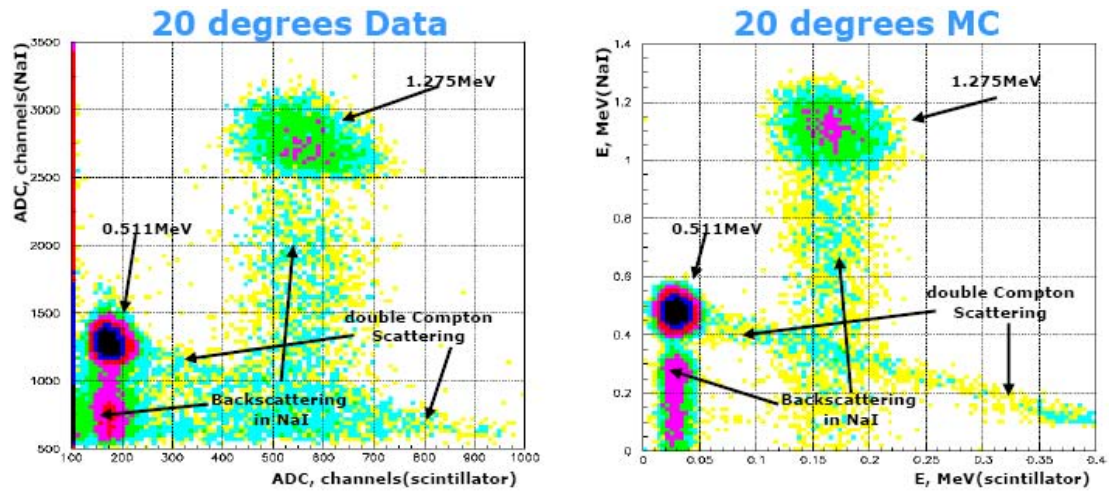


Figure 26: Correlation between energy deposition in the NaI detector and LS at the 20 degrees angular position of the NaI. The left plot corresponds to the real measurements and the right one to the Monte Carlo simulation.

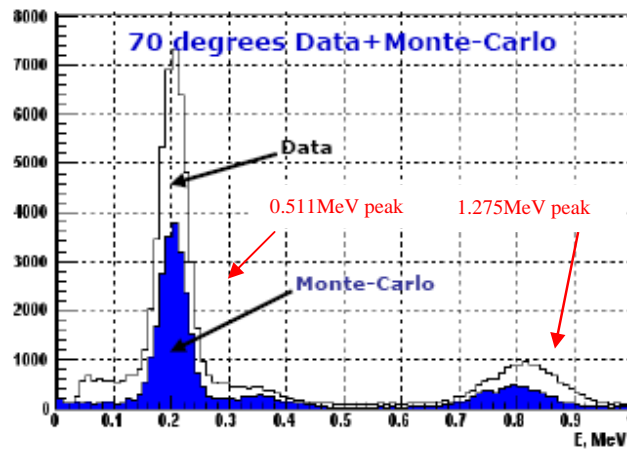


Figure 27: Distribution of the recoil electron energy in the LS for both incident gammas at 70 degrees angular position of the NaI detector. The blue histogram shows the MC result and the white shows real data.

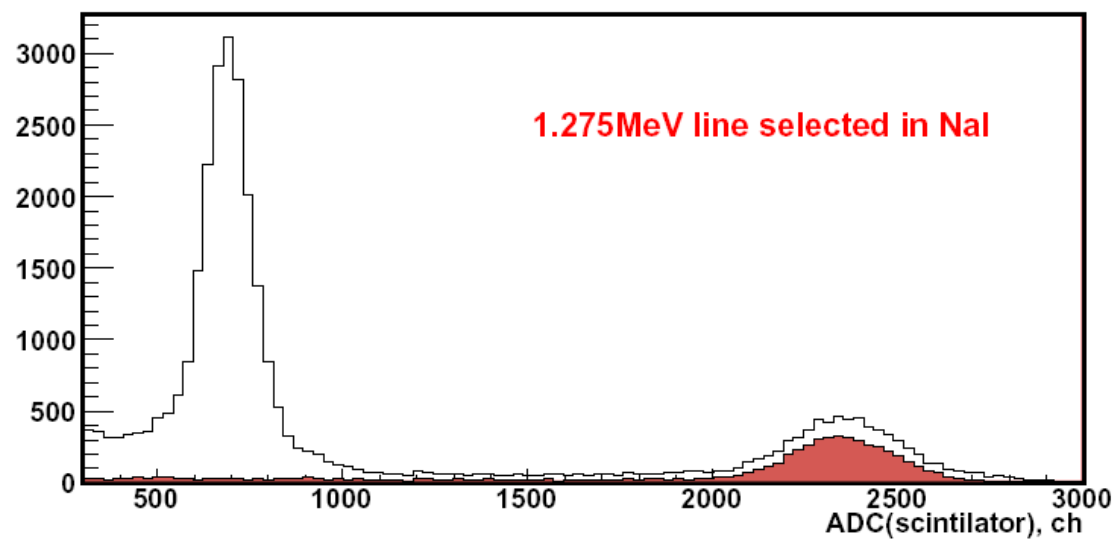
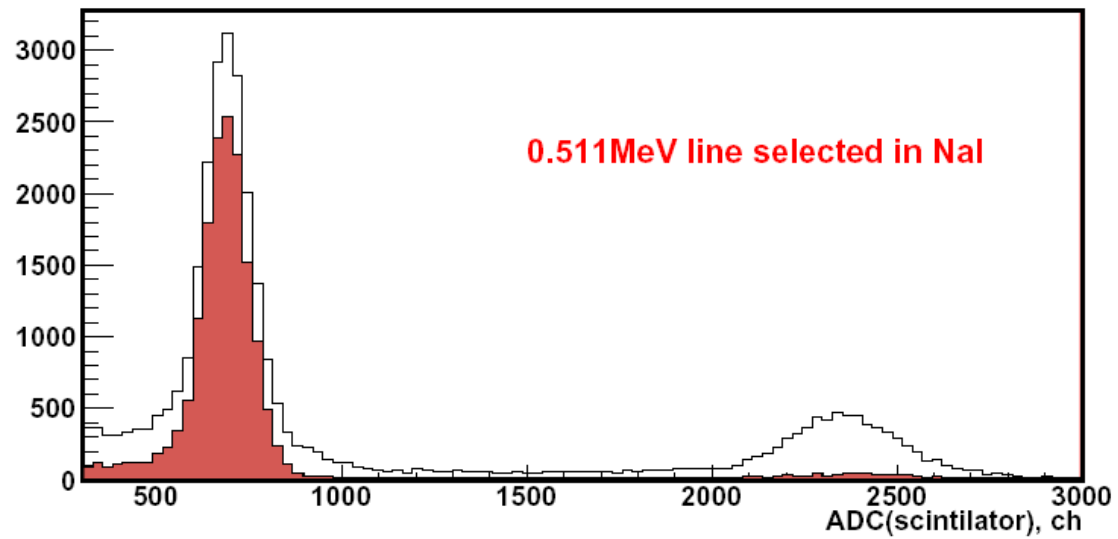


Figure 28: Selection of the energy deposited in the LS by recoil electrons coming from incident gammas with the different initial energy. White histogram – before energy cut in the NaI and red – after energy cut in the NaI.

3.2.6 LS response to low-energy electrons (Final Result)

The results of our measurement of the liquid scintillator response to low energy electrons is presented in terms of the ratio of measured visible energy to the real energy determined from the angular position of the NaI detector and GEANT simulations. The observed non-linearity of the KamLAND scintillator is shown in Figure 29. Our measurement covered the energy range between 0.029MeV and 1MeV. Maximum non-linearity is up to 19% at 0.029MeV data point. The systematic errors are 0.5%.

3.3 Monte-Carlo study of non-linearity

Measurement of the liquid scintillator response to low energy electrons with the Compton Spectrometer covers only the energy range below 1MeV. The idea of the Monte-Carlo study was to build a model that could reproduce the measurement made with the Compton Spectrometer to understand the physical processes caused energy quenching in the liquid scintillator.

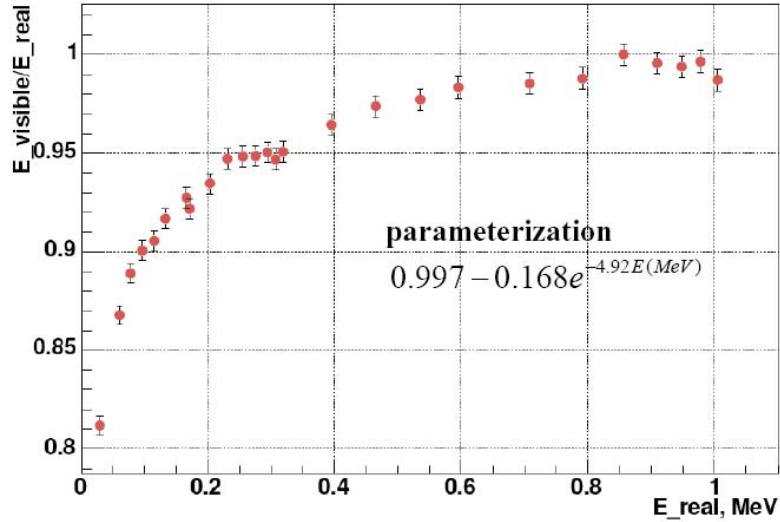


Figure 29: Liquid scintillator non-linear response to low-energy electrons measured as a ratio between visible and real energy of the recoil electron as a function of real energy.

If this can be achieved, then based on the parameters extracted from the Monte-Carlo study we can understand the LS response to the energies up to 15MeV that corresponds to the energy range of antineutrinos from the Sun. It is also very important to calculate the background caused by atmospheric neutrino interactions in the KamLAND detector. Since the products of such interactions are positrons, protons, gammas, alphas it is important to know the LS response to these particles. The same MC model can be applied to understand this response.

The Monte-Carlo model is based on the assumption that non-linearity in the LS could be caused by Birks' quenching and Cherenkov light contribution. During this MC simulation the visible energy was calculated as (29) and then the ratio between visible and real energy was calculated as a function of the real energy.

$$E_{visible} = k \cdot (E_{deposited} \cdot m + N_{Ckov}) \quad (29)$$

Where $E_{deposited}$ (depended on real energy) is the energy deposited by particles taking into account the Birks' Law, m is a conversion of deposited energy to the number of photons, N_{Ckov} is number of Cherenkov photons detected and k is a conversion factor for the summarized scintillation and Cherenkov photons to the energy.

The Monte-Carlo procedure consisted of two parts: calculation of the number of Cherenkov photons detected and calculation of the deposited energy taking into account Birks' Law. The MC simulation was performed using the GEANT3 program.

3.3.1 Cherenkov photons detection

Using the GEANT program the geometrical, physical and optical properties of the target volume container had been described. According to the Compton formula (28) the kinetic energy of the recoil electron is determined by the initial energy of the gamma and angle of scattering. During the measurements with the Compton Spectrometer the angular position of the NaI detector determined the initial kinetic energy of the recoil electrons. Cherenkov photons were produced by the electrons passing through the target volume.

The initial energies of the electrons corresponded to the same angular positions of the NaI detector that were used during the Compton Spectrometer measurements. The initial positions of the electrons were randomly distributed inside the target volume. The process of Cherenkov light absorption and reemission explained in paragraph 3.1.2 had been implemented in the Monte-Carlo simulation. Figure 30 shows the initial spectra of the Cherenkov photons produced by the electrons with the different initial energies. These spectra were normalized to one electron. The shapes of the Cherenkov spectra correspond to the shape of refractive index of the LS as a function of the wavelength of light (see Figure 15). The PMT is sensitive to light with a wavelength above 300nm, but shorter than 600nm. Figure 30 clearly shows that for electrons with energies below 0.2MeV there is no Cherenkov light produced in the PMT sensitive region. In addition, even for electrons with the higher energies most of the Cherenkov light spectra have wavelengths below 300nm. Since in a real experiment the process of Cherenkov light absorption and reemission into the PMT sensitive region occurs, as described earlier, it is vital to take into account this process during the Monte-Carlo study in order to calculate the exact number of detected photons. The effect of the reemission process can be seen on Figure 31, which shows the Cherenkov light collection with and without reemission of light as a function of initial kinetic energy of the electron. Reemission mechanism results in 3.7 times gain in light yield at 1MeV kinetic energy of electron.

The Cherenkov photons experienced multiple reflections from the Tyvek covered the target volume walls. For the MC simulation Tyvek reflectivity was assumed to be 95%. After absorption and reemission photons can be detected by the PMT. The integrated quantum efficiency of the PMT is 20%. Overall, taking into account the described processes and PMT quantum efficiency the total detection efficiency of the Cherenkov light is 3.6%.

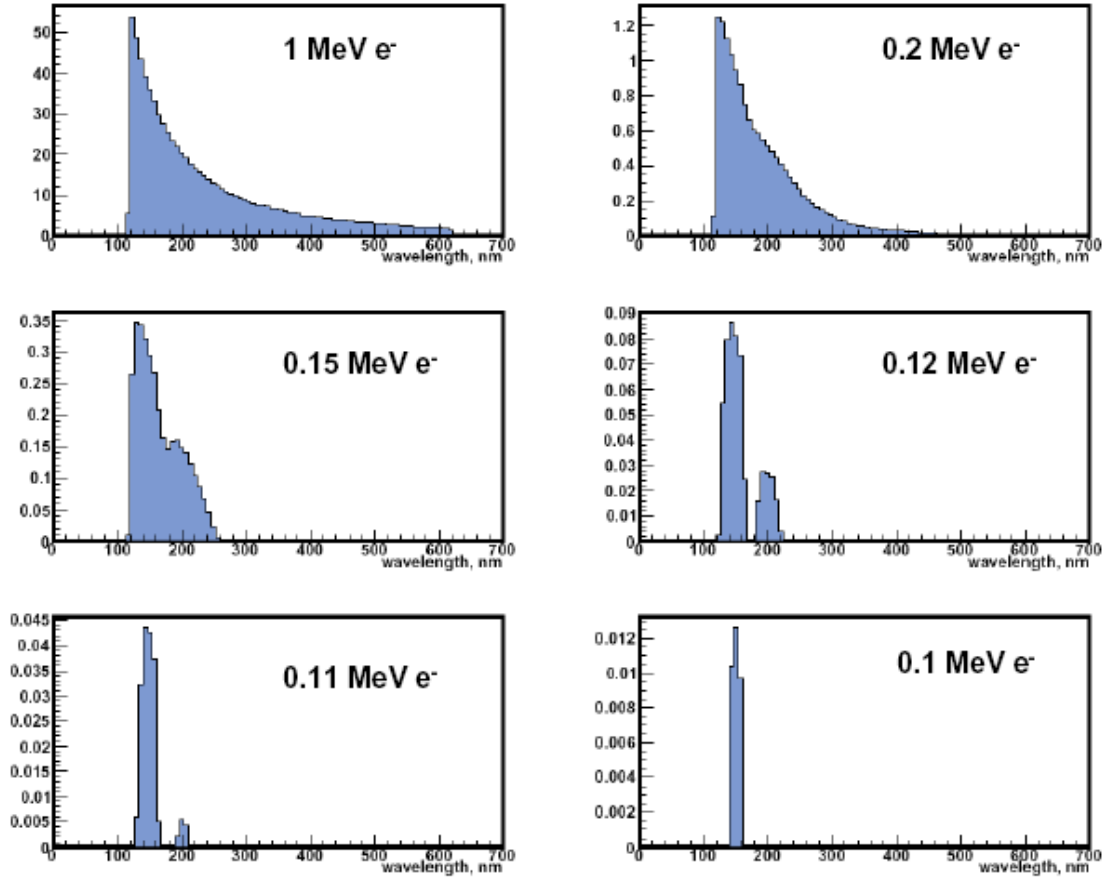


Figure 30: Initial spectra of the Cherenkov light produced by electrons with different initial kinetic energies. Spectrums are normalized to one initial electron.

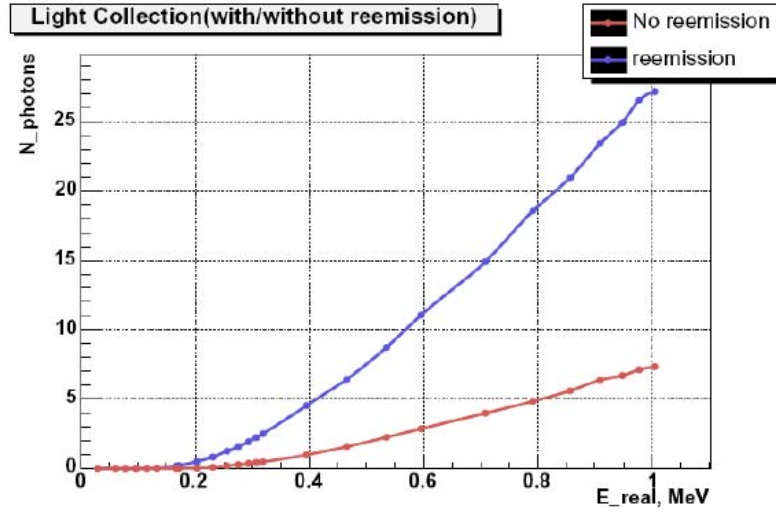


Figure 31: Cherenkov light collection with and without reemission as a function of kinetic energy of electron. Red line represents the light collection without reemission mechanism and the blue line light collection taking into account reemission process.

3.3.2 Calculation of deposited energy with different Birks' coefficients

During this part of the simulation procedure the geometry and physical properties of the target volume were the same as for the Cherenkov light detection study except the process of Cherenkov light production had been disabled. Initial energies of the electrons were the same as had been used during the Compton Spectrometer measurement. To achieve the best performance of the Monte-Carlo, the parameters of GEANT had been modified to track the electrons with the small step in order to keep dE per step size as small as possible. The GEANT program performs particle tracking down to 2-3keV kinetic energy. Due to the fluctuations in dE/dx at energies close to this threshold and strong dependence on the size of each step it was decided to use dE/dx calculated with parameterization [23], [24] instead of using regular GEANT procedure for the energies below 30keV. The calculation of deposited energy by recoil electron was made using different Birks' coefficients.

3.3.3 Monte-Carlo study results

Combination of the Cherenkov light detection results along with energy deposition for different Birks' coefficients was used to obtain the visible energy (29) and the ratio between visible and real energies as a function of real energy. Minimization of the χ^2 (30) and variation of the Birks coefficients along with variation of scintillation light output was used to obtain the same shape of nonlinearity measured with Compton Spectrometer.

$$\chi^2 = \sum_{i=1}^N \frac{(x_i - y_i)^2}{\sigma_i^2} \quad (30)$$

Where x_i is a ratio measured by the Compton Spectrometer, y_i is a ratio obtained from Monte-Carlo and σ_i is the error of the Compton Spectrometer measurement.

Figure 32 shows the possible regions of the Birks coefficients and scintillation light output for the different confidence levels. In order to reduce the time consumption of the MC procedure the variation of the Birks coefficients was made with relatively large steps. As a result the plot in Figure 32 is rather more discrete than continuous. The best Birks' value is $K_B = 0.01072^{+0.0012}_{-0.0005}$ [g/(MeV·cm²)] and the best scintillation light output is 609^{+110}_{-80} photons/MeV.

Independently from the Monte-Carlo study the scintillation light output was calibrated using the single photo electron measurement. The scheme of the calibration setup is shown in Figure 33. Light electric diode (LED) connected to the same PMT that had been used for the non-linearity measurement through the optical fiber. The amplitude of the signal coming from pulse generator is adjusted in order to detect single photoelectrons by the PMT. For the scintillator non-linearity study 1250V was applied on the PMT. However it was impossible to detect single photoelectrons using the same high voltage and for this measurement the voltage was increased to 1600V. The signal from the PMT is digitized by the amplitude digital converter (ADC) which is not the same as used for the Compton Spectrometer measurement.

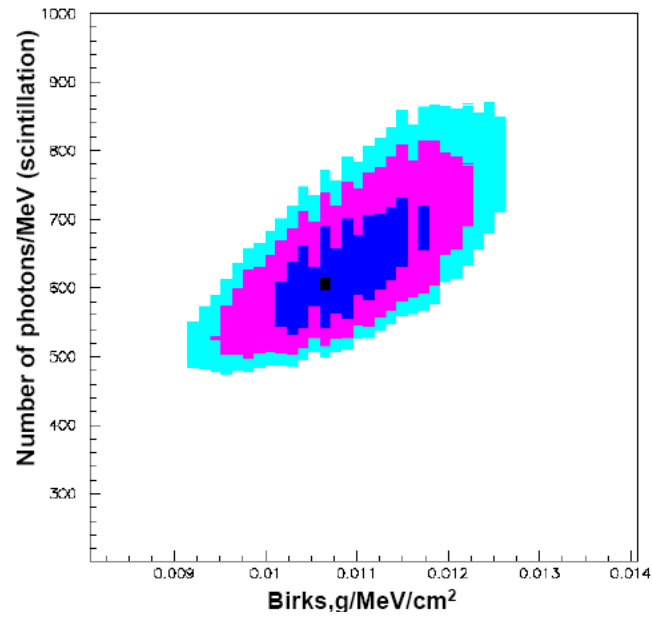


Figure 32: Possible parameter region of the Birks coefficients and scintillation light output for the C.L. 99%, 95% and 90%. Black point corresponds to the minimum χ^2

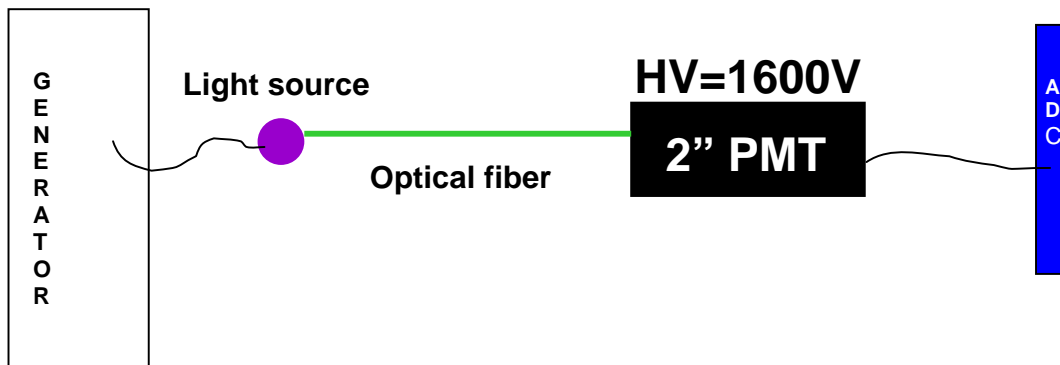


Figure 33: Scintillation light output calibration setup

In order to correctly calculate the scintillation light output during the LS measurements the PMT gain and different sensitivity of the ADC have to be taken into consideration. In order to calculate gain between 1600 and 1250V the amplitude of the signal from the LED was adjusted to be able to measure it with both voltages. Figure 34 shows the distribution of the PMT signals at 1250 and 1600V. Calculated gain between 1600 and 1250V is 7.65. Then the amplitude of the LED signal was reduced to measure a single photoelectron with 1600V. The PMT signal distribution corresponding to a single photoelectron is shown in Figure 35. The sensitivity of the ADC during this measurement was 0.25pC/count and ADC sensitivity for LS study was 0.1pC/count. The scintillation light yield was calculated using the single photoelectron amplitude and taking into account the PMT gain and difference in sensitivity between ADCs. One photoelectron corresponds to the 0.001554MeV and the scintillation light output is equal to 643 photoelectrons per 1MeV. This result is consistent with scintillation light output obtained from Monte-Carlo.

The Cherenkov light contribution to the absolute light output can be calculated using parameters found from the Monte-Carlo study. Figure 36 represents the ratio between Cherenkov and scintillation light yield as a function of kinetic energy of the recoil electron. Cherenkov light contributes up to 5% from the total light yield for 1MeV electron. Finally, the Monte-Carlo non-linearity result is shown in Figure 37. Obtained MC results are in very good agreement with experimental data measured by the Compton Spectrometer. The optimized on electrons with $E_{\text{kin}} < 1\text{MeV}$ Monte-Carlo model and obtained values of Birks coefficient and scintillation light output can be used to reproduce the calibration result obtained in KamLAND detector with gamma sources (see Table 2). As shown in Figure 38 our model reproduces the non-linearity measurements made in KamLAND detector with a very high accuracy. This MC model was also used to reproduce proton quenching results measured by the OCTAVIAN facility in Osaka University without extra tuning. Proton quenching is shown in Figure 39. Later our Monte-Carlo procedure was incorporated into global KamLAND simulation to properly calculate backgrounds for the antineutrino detections.

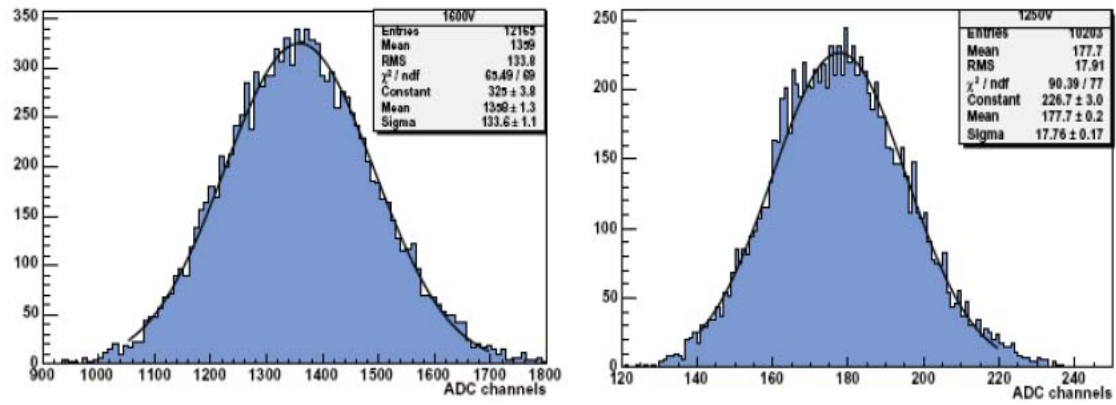


Figure 34: Distribution of the signals from PMT at 1600V (left) and 1250V (right).

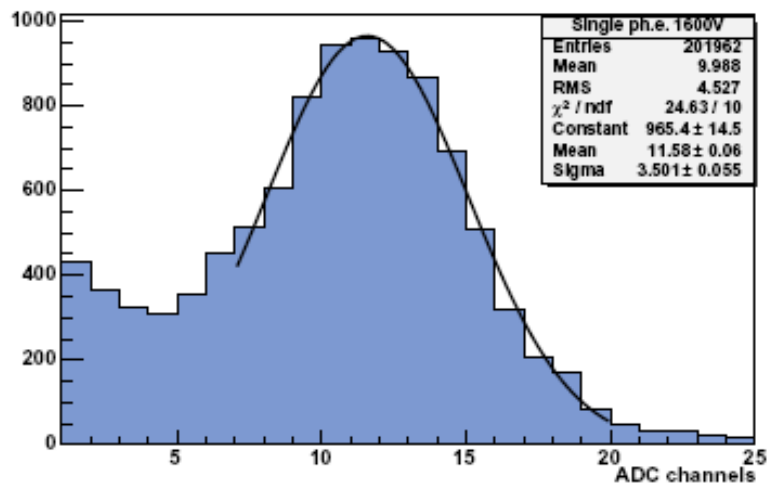


Figure 35: PMT signal distribution from the single photoelectron as a function of ADC channels.

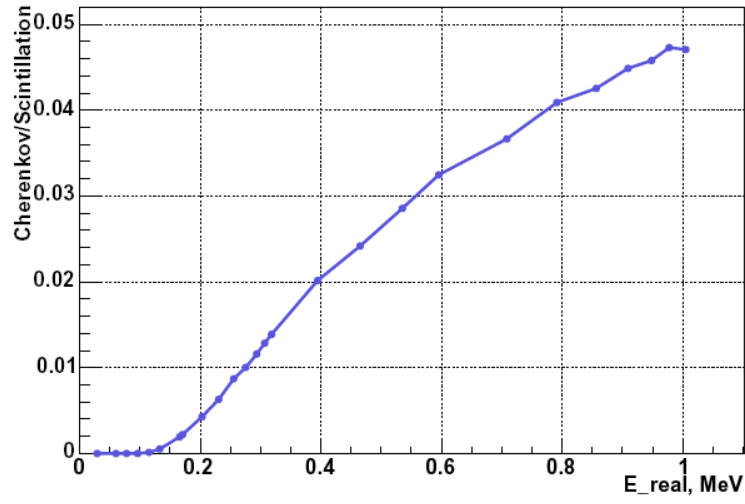


Figure 36: Cherenkov light contribution as a function or recoil electron energy

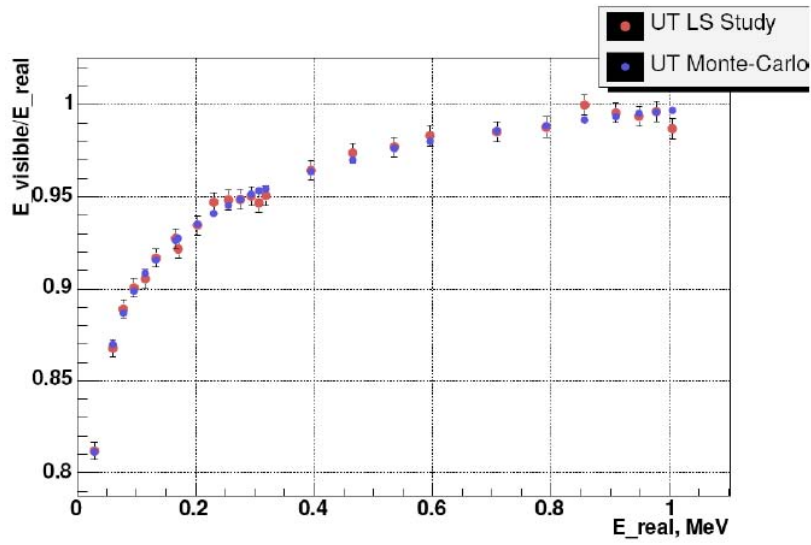


Figure 37: Non-linearity of the LS response to electrons measured by Compton Spectrometer (red) and from Monte-Carlo study (blue) as a function of real electron energy

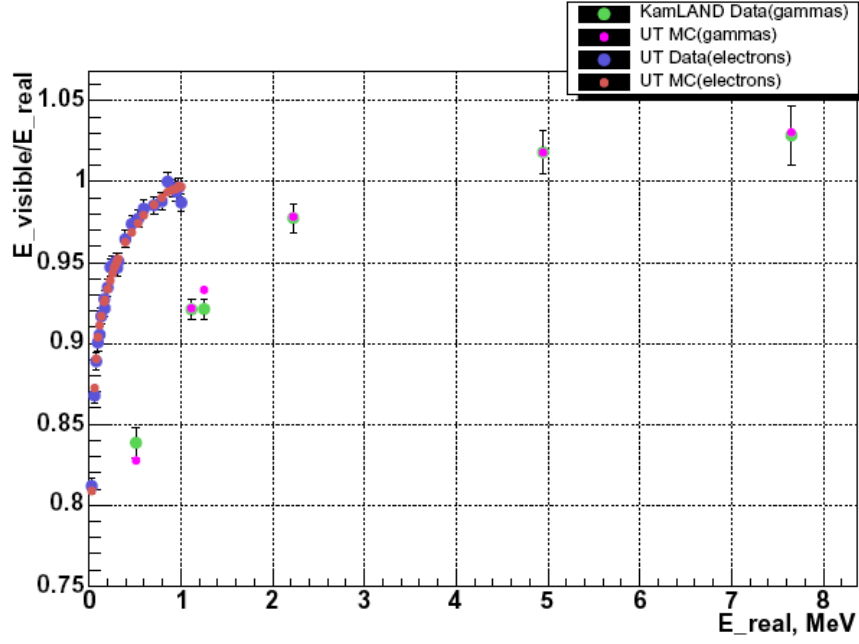


Figure 38: The LS response to electrons (Blue – Compton Spectrometer measurements, Red – Monte-Carlo study) same as Figure 37. The LS response to gammas (Green – KamLAND measurements with gamma calibration sources, Purple – Monte-Carlo study)

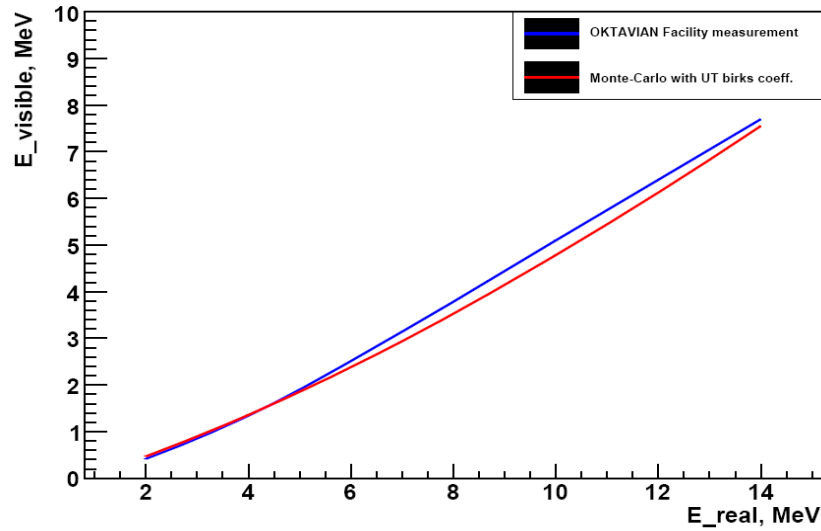


Figure 39: Proton quenching parameterization based on measurements made by OKTAVIAN Facility (blue line) and Monte-Carlo calculations (red line)

Chapter 4

Data Analysis

In 2004 the KamLAND collaboration had published results on the search for electron antineutrinos from the Sun [28] in the energy range 8.3-14.8 MeV. The results were based on data taken during the period March 4-December 1 2002. The corresponding live time was 185.5 days. No candidates have been found (see Figure 40) and collaboration set the upper limit on the electron antineutrino flux $3.7 \times 10^2 \text{ cm}^{-2} \text{ s}^{-1}$ and neutrino conversion probability 2.8×10^{-4} . During the last years the KamLAND collaboration implicated the new vertex reconstruction procedure, new energy reconstruction procedure and new improved muon vertex reconstruction algorithm which significantly improved the reconstruction accuracy of the events. These improvements along with statistics increased by a factor of 7.7 allow us to perform a significantly more sensitive search for electron antineutrinos from the Sun than has been reported in the early KamLAND publication [28]. The current study is based on 1425.9 live-days of data collection.

4.1 Verification of the Energy Scale

The main purpose of the KamLAND experiment was to search for the oscillations of reactor antineutrinos. These antineutrinos have an energy spectrum that mainly belongs to the energy region below 8 MeV. The vertex and energy reconstruction tools were optimized to reconstruct relatively low-energetic events. Since we are searching for the electron antineutrinos from the Sun with energies up to 15 MeV it is important to verify that energy and vertex reconstruction tools are able to reconstruct such energetic events correctly. To verify that β -decay events of cosmogenically produced ^{12}B can be used.

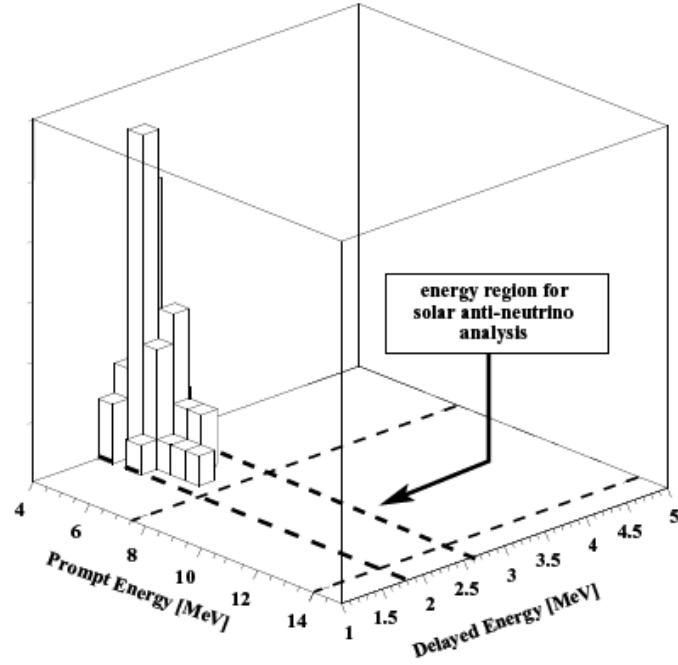


Figure 40: Energy distribution of the final event candidates from the first solar antineutrino KamLAND paper [28]. No candidates were found in the region of interest. The tail from reactor electron antineutrinos is visible below 8 MeV.

In KamLAND ^{12}B is produced by interaction of cosmic muons with carbon atoms in the scintillator. With the mean lifetime of 29.1 msec the ^{12}B isotope experiences β -decay and produces electrons with energies up to 13.4 MeV. Extraction of such events from the KamLAND data set and comparison of its spectra with theoretically calculated β spectra of ^{12}B allows us to make a conclusion about the quality of the reconstruction events with energies up to 15 MeV. ^{12}B candidates had been selected after muon events within 2-60 msec timing window. The background was selected within the same interval but in an off-timing window between 502-560 msec. Candidates were selected within 3 meters from muon track. The quality of the vertex reconstruction of these events can be verified using the spatial distribution of candidates inside the detector. Since the events that occurred in the buffer oil can produce only Cherenkov light in the ideal case, all events have to be reconstructed inside the volume with 6.5 m radius filled with liquid scintillator. Figure 41 shows the space-distribution of the candidates within the different energy windows. It can be clearly seen that candidates normally distributed inside the scintillator, but some of the candidates were reconstructed outside the balloon with LS inside the buffer oil. The reconstruction inefficiency of the ^{12}B candidates was calculated as a ratio between number of candidates reconstructed outside the LS and total number of reconstructed events. Figure 42 shows the reconstruction inefficiency as a function of energy of the events. The observed efficiency is better than 96% for almost all energy ranges except for the events with energies above 14 MeV where it decreases to ~87%. Energy spectra of ^{12}B events was built subtracting the events selected within the off-timing window 502-560 msec from events selected within 2-60 msec after muon events. To crosscheck the results obtained from the study of LS non-linearity the Monte-Carlo simulation was performed. Electrons with initial energies corresponding to the theoretical spectra of the ^{12}B β -decay were normally distributed inside the detector. The tracking of the electrons was made by GEANT.

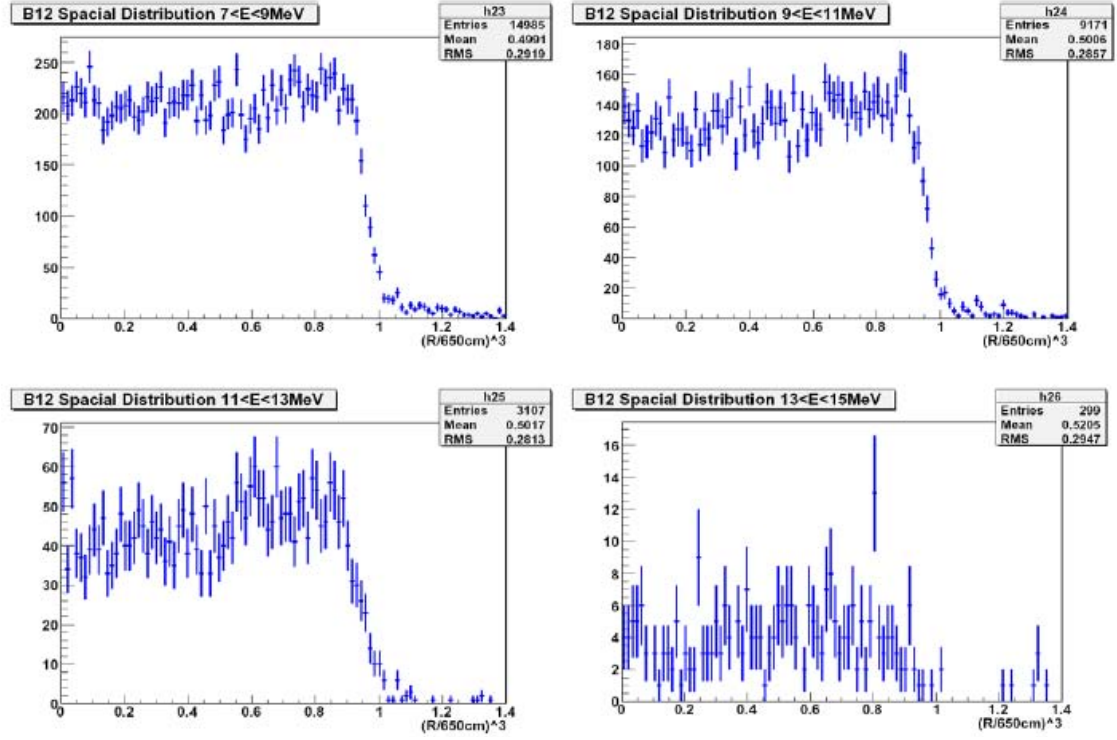


Figure 41: R^3 distribution of the ^{12}B events with different energy cuts inside the KamLAND detector as a function of radius of the balloon with scintillator. X-axis is a cubed ratio between actual radius of the event and radius of the balloon.

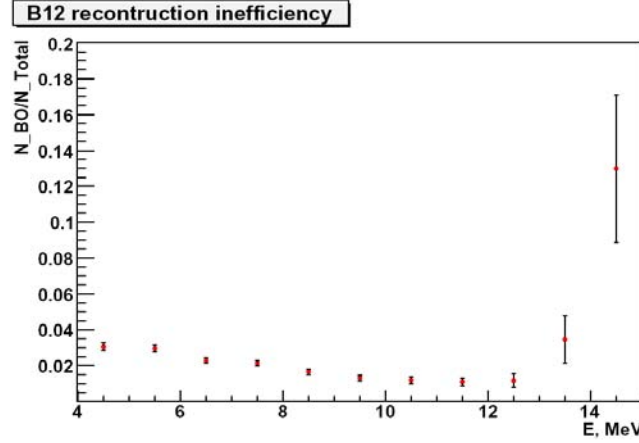


Figure 42: Reconstruction inefficiency of the ^{12}B events. Ratio between the events reconstructed inside the buffer oil to the total number of reconstructed events as a function of energy.

Using the Birks coefficient, scintillation light yield and number of Cherenkov photons detected obtained from the Monte-Carlo simulation of the LS non-linearity the visible energy of the electrons was calculated and then converted to the real energy. The combined plot of the background subtracted energy spectra of ^{12}B candidates, theoretical spectrum and Monte-Carlo spectrum is shown in Figure 43. All spectra are in very good agreement.

4.2 Candidates Selection

For the selection of the solar antineutrino candidates the KamLAND Analysis Tool (KAT) was used. Neutrinos from the ^8B decay on the Sun have energies up to 15 MeV. Neutrinos coming from nuclear power plants are the background for the current study. In order to eliminate reactor neutrino events, the 7.5-30MeV energy window was used during the analysis. Although we are not expecting electron antineutrinos coming from the Sun with energies higher than 15 MeV, the energy window 15-30MeV was used to cross check the background calculations.

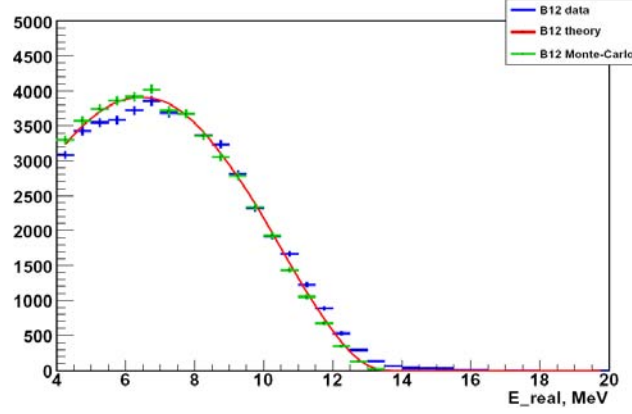


Figure 43: Energy spectrum of ^{12}B decay. Blue points are KamLAND data, red line is theoretical spectrum of ^{12}B decay and green points obtained from Monte-Carlo.

Electron antineutrino candidates' selection was based on the detection of two following signals: prompt - positron from inverse β -decay and delayed – neutron capture.

Since the traveling distance of thermal neutron is about few centimeters and its capture occurs about 210 μsec after β -decay, prompt and delayed events have to be time and spatially correlated in order to be related to the detection of positron (prompt event) from inverse β -decay and neutron capture (delayed event). The following cuts on events were applied:

- $7.5 \text{ MeV} < E_{\text{prompt}} < 30 \text{ MeV}$ and $1.8 \text{ MeV} < E_{\text{delayed}} < 2.6 \text{ MeV}$
- $R_{\text{prompt}} \& R_{\text{delayed}} < 600 \text{ cm}$.
- $dR_{\text{prompt-delayed}} < 160 \text{ cm}$
- $dT_{\text{prompt-delayed}} < 1000 \mu\text{sec}$

A fiducial 600 cm cut was applied for the prompt and delayed events, but the final results will be presented for the case of 550 cm fiducial volume cut as well. Spatial and timing correlation between prompt and delayed events was studied using large statistics from reactor antineutrino analysis. Figure 44 shows that the number of events that are not satisfied and the spatial and timing cuts are strongly suppressed. Efficiency of 1.6 m cut is 96.1% and timing cut efficiency is 99.2%.

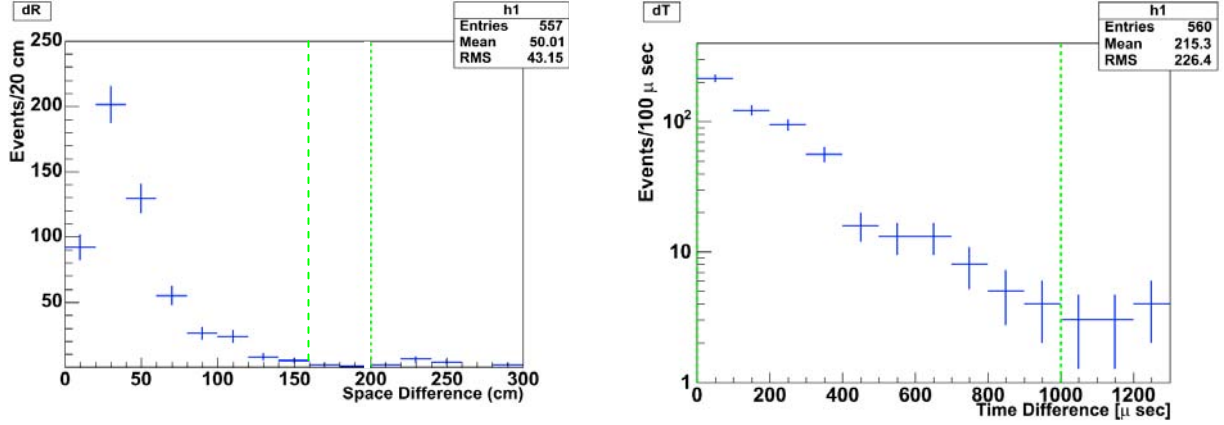


Figure 44: Spatial (left) and timing (right) correlation between events high statistics (reactor antineutrino analysis).

The 1 km depth of the KamLAND site protects the detector from cosmic muons. However it could not eliminate muons completely and the rate of the incoming muons through the entire detector is 0.3Hz. Cosmic muons interacting with the carbon atoms create radioactive isotopes. Interactions of muons with the surrounding rock produce neutrons coming inside the inner detector. The products of muon interactions can produce correlated events that mimic antineutrinos and such events are background for the antineutrino search analysis. To eliminate this background the muon veto cut has to be applied. Muon veto significantly reduces the background from relatively short lived isotopes such as ^{12}N , ^{12}B , ^9C , ^8B , ^8Li , ^8He , and ^9Li that have mean life times less than 2 seconds. Identity of the muon event in KamLAND is determined by the following criteria: total charge of 17” PMTs (TotalCharge17) larger than 10000 photoelectrons or TotalCharge17 is larger than 500 photoelectrons and number of hits in the outer detector is larger than 5.

The following muon veto criteria were applied for the selected candidates:

- Low Charged Muon (TotalCharge17<40000p.e.)

2msec veto for whole detector if TotalCharge17>13000p.e.

- Energetic Muon (TotalCharge17>40000p.e. and dQ>10⁶p.e.)

2sec veto for whole volume of detector

- Miss reconstructed muon (TotalCharge17>40000p.e. and badness>100)

2sec veto for whole volume of detector

- Well reconstructed non-energetic muon (TotalCharge17>40000p.e. and badness<100 and $dQ < 10^6$ p.e.)

2msec veto applied for the whole volume of the detector and 2sec veto applied on delayed events within 3 meters from the muon track.

Parameter dQ is a residual charge and it is defined as a difference between total charge that produced inside the inner detector and calculated charge (number of scintillation and Cherenkov photons) that expected to be produced by muon with certain track length.

After all cut had been applied three classes of events had been found:

- Regular Candidate (one prompt and one delayed events)
- Candidates with multiple neutrons (one prompt and two delayed events)
- Candidates with muon decay (two prompt and one delayed events)

Only one candidate with possible muon decay was found. Spatial difference between possible muon event and following it positron event is 6.4cm and time difference is 1.23 μ sec. Four candidates have multiple neutron captures events.

Following number of candidates were found for different energy and fiducial volume cuts:

- 5.5 m fiducial cut and energy window 7.5-15MeV: total 8 candidates were selected (1 multiple neutron capture event and 1 muon decay event)
- 6.0 m fiducial cut and energy window 7.5-15MeV: total 13 candidates were selected (2 multiple neutron capture events and 1 muon decay event)
- 5.5 m fiducial cut and energy window 15-30MeV: total 4 candidates were selected (1 multiple neutron capture event and 1 muon decay event)
- 6.0 m fiducial cut and energy window 15-30MeV: total 9 candidates were selected (2 multiple neutron capture events and 1 muon decay event)

Energy distributions of prompt and delayed events are shown in Figure 45 (5.5 m fiducial cut) and Figure 46 (6.0 m fiducial cut). Time and spatial correlations between prompt and delayed event for the selected candidates are shown in Figure 47 (5.5 m fiducial cut) and Figure 48 (6.0 m fiducial cut).

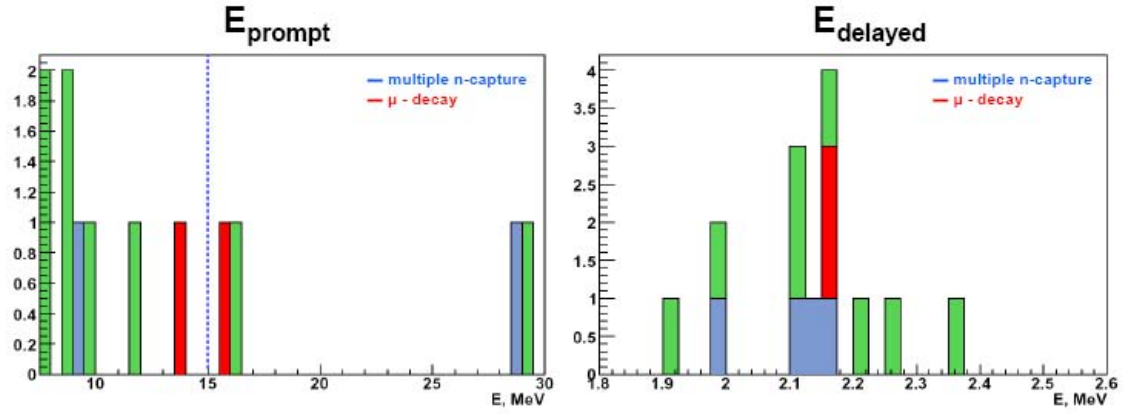


Figure 45: 5.5 meters volume. Prompt (left) and delayed (right) events energy spectra. Green candidates – one prompt and one delayed events, blue candidates – multiple neutron captures, red candidates – muon decay.

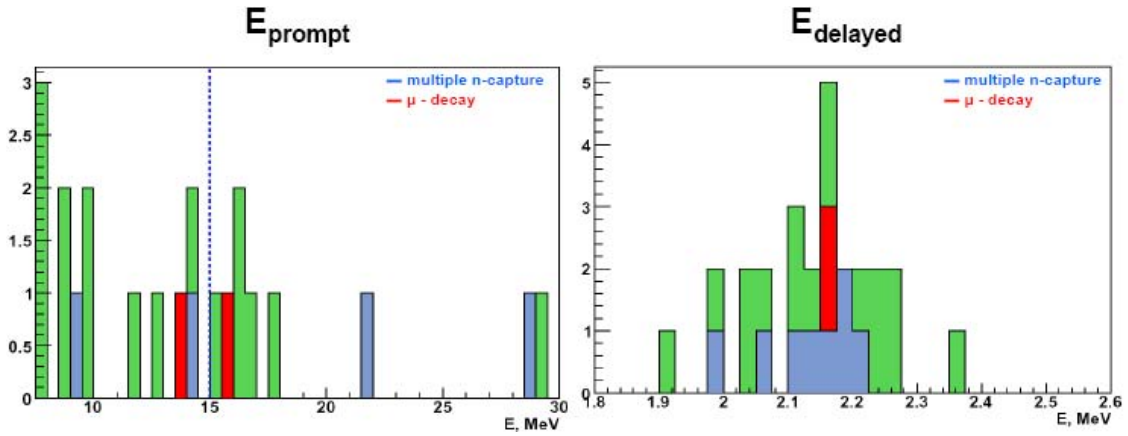


Figure 46: 6.0 meters volume. Prompt (left) and delayed (right) events energy spectra. Green candidates – one prompt and one delayed events, blue candidates – multiple neutron captures, red candidates – muon decay.

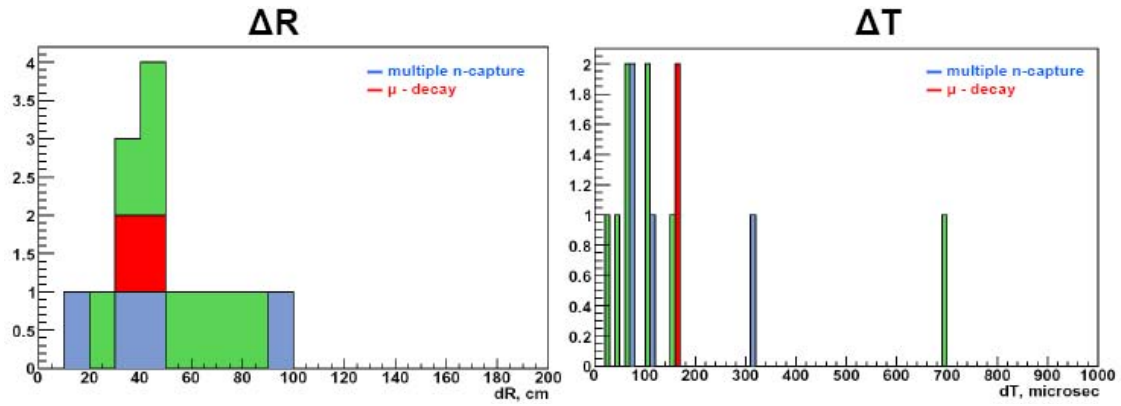


Figure 47: 5.5 meters volume. Space (left) and time (right) correlation between prompt and delayed events. Green candidates – one prompt and one delayed events, blue candidates – multiple neutron captures, red candidates – muon decay.

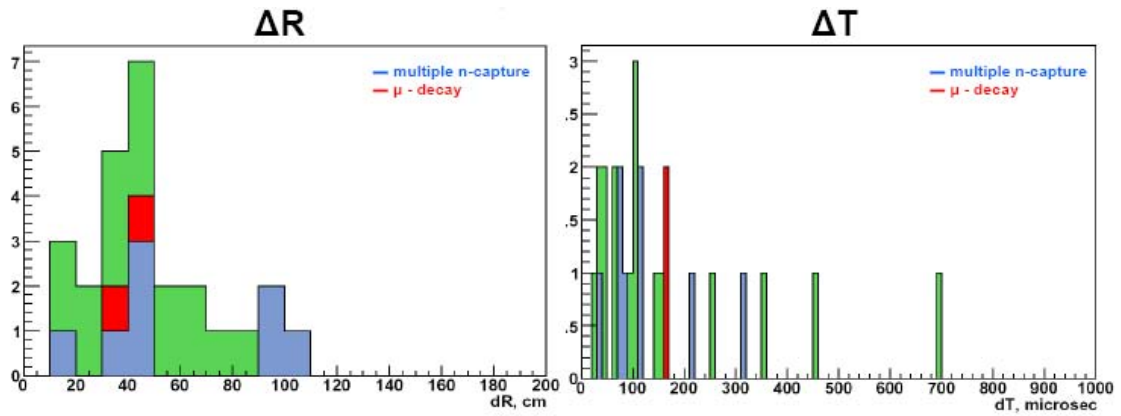


Figure 48: 6.0 meters volume. Space (left) and time (right) correlation between prompt and delayed events. Green candidates – one prompt and one delayed events, blue candidates – multiple neutron captures, red candidates – muon decay.

Chapter 5

Background calculation

Due to the very low rate of the selected candidates the calculation of the background is a very important part of this study. There are four sources of the background events: accidental background, background induced by muons, reactor antineutrinos interactions, and background from atmospheric neutrinos interactions. This chapter is dedicated to thoroughly calculations of the fore mentioned background sources.

5.1 Accidental Background

During the candidates selection procedure pairs of prompt and delayed events were selected. These events were time and space correlated. However there is a non-zero probability of accidental existence of event that could mimic delayed event for the selected prompt event. Such coincidence of the prompt and delayed events is an accidental background. The calculation of accidental background events was based on the selection of prompt event and following selection of the delayed event within off-time window. The selected off-time interval was chosen from 10 to 20 seconds after the prompt events. The off-time window is 10^4 times longer than time interval for neutrinos detection. This will reduce the statistical errors. The cuts on the selected prompt and delayed events were exactly the same as were described in Section 4.2 except the time correlation window was between 10 and 20 seconds instead of less than 1000 μsec . Figure 49 shows as expected no time correlation between prompt and delayed events within selected time interval. Energy spectrums of the accidental events for 5.5 and 6.0 meters are shown in Figure 50. The number of selected accidental events had been scaled by a factor of 10^{-4} . Results of the accidental background calculations are summarized in the Table 4.

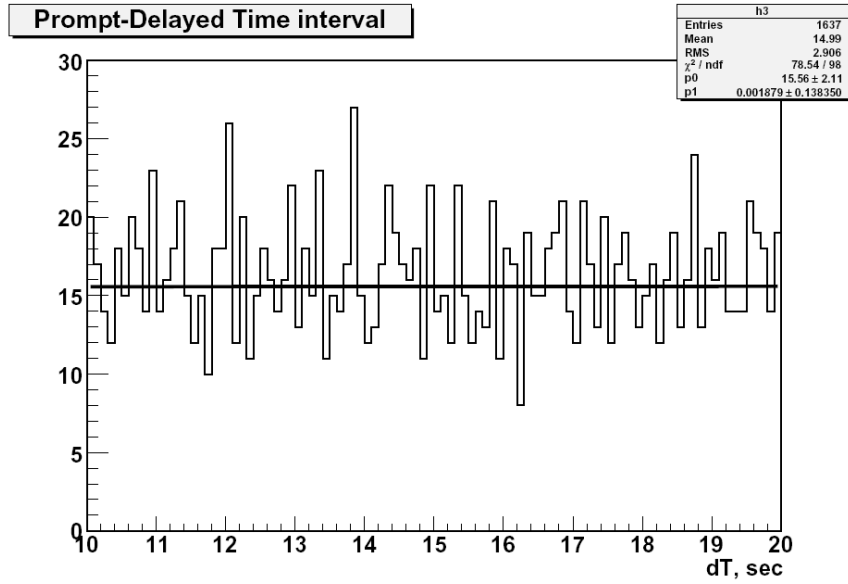


Figure 49: Accidental time intervals distribution between prompt and delayed events.

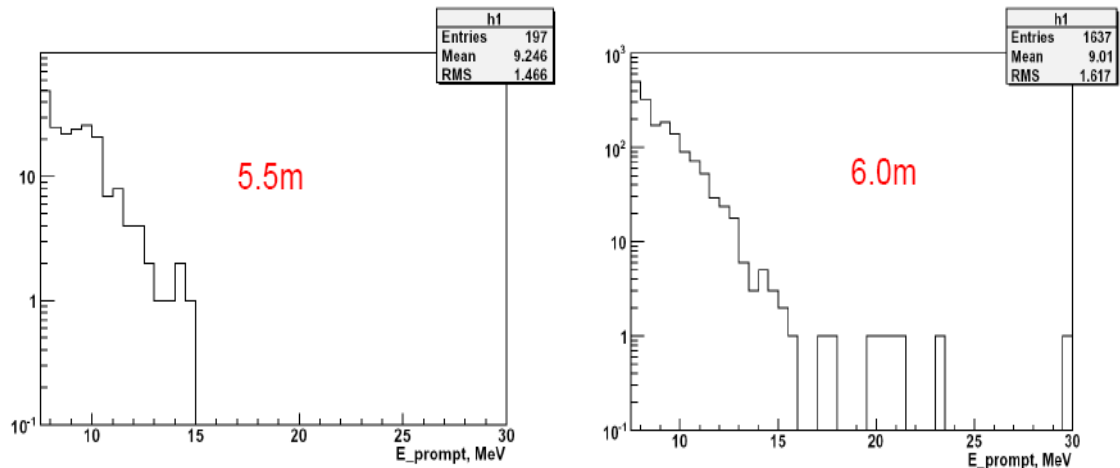


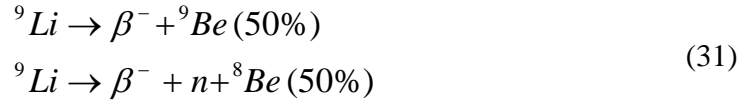
Figure 50: Energy distribution of the accidental events for the 5.5 m volume on the left and 6.0 m volume on the right. Number of events on both histograms has to be scaled by factor of 10^{-4} in order to obtain real number of accidentals.

Table 4: Accidental background summary (scaled to neutrino detection time interval).

Fiducial Volume, m	5.5		6.0	
Energy Range, MeV	7.5-15 MeV	15-30 MeV	7.5-15 MeV	15-30 MeV
Number of events	0.0197±0.0014	0	0.1626±0.0040	0.0011±0.0003

5.2 ^9Li Background

As it was already mentioned in the previous chapter, cosmic muons interacting with the carbon atoms in the scintillator produce various radioactive isotopes. Some of the isotopes via decay produce neutrons and β particles. Such correlated events mimic the actual solar antineutrinos interactions and are background for our study. The decay of ^9Li produced by incoming muon is a background event. Mean life time of ^9Li is 257.2 msec and following modes of the decay exist:



Only decay mode with production of the neutron is considered in the background analysis. Application of the muon veto while selecting the solar antineutrinos candidates significantly reduces the rate of ^9Li event, but can not remove it completely. Whole volume of the detector is vetoed for 2 seconds after showering muon. Since the mean life time of the isotope is almost eight times shorter than the veto period the ^9Li events produced by showering muon almost completely eliminates by muon veto procedure. In the case of interaction of non-showering muon 2 msec veto is applied for the entire volume and 2 seconds veto applied on the 3 meters cylindrical volume (see Section 4.2) around muon track. Three meters cylindrical cut is applied only for delayed events. The

background from non-showering muon makes main contribution and it is depends on the efficiency of the cylindrical cut that has been calculated in Section 5.2.

The ${}^9\text{Li}$ candidates were selected using the same cuts that were used for the selection of the solar antineutrino candidates, but muon veto was not applied. The candidates were selected within 1 second from muon events and the background was calculated in the off-timing window between 5 and 6 second after muon. In order to reduce statistical errors candidates were selected within 4-15MeV energy window and then the number of candidates had been scaled to 7.5-15MeV energy window using the scaling factor 0.277 obtained from the theoretical spectrum of the ${}^9\text{Li}$ decay. The background subtracted spectra of the selected ${}^9\text{Li}$ candidates and theoretical spectra are shown in Figure 51. Subtracting the background selected within the off-timing window from the ${}^9\text{Li}$ candidates for 6m fiducial volume 810 ± 35 events were found after showering muon and 205 ± 28 events after non-showering muon within 4-15MeV energy window. Applying scaling factor 0.277 following numbers obtained for the 7.5-15MeV window:

- Showering muon: 224.4 ± 9.7 events
- Non-showering muon: 56.8 ± 7.8 events

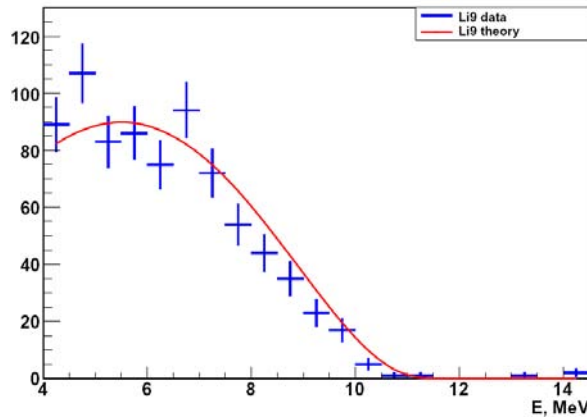


Figure 51: Energy distribution of the ${}^9\text{Li}$ events selected from the data (blue). Theoretical spectrum of the ${}^9\text{Li}$ β -decay events (red).

Only events remained after 2 second veto after showering and non-showering muon and events that outside 3 meters cut after non-showering muon contribute to the background. In order to estimate the background left after 3 meters cut had been applied it is necessary to know efficiency of 3 meters cut. This efficiency was calculated based on the spallation neutron study.

Interacting with the scintillator, cosmic muons break the carbon atoms producing numerous numbers of spallation neutrons. These neutrons capture on protons and ^{12}C within hundreds of microseconds with emission of 2.22MeV gamma (capture on proton) and 4.95MeV gamma (capture on carbon). The probability of neutron capture on proton and ^{12}C is about 99.5% and 0.5% respectively. Selection procedure of such events is based on the time difference from muon cut and the cut of the maximum number (NsumMax) of PMTs hits at the time when the trigger signal issued. Following cuts were applied for spallation neutron selection:

- NsumMax<1200
- $150\mu\text{sec} < dT < 1000\mu\text{sec}$ timing window for neutrons selection
- $2150\mu\text{sec} < dT < 3000\mu\text{sec}$ off-timing window background
- NsumMax < number of waveforms

The visible energy spectrum of neutron capture events is shown in Figure 52. Two peaks corresponding to the energy of emitted gammas are clearly seen. These events were used to estimate the efficiency of the 3 meters cut. Figure 53 shows the distance between neutron capture events and muon track. Ratio between events within 3 meters from muon and total number of events gives 94.1% cylindrical cut efficiency.

Using 257.2 msec ^9Li mean life time, 5.9% inefficiency of 3 meters cut and summarizing background from showering and non-showering muon 3.5 ± 0.5 background events were calculated for the 6 meters fiducial volume. Using the same procedure for the 5.5 meters fiducial volume 2.7 ± 0.4 background events were calculated.

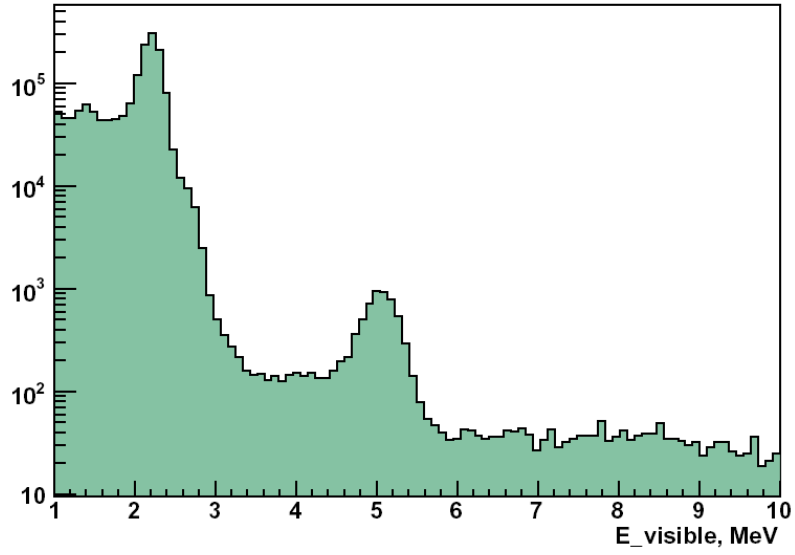


Figure 52: Visible energy spectrum of neutron capture events. First peak around 2.2MeV corresponds to neutron capture on proton and second peak around 5MeV corresponds to capture on ^{12}C .

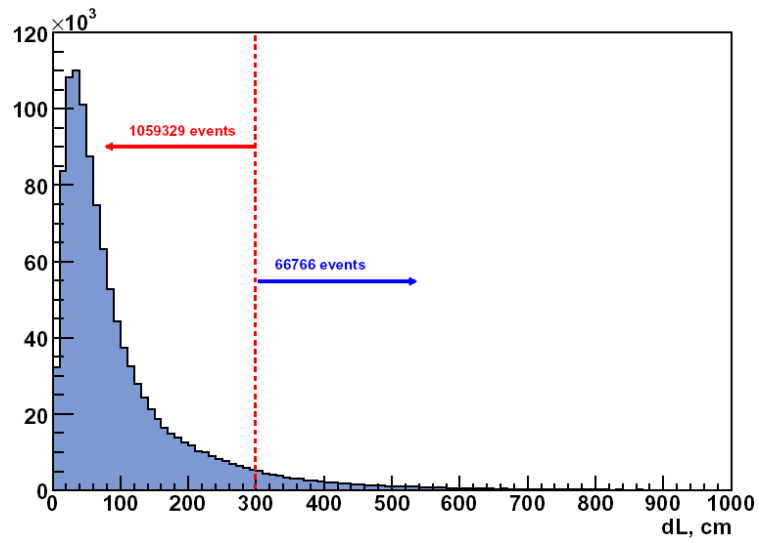


Figure 53: Distance between spallation neutron capture and muon track. 94.1% of events are within 3 meters cylindrical volume around muon track.

5.3 Reactor neutrinos background

Interactions of electron antineutrinos coming from the nuclear power plants surrounding the KamLAND site are background for the search of electron antineutrinos coming from the Sun. Although the number on reactor neutrinos with energies higher than 8.8MeV (it corresponds to the 7.5MeV prompt event) seems to be negligible (see Figure 6) it is important to estimate this background since the detection efficiency of these events is close to 100% and even one background event gives a significant contribution to the background due to the low statistics of the selected solar electron antineutrino candidates. The main contribution to the reactor antineutrino background is coming from the fission of ^{238}U . The initial reactor neutrinos spectra was taken from [16], [17], [18] and extrapolated up to 12MeV energy. The cross-section of electron antineutrinos interactions with proton is represented by (32).

$$\sigma_{\bar{\nu}_e p \rightarrow e^+ n} = 9.3 \cdot 10^{-48} \left(\frac{E_\nu}{1\text{MeV}} \right)^2 \left(1 - \frac{Q}{E_\nu} \right) \sqrt{1 - 2 \frac{Q}{E_\nu} + \frac{Q^2 - m_e^2}{E_\nu^2}} \Theta(E - Q) \quad (32)$$

where $Q=1.3\text{MeV}$ is mass difference between neutron and proton and $\Theta(E-Q)$ is a threshold function that equals 0 or 1 in case of $(E-Q)<0$ and $(E-Q)>0$, respectively.

Using the initial reactor neutrino spectra, information about number of fissions of each isotope during each KamLAND run, cross-section of electron antineutrino interaction on proton (32), 93% detection efficiency of such events and taking into account KamLAND neutrino oscillation parameters [8] the number of reactor neutrinos events were calculated. The expected prompt energy spectrum of reactor antineutrinos after oscillations is shown on Figure 54. For the energies above 7.5 MeV the reactor background rate is 1.9 ± 0.6 events for 6 meter volume and 1.5 ± 0.5 events for 5.5 meters volume.

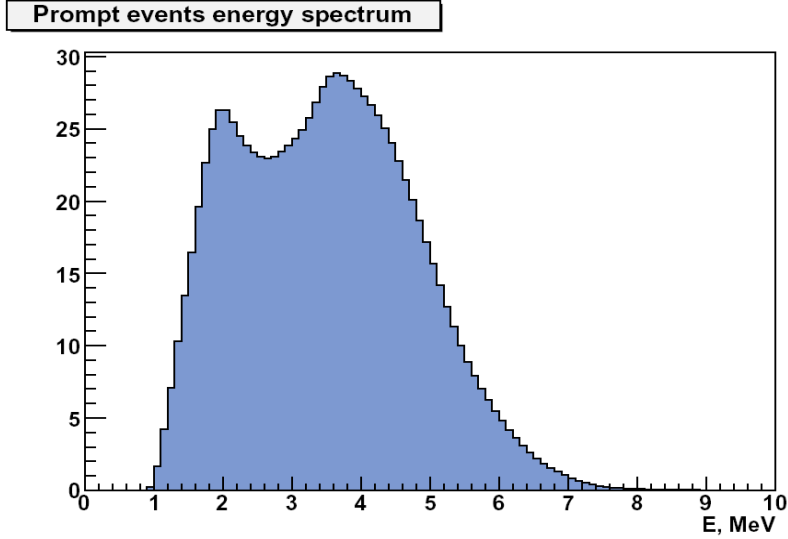


Figure 54: Expected prompt energy spectrum from reactor antineutrinos with oscillations.

5.4 Atmospheric neutrinos background

The interaction of the atmospheric neutrinos with carbon atoms in the KamLAND scintillator is the most significant source of the background. The nature of the atmospheric neutrinos has been already discussed in the Section 1.2.2. Two types of atmospheric neutrinos interactions are possible: neutral current interactions and charged current interactions. The summary of reactions considered as the background sources is given in Figure 55.

The global Monte-Carlo simulation based on GEANT program was performed in order to calculate the background caused by atmospheric neutrinos. Full KamLAND detector geometry was implemented into the simulation procedure. Each reaction was considered separately from the others with its own initial conditions. Atmospheric neutrino flux for this study was taken from [29]. The atmospheric neutrino fluxes are shown in Figure 56. Using the neutrino fluxes, cross-sections and number of carbon atoms in the scintillator (2.3×10^{31} carbon atoms in 5.5m volume) the initial neutrinos spectra were calculated.

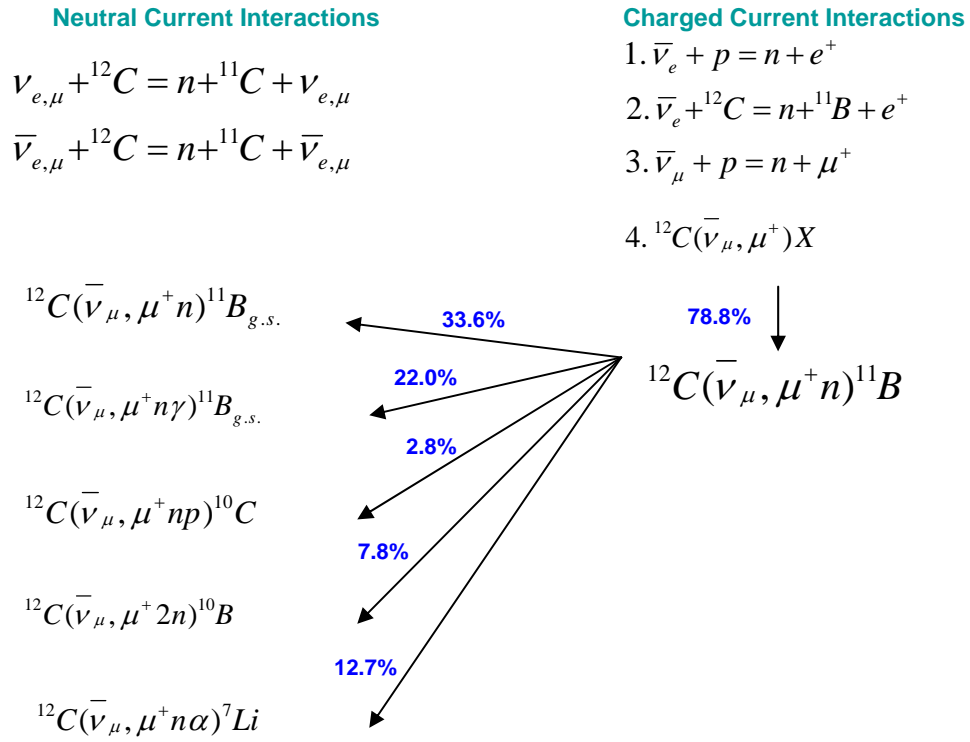


Figure 55: Source of the background from atmospheric neutrinos.

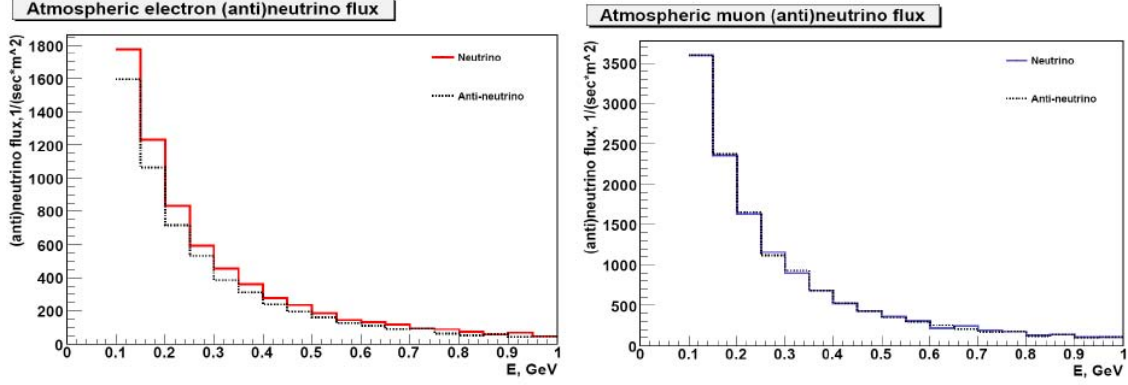


Figure 56: Atmospheric neutrino fluxes at KamLAND site: electron (anti)neutrinos fluxes on the left and muon (anti)neutrinos on the right. Solid color lines correspond to neutrinos and dashed lines correspond to antineutrinos.

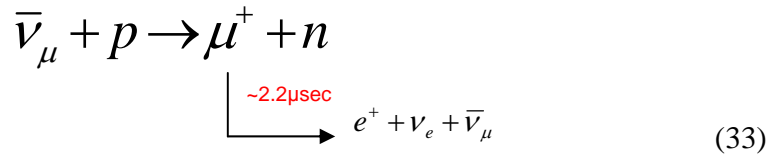
This result was used to calculate the spectra of the products of neutrino interactions with the scintillator. These spectra were used as input to the MC simulation program for the following tracking of the products of neutrino interactions. Due to the relatively small amount of expected interactions from atmospheric neutrinos at KamLAND detector 1000 times more events than expected were generated to make the results statistically significant. The atmospheric neutrino interaction points were uniformly distributed inside the inner detector.

During the particle tracking procedure energy deposition of each product of the reactions was appropriately quenched using the Birks' coefficient obtained from the non-linearity study of the liquid scintillator. Then using scintillation light yield and the number of Cherenkov photons from the non-linearity MC the visible energy of the prompt events was calculated according (29) and it was converted to the real energy using the procedure implemented into the KamLAND Analysis Tool. During this Monte-Carlo simulation the following array of data was created: prompt energy, delayed energy, prompt vertex, delayed vertex and time of delayed event relative to the prompt event. Background events were selected using exactly the same procedure was used for the selection of solar electron antineutrino candidates.

5.4.1 Atmospheric Charged Current Background

The cross section in Figure 12 had been used to calculate the number of electron antineutrino interactions on proton. The cross section for the muon antineutrino interactions on free proton and carbon was calculated by MiniBooNE collaboration [30]. These cross-sections are shown in Figure 57. Using the branching ratios [31] of each reaction of the charge current interaction of atmospheric muon antineutrino on the ^{12}C and cross-section the number of interactions can be calculated.

In case of muon antineutrino interactions on carbon, similarly to the data analysis, three classes of events can be selected: double coincidence, triple coincidence with one neutron capture and triple coincidence with double neutron capture. Triple coincidence with double neutron captures can only be observed during the reaction with the production of ^{10}B and two neutrons (see Figure 55). Triple coincidence with double prompt events and one neutron capture can be observed in the reactions with production of muon. Mean lifetime of the muon is $2.2\mu\text{sec}$ and muon itself is considered as a prompt event. Michael electrons produced during the muon decay are also considered as a prompt event. The number of triple coincidence events with double prompt events is strongly suppressed since all three events have to satisfy all selection cuts. The same procedure was applied during the selection background events and most of the triple coincidence events corresponded to the muon decay was eliminated by muon veto. The interaction of muon antineutrino on proton (33) gives the main contribution to the charge current interaction of atmospheric neutrinos.



Prompt event in this reaction can be either muon or positron coming from muon decay. Figure 58 shows uniform spatial distributions of the muon-prompt event and positron-prompt event candidates. The distribution of the distance between prompt and delayed

events is shown in Figure 59 for both muon and positron prompt events. These distributions are similar to ones obtained from the real data.

Finally, for muon antineutrino interactions on proton the number of background events expected for the 6 meters fiducial volume are 0.463 ± 0.021 for the 7.5-15 MeV energy range and 0.837 ± 0.029 events for the 15-30 MeV energy range. Figure 60 shows the prompt energy spectra for the background events.

A summary of background for all reactions is shown in Table 5 for 5.5 meters volume and in Table 6 for the 6 meters volume. A summary of the triplet coincidence background events is shown in Table 7.

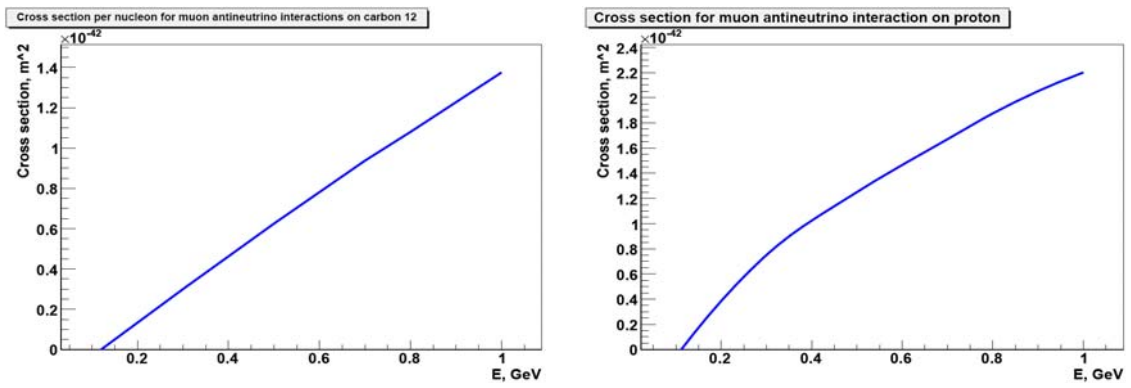


Figure 57: Cross-section per nucleon of muon antineutrino interactions on ^{12}C (left). Cross-section of muon antineutrino interactions on free proton (right).

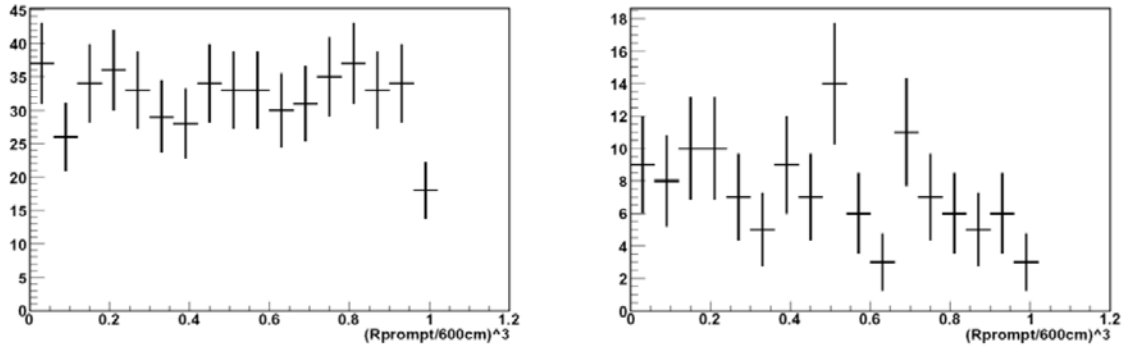


Figure 58: R^3 distributions for 6m volume of the muon-prompt event (left) and positron-prompt event (right).

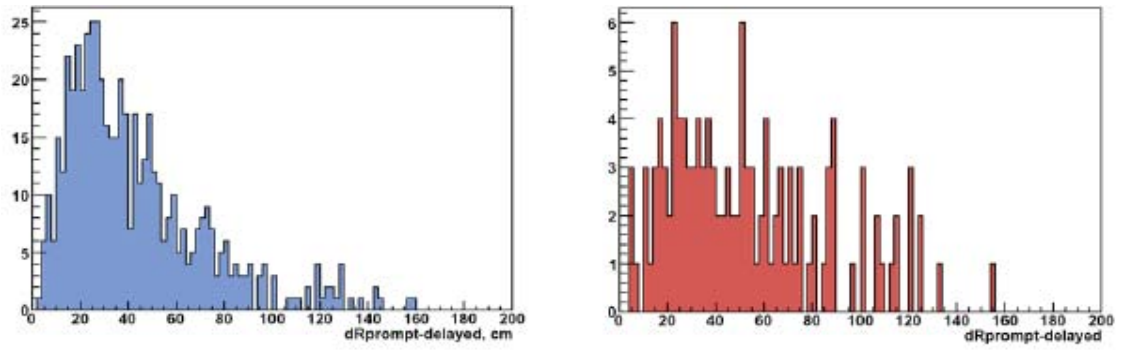


Figure 59: Distance between prompt and delayed events for muon-prompt event (left) and positron-prompt event (right).

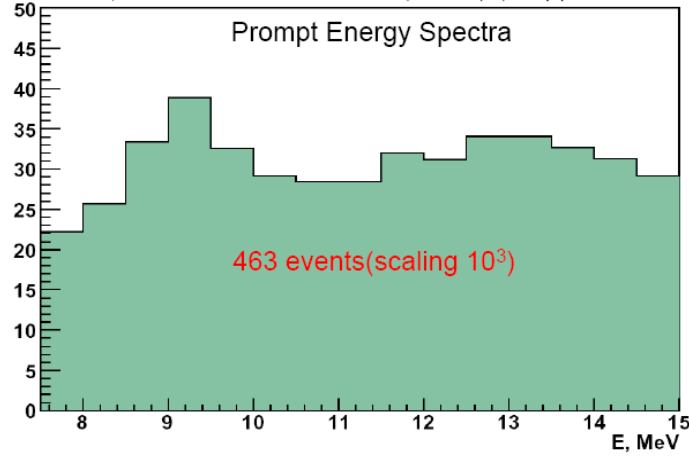


Figure 60: Prompt energy spectra of the background events coming from interactions of atmospheric muon antineutrinos on proton.

5.4.2 Atmospheric Neutral Current Background

The cross-section of the neutral current neutrino interactions on carbon atoms (34) was not measured or calculated yet. Due to the lack of knowledge of the exact cross-section of the neutral current interactions it is important to consider large uncertainties for the estimation of corresponding errors. The main sources of the uncertainties of the neutral current background rate are the uncertainties on the atmospheric neutrino flux and uncertainties on the cross-section. According to the [29] uncertainties on the atmospheric neutrino flux are about 22%. In order to be able to estimate the background coming from the neutral current interactions of atmospheric neutrinos on ^{12}C the cross-section of neutrino interactions on free neutron was used and then nuclear effects were applied. Uncertainties on the cross-section were taken from the measurements of neutral current interaction cross-section of neutrinos on free proton [32]. The maximum uncertainty of this measurement is 18%. The same uncertainty was used for the neutral current background study. The combined uncertainty is 28.4%.

$$\nu_{e,\mu} + {}^{12}\text{C} = n + {}^{11}\text{C} + \nu_{e,\mu} \quad (34)$$

The cross-section of neutrino interaction on free neutron can be obtained from the neutral current cross-section of neutrino interaction on free proton that was calculated in [32]. Figure 61 shows the neutral current neutrinos cross-section on free neutron and free proton as a function of squared transferred momentum for the neutrinos with the energy 1.25 GeV. Considering the different probability of neutron emission from the $s_{1/2}$ and $p_{3/2}$ shells of ^{12}C atom along with various de-excitation modes of $^{11}\text{C}^*$ nuclear effects were introduced. In ^{12}C atom there are four neutrons in the P-shell (outer shell) and two neutrons on the S shell (inner shell). The probability to remove neutron from the P and S shells are $2/3$ and $1/3$, respectively. The neutron disappearance from the P shell results in the de-excitation of $^{11}\text{C}^*$ accompanied by 2 MeV gamma emission and followed by β -decay [33].

The case of neutron disappearance from S-shell is more complicated. The $^{11}\text{C}^*$ excitation energy is 23 MeV and de-excitation procedure occurs via various modes. Branching ratios for the de-excitation mode was taken from [33].

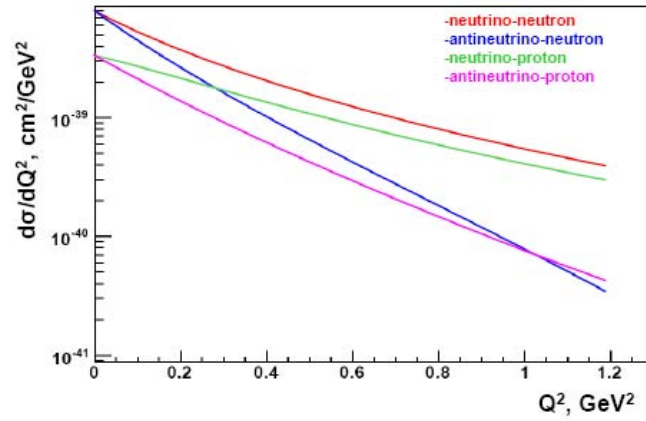


Figure 61: Cross-section of neutral current interaction of 1.25 GeV neutrinos on free proton and neutron as a function of squared transferred momentum.

Following de-excitation modes were considered to estimate the neutral current background:

- $^{11}\text{C}^* \rightarrow \gamma$ (2MeV)
- $^{11}\text{C}^* \rightarrow p \gamma$ ^{10}B
- $^{11}\text{C}^* \rightarrow p \alpha$ ^6Li
- $^{11}\text{C}^* \rightarrow p p$ ^9Be

The mode corresponded to the neutron emission from the outer shell gives the main contribution to the background. The spatial distribution of the prompt events and distance between prompt and delayed events for the neutron disappearance from the outer shell of ^{12}C are shown in Figure 62 and 63, respectively. The total number of background for this mode in 6 meters volume is 4.154 ± 0.064 for the 7.5-15 MeV energy range. The energy distribution of background events from neutral current interaction with neutron emission from the outer shell of carbon atom is shown in Figure 64. The summarized plot with all types of the background induced by atmospheric neutrino interactions in KamLAND detector is shown in Figure 65.

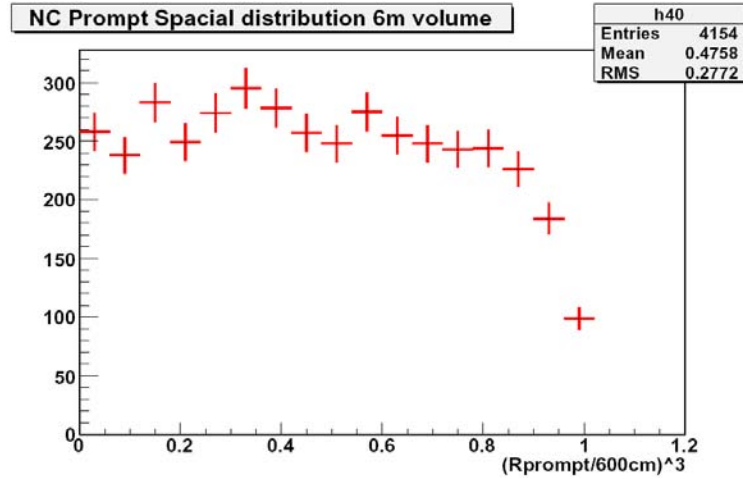


Figure 62: R^3 distribution of the neutral current (outer shell) background events in 6m. fiducial volume.

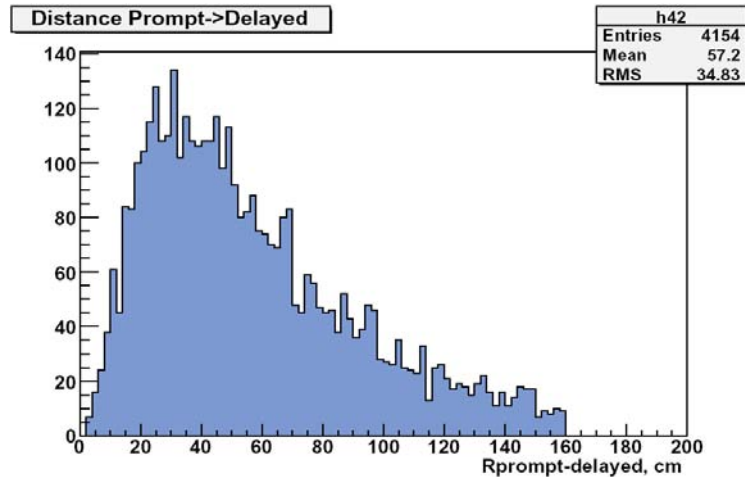


Figure 63: Distance between prompt and delayed events for neutral current interaction (outer shell) in 6m fiducial volume.

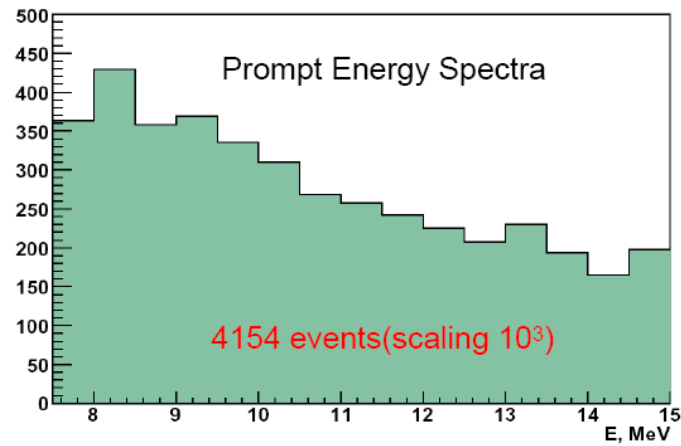


Figure 64: Prompt energy spectra of background from neutral current interactions (outer shell) in 6m fiducial volume.

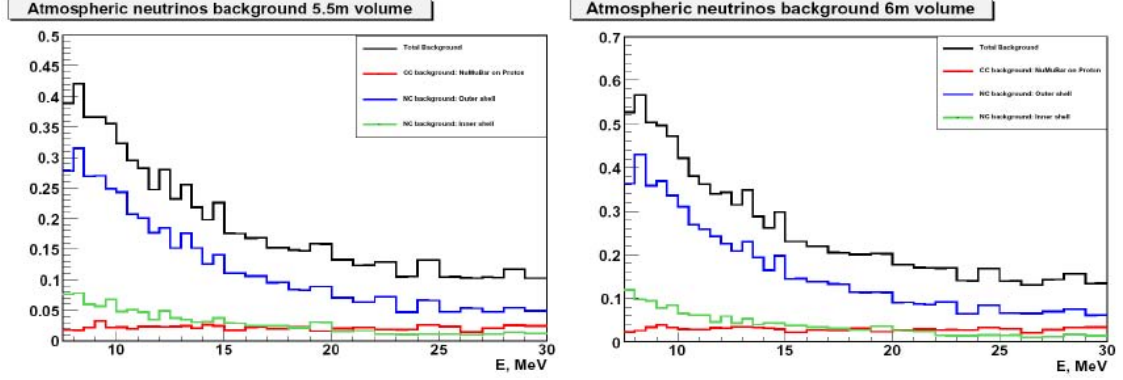


Figure 65: Atmospheric neutrino background spectra. The red line shows the background from charged current interactions. Green and blue lines correspond to background from neutral current interactions with neutron emission from inner and outer shells of carbon atom, respectively. Black line corresponds to the total background induced by atmospheric neutrino interactions.

5.5 Background Summary

The background had been calculated for the 5.5 and 6.0 meters fiducial volume within 7.5-15MeV and 15-30MeV energy ranges. The main background sources are the neutral current interactions of atmospheric neutrinos, background from ^9Li and reactor antineutrinos. The background for each source and reactions is summarized in the Table 5 for the 5.5 meters volume and Table 6 for the 6.0 meters volume. For the 5.5 meters analysis the background for the 7.5-15MeV energy window is 8.78 ± 2.16 events and 3.96 ± 1.04 for 15-30MeV energy range. For the 6.0 meters analysis the background for the 7.5-15MeV energy window is 11.61 ± 2.78 events and 5.24 ± 1.38 for 15-30MeV energy range. Triple coincidence events in KamLAND data and Monte-Carlo study of the background are summarized in Table 7.

Table 5: Background summary for the 5.5 meters fiducial volume

	7.5-15MeV	Comments	15-30MeV	Comments
Candidates				
$\bar{\nu}_e + p \rightarrow e^+ + n$	6	1 multiple n-capture, 1 μ -decay	2	1 multiple n-capture, 1 μ -decay
Charged Current Atmospheric Neutrinos Background				
$\nu_\mu + {}^{12}\text{C} \rightarrow \mu^- + n + {}^{11}\text{N}$	0.046		0.154	
$\bar{\nu}_\mu + {}^{12}\text{C} \rightarrow \mu^+ + n + {}^{11}\text{B} + \gamma$	0.03		0.136	
$\nu_\mu + {}^{12}\text{C} \rightarrow \mu^+ + n + {}^7\text{Li} + \alpha$	0.066		0.105	
$\nu_\mu + {}^{12}\text{C} \rightarrow \mu^+ + 2n + {}^{10}\text{B}$	0.007		0.006	
$\bar{\nu}_\mu + {}^{12}\text{C} \rightarrow \mu^+ + n + {}^{11}\text{B}$	0.073		0.246	
$\bar{\nu}_\mu + p \rightarrow \mu^+ + n$	0.344		0.626	
$\bar{\nu}_e + p \rightarrow e^+ + n$	0.008		0.022	
Neutral Current Atmospheric Neutrinos Background				
$\nu + {}^{12}\text{C} \rightarrow \nu + n + {}^{11}\text{C}$	3.882		2.619	
Neutrino int. in the rock	0.1		0.05	
Others				
${}^9\text{Li}$	2.7		0	
Reactor anti neutrinos	1.5		0	
Accidental background	0.02		0	
TOTAL Background				
	8.776		3.964	

Table 6: Background summary for 6.0 meters fiducial volume

	7.5-15MeV	Comments	15-30MeV	Comments
Candidates				
$\bar{\nu}_e + p \rightarrow e^+ + n$	10	2 multiple n-capture, 1 μ -decay	6	2 multiple n-capture, 1 μ -decay
Charged Current Atmospheric Neutrinos Background				
$\nu_\mu + {}^{12}\text{C} \rightarrow \mu^- + n + {}^{11}\text{N}$	0.063		0.203	
$\bar{\nu}_\mu + {}^{12}\text{C} \rightarrow \mu^+ + n + {}^{11}\text{B} + \gamma$	0.048		0.185	
$\bar{\nu}_\mu + {}^{12}\text{C} \rightarrow \mu^+ + n + {}^7\text{Li} + \alpha$	0.087		0.136	
$\bar{\nu}_\mu + {}^{12}\text{C} \rightarrow \mu^+ + 2n + {}^{10}\text{B}$	0.005		0.009	
$\bar{\nu}_\mu + {}^{12}\text{C} \rightarrow \mu^+ + n + {}^{11}\text{B}$	0.1		0.324	
$\bar{\nu}_\mu + p \rightarrow \mu^+ + n$	0.463		0.837	
$\bar{\nu}_e + p \rightarrow e^+ + n$	0.011		0.028	
Neutral Current Atmospheric Neutrinos Background				
$\nu + {}^{12}\text{C} \rightarrow \nu + n + {}^{11}\text{C}$	5.144		3.449	
Neutrino int. in the rock	0.13		0.07	
Others				
${}^9\text{Li}$	3.5		0	
Reactor anti neutrinos	1.9		0	
Accidental background	0.163		0.001	
TOTAL Background				
	11.614		5.242	

Table 7: Triple coincidence events in KamLAND data and Monte-Carlo study of the background.

7.5-15MeV							
DATA				Background			
5.5m volume		6.0m volume		5.5m volume		6.0m volume	
multi n-capture	μ -decay	multi n-capture	μ -decay	multi n-capture	μ -decay	multi n-capture	μ -decay
1	1	2	1	0.05	0.02	0.07	0.09
15-30MeV							
1	1	2	1	0.05	0.36	0.08	0.48

Chapter 6

Interpretation of results

6.1 Total number of candidates and background rates

During this study we were trying to observe the exotic mechanism of conversion of electron neutrinos produced in the Sun to the electron antineutrinos. This search was performed using data obtained by the KamLAND experiment. Two different fiducial volumes have been considered as the target volume of the detector 5.5 and 6.0 meters volumes. The data analysis procedure has been done for two energy regions. The energy range between 7.5 and 15 MeV have been used in the search of electron antineutrinos from the Sun and the energy window between 15 and 30 MeV was analyzed to compare the actual number of events found within this region from the data with the background calculated for this energy range. The background for both fiducial volumes and energy ranges was calculated. Using 5.5 meters fiducial volume 6 candidates was found within 7.5-15 MeV energy range and 2 candidates within 15-30MeV energy range. The corresponding background at 7.5-15MeV and 15-30MeV is 8.78 ± 2.16 and 3.96 ± 1.04 events respectively. For the 6.0 meters fiducial volume 10 and 6 candidates was found within 7.5-15MeV and 15-30MeV energy windows, respectively. The corresponding background is 11.61 ± 2.78 and 5.24 ± 1.38 counts. Based on obtained results the upper limit on the flux of electron antineutrinos coming from the Sun was set.

6.2 Electron antineutrino flux limit

Using the Feldman-Cousins unified approach [34] of confidence belt construction that can be applied to small signals relative the background the signal mean value. The limit on the electron antineutrino flux was calculated using (35).

$$\Phi_{\nu_e} = \frac{N_{signal}}{\sigma \times \varepsilon \times T \times n_{protons}} \quad (35)$$

Where N_{signal} is a signal mean value obtained using the 95% confidence level intervals from [34] for the known number of candidates and background rates, $\sigma=6.9 \times 10^{-42} \text{cm}^2$ – average cross-section, $\varepsilon=0.94$ – detection efficiency, $T=1.2 \times 10^8$ s. and $n_{protons}=4.6 \times 10^{31}$ and 6.0×10^{31} for 5.5 meters and 6.0 meters analysis, respectively. Thus the upper limit is $1.2 \times 10^2 \text{ cm}^2 \text{s}^{-1}$ for 5.5 meters analysis and $1.3 \times 10^2 \text{ cm}^2 \text{s}^{-1}$ for 6.0 meters analysis. Both 5.5 and 6.0 meters analysis results are consistent within margin of errors. Considering only the limit corresponded to 5.5 meters analysis, this limit was improved by factor of 3 compared to the previous KamLAND result [28]. Due to presence of background further increase of statistics would not significantly improve this result in KamLAND-like detectort.

6.3 Limits on the neutrino conversion probability and product of the neutrino magnetic moment and magnetic field.

The 7.5-15MeV energy region of prompt events corresponds to the $8.8 < E_\nu < 16.3$ MeV antineutrino energies. The total ^8B solar neutrino flux is $5.05 \times 10^6 \text{cm}^{-2} \text{s}^{-1}$ [40]. The neutrino energy window between 8.8 and 16.3 MeV contains 24.05% of total ^8B neutrino flux. Using the obtained upper limit on the electron antineutrino flux for the 5.5 meters fiducial volume the probability of conversion electron neutrinos produced on the Sun to electron antineutrinos is 9.8×10^{-5} . Then using the conversion probability it is possible to set the upper limit on the product of the neutrino magnetic moment and transverse component of the magnetic field in the Sun (36).

$$\frac{\mu}{10^{-12} \mu_B} \frac{B_T(0.05R_s)}{10kG} < 7.7 \times 10^2 \quad (36)$$

The magnetic field in the core of the Sun is not very well known that is why it is not possible to get the exact limit on the neutrino magnetic moment itself using (36).

6.4 Diffuse Supernovae neutrino flux

Although neutrinos coming from the single Supernovae explosion can be detected in practice, the rate of the supernovae explosions is believed to be about 1-3 per hundred years in the Milky Way size galaxy and it statistically it would take years to observe such events. The more reasonable approach is to observe integrated flux of neutrinos coming from all Supernovae. Such integrated neutrino flux calls the diffuse supernovae neutrino flux (DSNF). Observation of the DSNF gives possibility to get information about the neutrino production from the Supernovae explosions and can help to distinguish between various cosmological models [39].

Limits obtained on the electron antineutrinos can be used as an upper limit on the diffuse Supernova neutrino flux. The diffuse Supernovae neutrinos possess energies up to 60 MeV. Recently SuperKamiokande [35], [36] and SNO collaboration [37] set the limits on the diffuse Supernovae neutrino flux only for energies higher than 20 MeV. The KamLAND collaboration results could be used to set a limit on the diffuse Supernovae neutrino flux for energies below 20 MeV. For the energy range 8.8-16.3MeV the limit on DSNF is $15.9 \text{ cm}^{-2}\text{s}^{-1}\text{MeV}^{-1}$. This limit improved the previous limit set by KamLAND by factor of 3.6. The current best limits are summarized and shown of Figure 66 [37].

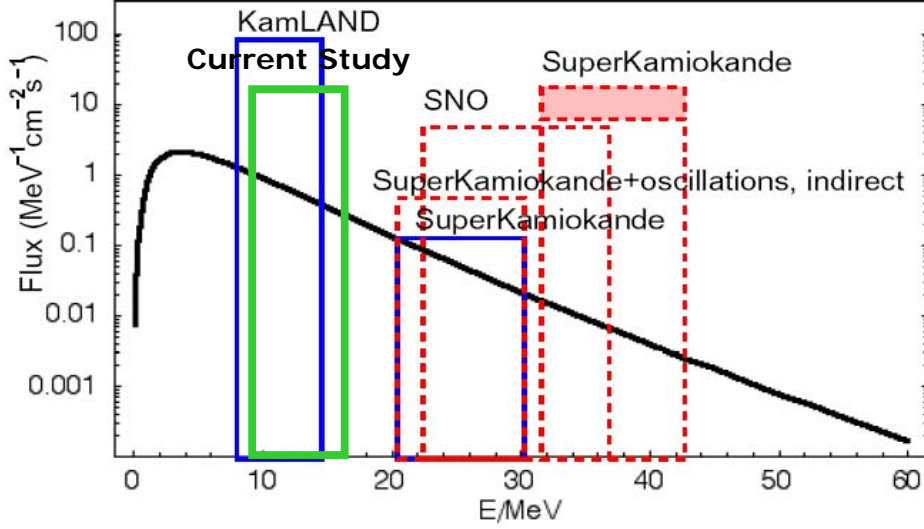


Figure 66: Diffuse Supernovae neutrino flux and current limits obtained by SuperK, SNO and KamLAND. The blue solid lines and the red dash lines correspond to electron antineutrinos and electron neutrinos respectively. The black line represents the theoretically predicted diffuse supernovae flux. The green solid line represent limit obtained during this study. The plot had been taken from [38] and current study limit had been added.

6.5 Future large scintillator neutrino detectors.

The background rates obtained during this study can help estimate the background for the future large scintillator neutrino detectors such as LENA [40]. According to obtained result the main source of the background is neutral current interaction of the atmospheric neutrinos with the scintillator. Let us consider the large detector similar to detector proposed by future LENA experiment, filled with 5×10^4 cubic meters of scintillator the same that we are using in KamLAND.

Using the neutral current background rate obtained during this study it is possible to estimate the total number of neutral current background events within 15-30 MeV energy range during 10 years of measurements. The time scale factor is about 2.5 comparing to live-time used for the search of electron antineutrinos from the Sun in current study. The detector volume scale factor is 71.7 with respect to 5.5m fiducial volume. Combining

these scale factors and 2.6 neutral current events found in 15-30 MeV energy range the total rate of the background caused by atmospheric neutrino interactions is about 50 events per one year. According to the LENA proposal of measurement diffuse Supernovae neutrino flux [40] the expected total background rate within 19-25 MeV energy range is 5.6 events per 10 years. The background within 15-30 MeV energy range is flat and obtained 50 events per one year with in 15-30 MeV energy range can be scaled to 19-25 MeV window. As the result about 200 neutral current background events are expected in 19-25 MeV range in 10 years. This result clearly shows (see Figure 67) that proposed by LENA collaboration limits on the diffuse Supernovae neutrino flux can not be achieved and importance of the neutral current background for the future neutrino experiments with scintillation detectors.

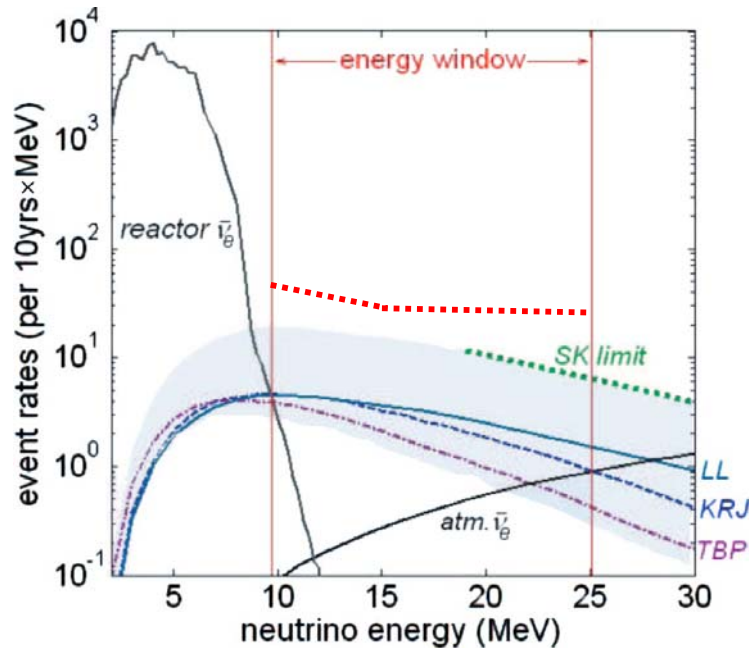


Figure 67: Event rates expected by LENA experiment from reactor, atmospheric and diffuse supernovae electron antineutrinos. DSNF is based on various models (LL, KRJ and TBP). Plot is taken from [40]. Red dashed line added to this plot shows neutral current background calculated during this study and scaled corresponding time exposure and target volume of proposed LENA experiment.

Chapter 7

Conclusions

This dissertation represents the results of the search for electron antineutrinos from the Sun with KamLAND detector within the 8.8-16.3 MeV energy range. The aim of this work was to improve the current limits on the flux of electron antineutrinos coming from the Sun, probability of conversion ^8B electron neutrinos produced in the core of the Sun to electron antineutrinos and product of the neutrino magnetic moment and transverse component of the magnetic field in the neutrino production region. Existing limits on these parameters were set by KamLAND collaboration [28] as well and these limits were: $\Phi_\nu < 3.7 \times 10^2 \text{ cm}^{-2} \text{ s}^{-1}$, $P_{\text{conversion}} < 2.8 \times 10^{-4}$ and the limit on the product of the neutrino magnetic moment and transverse component of magnetic field 1.3×10^3 .

The current study is based on the 1425.9 days of data collection instead of 185.5 days live-time used in the previous study. The rate of the observed signal is comparable with the expected background rate and it was vital to correctly calculate the background to improve the existing limits on the parameters. One of the main parts of the current research was dedicated to the development of the global Monte-Carlo simulation program which is used to calculate the background caused by atmospheric neutrinos.

On the initial stage of the background estimation procedure the Compton Spectrometer was built to measure the response of the KamLAND scintillator to low energy electrons. The scintillator response result and KamLAND calibration data had been reproduced with the MC simulation. That allowed us extract following scintillator's parameters: Birks' coefficient, scintillation light yield and number of detected Cherenkov

photons and to implement these parameters to the global Monte-Carlo program. The background was calculated within 7.5-30 MeV prompt energy range.

The data analysis had been performed for 5.5 and 6.0 meters fiducial volumes. The number of found electron antineutrinos candidates within 8.8-16.3 MeV energy range is 6 and 10 for the 5.5 and 6.0 meters analysis respectively. The background rate for 5.5 and 6.0 meters was 8.8 and 11.6 events respectively. Using the number of electron antineutrino candidates and background rate the new limit on the flux of electron antineutrinos coming from the Sun had been set.

Obtained flux limits are $1.2 \times 10^2 \text{ cm}^{-2} \text{ s}^{-1}$ and $1.3 \times 10^2 \text{ cm}^{-2} \text{ s}^{-1}$ with 95% confidence level for 5.5 and 6.0 meters analysis. Limits coming from two different fiducial volumes are consistent with each other within margin of errors. The 5.5 meters analysis gives stringent limit on the electron antineutrino flux. With this limit the previous KamLAND result was improved by factor of 3. This limit was used to calculate the neutrino conversion probability and product of the neutrino magnetic moment and magnetic field in the core of the Sun. The observed probability of electron neutrino conversion to electron antineutrinos is $P_{\text{conversion}} < 9.8 \times 10^{-5}$. The upper limit on the product of the neutrino magnetic moment and magnetic field is 7.7×10^2 .

The upper limit on the electron antineutrino flux coming from the Sun can be useful to estimate the upper limit on the diffuse Supernovae electron antineutrino flux. The limit on DSNF is $15.9 \text{ cm}^{-2} \text{ s}^{-1} \text{ MeV}^{-1}$ within 8.8-16.3 MeV energy range and it was improved by factor of 3.6 with respect to the limit based on the previous limit on electron antineutrinos from the Sun set by KamLAND.

The results of the background calculation within 8.8-31.3 MeV neutrino energy interval are very important for the future large scintillator neutrinos detectors. It was demonstrated using as example LENA experiment proposal that the background induced by interaction of atmospheric neutrinos is underestimated by 2-3 orders of magnitude.

Bibliography

- [1] M. Frank Phys. Rev. D60, 093005
- [2] Castellani, V. & degl'Innocenti, S. Astrophysical Journal, Part 1 (ISSN 0004-637X), vol. 402, no. 2, p. 574-578.1
- [3] G.G. Raffelt, Phys.Rept.320:319-327, 1999
- [4] Kazuo Fujikawa, Robert Shrock (SUNY, Stony Brook) Phys.Rev.Lett.45:963,1980
- [5] Z. Daraktchieva et al., Phys.Lett.B615:153-159, 2005
- [6] E. K. Akhmedov, Phys. Lett. B **213**, 64 (1988)
- [7] E. Kh. Akhmedov, J. Pulido, Phys.Lett.B553:7-17, 2003
- [8] S. Abe et al., Phys. Rev. Lett. 100:221803, 2008
- [9] J. N Bahcall, <http://www.neutrinooscillation.org>
- [10] R. Davis, Jr., et al., Phys. Rev. Lett. 20, 1205 (1968)
- [11] Ahmad, Q. R., et al., Phys. Rev. Lett. 89 011301 (2002)
- [12] B. Aharmim et al., Phys. Rev. Lett. **101**, 111301 (2008)
- [13] Y Ashie et al., Phys. Rev. D 71, 112005 (2005)
- [14] J. Hosaka et al., Physical review D74, 032002(2006)
- [15] Y. Ashie et al., hep-ex/0404034
- [16] K. Schreckenbach et al., Phys. Lett. B160, 325(1985)
- [17] A.A. Hahn et al. Phys. Lett B218 365(1989)
- [18] P. Vogel et al., Phys. Rev. C24, 1543(1981)
- [19] K. Eguchi et al., Phys. Rev. Lett. 90, 021802 (2003)
- [20] L. B. Okun "Elementary particle physics" 1984 (in Russian)
- [21] K. Ichikawa "Neutrino mass constraint from CMB and its degeneracy with other cosmological parameters", Journal of Physics: Conference Series 120 (2008) 022004
- [22] J. B. Birks "The theory and practice of scintillation counting", Oxford. Pergamon Press, 1964
- [23] T. Mukoyama "Range of electrons and positrons", NIM 134(1976) 125-127

- [24] J. A. Gledhill “The range-energy relation for 0.1-600keV electrons” J. Phys. A: Math., Nucl. Gen., Vol. 6, September 1973
- [25] Ch. Weinheimer “The Mainz Neutrino Experiment” NEUTRINO 2000 Conference
- [26] W. Heller, Physical Review vol. 68 (1945) 5-10
- [27] R. Mehra, Proc. Indian Acad. Sci. (Chem. Sci.), vol. 115 (2003)147-154
- [28] K. Eguchi et al., Phys.Rev.Lett.92:071301, 2004
- [29] M. Honda, et al., Phys. Rev. D75, 043006(2007)
- [30] M. Sajjad Athar, Shakeb Ahmad, S.K. Singh, Phys.Rev.D75:093003,2007.
- [31] E. Kolbe, K. Langanke, F.-K. Thielmann, P. Vogel, Phys.Rev.C52:3437-3441,1995.
- [32] L. A. Ahrens, et. al., Phys. Rev. D 35, 785 (1987)
- [33] Y. Kamyshev, E. Kolbe, Phys. Rev. D 67, 076007 (2003)
- [34] G. J Feldman and R. D. Cousins, Phys. Rev. D 57, 3873 (1998)
- [35] M. Malek et al., Phys. Red, Lett. 90, 061101 (2003)
- [36] C. Lunardini, Phys. Rev. D73, 083009 (2006)
- [37] B. Aharmim et al., hep-ex/0607010 (2006)
- [38] C. Lunardini astro-ph/0610534
- [39] S Ando 2004 Astrophys. J. 607 20
- [40] M. Wurm et al., Phys. Rev. D 75, 023007 (2007)

Vita

Oleg Perevozchikov was born in Protvino, Moscow region, Russia on November 30, 1974. He graduated from High School in 1992. In 1995 he was accepted to the Physics department of the Moscow State University (Russia) where he earned Master Degree with a concentration in Elementary Particle physics in 2001. In 2004 he went to the graduate school of the University of Tennessee, Knoxville to pursue his doctor of philosophy degree at the Department of Physics and Astronomy with concentration in High Energy and Elementary Particle physics.